# Nanoscale imaging of restricted cell membrane receptor diffusion

## DISSERTATION

zur Erlangung des akademischen Grades
doctor rerum naturalium
(Dr. rer. nat.)
im Fach Biophysik

eingereicht an der
Mathematisch-Naturwissenschaftlichen Fakultät I
Humboldt-Universität zu Berlin

von
Herr Dipl.-Phys. ChristianTischer
geboren am 13.12.1973 in Stuttgart

Präsident der Humboldt-Universität zu Berlin:
Prof. Dr. Jürgen Mlynek

Dekan der Mathematisch-Naturwissenschaftlichen Fakultät I:
Prof. Thomas Buckhout, PhD

Gutachter:

1. Prof. Dr. Reinhart Heinrich
2. Prof. Dr. Philippe Bastiaens
3. Prof. Dr. Ernst-Ludwig Florin

Tag der mündlichen Prüfung: 9. Juni 2005

# Abstract

In the work presented, a novel imaging technique (TNIM - Thermal Noise Imaging Microscopy) was developed for the purpose of studying nanoscale diffusive motion in heterogeneous media. TNI-Microscopy was specifically used to investigate if the mobility of cell membrane receptors is influenced by lateral membrane nanostructures. The direct investigation of these two-dimensional ultrastructures in living cells was up to now hampered because of lacking microscopy techniques. In TNI-Microscopy, the diffusive motion of a nanoparticle is limited to a small volume, making it possible to observe constraints on the particle's motion. Thus, the particle can be used to sample nanostructures. Concomitant, it is also recorded how the dynamics of the particle's motion are influenced by hydrodynamic coupling to the sampled structures. To realise TNI-Microscopy, a microscope was built that employs an optical trap to limit the diffusive motion of a probe particle to a submicroscopic volume. Within this volume, the particle position fluctuations are tracked with nanometer spatial precision and microsecond temporal resolution using an interferometric position detector. Initially, experiments on rigid three-dimensional structures were conducted, demonstrating that objects such as the filaments of a polymer network can be clearly seen in histograms of the particle's position fluctuations. From these histograms the position of objects could be determined with a precision of about 10 nm in three dimensions. These experiments were of fundamental significance as they confirmed that diffusive motion of a probe particle can indeed be used to image nanoscopic objects. In subsequent experiments it could be shown that it is simultaneously possible to capture the dynamics of the three-dimensional particle position fluctuations. Existing hydrodynamic theories that describe the mobility of a sphere (probe particle) at different distances to a rigid interface could be validated from the nanometer to the micrometer scale. Thus, the fundamental concepts of TNI-Microscopy were established and could be used to study how the mobility of cell membrane receptors is influenced by membrane lateral nanostructures. To achieve this, nanoparticles were bound specifically to the cell membrane epidermal growth factor (EGF) receptor. In this case, the particle served to make the lateral motion of the EGF-receptors observable and to limit its motion to a submicroscopic membrane area. Thus, the motion of EGF-receptors could be observed in a small membrane area for any length of time. In strong contrast to the measurements on rigid objects, the lateral membrane structure appeared highly dynamic. Inaccessible nanoscopic membrane areas restricted the diffusive motion of the receptor. The comparison with a lipid anchored protein showed that the characteristics of these areas depended on the observed protein. Furthermore, it was possible to observe these areas changing shape and position on the second time scale. A consequence of the restriction by these areas was that the EGF-receptor dwelt up to 20 times longer in specific membrane regions as it would have been expected for free diffusion. Moreover, it was possible to obtain information on the dynamics of the receptor's motion on the nanometer and the micrometer scale. The analysis of these dynamics provided evidence that the diffusion of the receptor is dominated by the lipid bilayer structure of the cell membrane on short length scales, whereas the motion on long length scales is hindered by nanoscopic membrane heterogeneities. In addition, first measurements were presented that showed the dynamics of the motion of the receptor with regards to its distance to confining membrane structures. Such measurements will allow in future to test theoretical models of the molecular build-up of membrane nanostructures and to investigate hydrodynamic coupling in two-dimensional systems. In the last part of this work, possible consequences of the restricted EGF-receptor mobility were discussed. Specifically, it was analysed how lateral membrane nanostructures influence the kinetics of receptor activation as well as the velocity by which a local signal could spread laterally within the membrane. Most notably, the rate by which receptors encounter each other by diffusive motion could depend stronger on the receptor surface density as it is considered by current models.

Concluding, it can be stated that TNI-Microscopy substantially facilitates the investigation of the dynamic lateral nanostructure of the cell membrane. TNI-Microscopy thereby contributes to the understanding of the kinetics of membrane bound reactions in living cells. Moreover, there are numerous applications in soft matter physics, which will be of interest to investigate in the future.

**Keywords:**
Diffusion, Membrane, Receptor, Cell

## Zusammenfassung

In der vorliegenden Arbeit wurde eine neue bildgebende Methode (TNIM - Thermal Noise Imaging Microscopy) zur Untersuchung nanoskaliger diffusiver Bewegung in heterogenen Medien entwickelt. Die TNI-Mikroskopie wurde gezielt verwendet, um zu erforschen, ob die Beweglichkeit von Zellmembranrezeptoren durch laterale Nanostrukturen in der Membran beeinflusst wird. Die gezielte Untersuchung dieser zweidimensionalen Ultrastrukturen war bisher an lebenden Zellen aufgrund fehlender mikroskopischer Techniken kaum möglich. Bei der TNI-Mikroskopie wird die diffusive Bewegung eines Nanopartikels auf ein submikroskopisches Volumen limitiert, so dass beobachtet werden kann, ob Objekte die Bewegung des Partikels in diesem Volumen beeinflussen. Das Partikel kann somit einerseits zum Abtasten von Nanostrukturen verwendet werden, andererseits wird auch erfasst, ob die Beweglichkeit des Partikels durch hydrodynamische Kopplung zu den beobachteten Strukturen beeinflusst wird. Dadurch erfasst man gleichzeitig die Struktur nanoskaliger Objekte und die Dynamik der Partikelbewegung in Gegenwart dieser Objekte. Um die TNI-Mikroskopie zu verwirklichen, wurde ein Mikroskop gebaut, in dem eine optische Falle die diffusive Bewegung eines Sondenpartikels auf ein submikroskopisch kleines Volumen reduziert. Ein interferometrischer Detektor erfasst die Partikelposition innerhalb dieses Volumens mit Nanometergenauigkeit bei einer zeitlichen Auflösung im Mikrosekundenbereich. Zunächst wurden Experimente an starren dreidimensionalen Strukturen durchgeführt, bei denen gezeigt werden konnte, dass sich Objekte (z.B. Filamente eines Polymernetzwerkes) deutlich in Histogrammen der Positionsfluktuationen des Partikels abzeichnen. Die Position von Objekten konnte dabei mit einer Präzision von ca. 10 nm entlang aller drei Raumrichtungen bestimmt werden. Diese Experimente waren von grundlegender Bedeutung, da sie bestätigten, dass die diffusive Bewegung eines Sondenpartikels tatsächlich gezielt zur Abbildung von nanoskopischen Objekten eingesetzt werden kann. In nachfolgenden Experimenten wurde gezeigt, dass es dabei gleichzeitig möglich ist, die Dynamik der dreidimensionalen Positionsfluktuationen ebenfalls mit ca. 10 nm Auflösung zu vermessen. Existierende hydrodynamische Theorien, die die Beweglichkeit einer Kugel (Sondenpartikel) für unterschiedliche Abstände zu einer starren Grenzfläche beschreiben, konnten dabei sowohl für den Nano- wie den Mikrometerbereich bestätigt werden. Damit waren die wesentlichen Konzepte der TNI-Mikroskopie etabliert und sie konnten zur Untersuchung der Beweglichkeit von Zellmembranrezeptoren und deren Beeinflussung durch laterale Nanostrukturen eingesetzt werden. Dazu wurden Nanopartikel an den in der Membran befindlichen epidermalen Wachstumsfaktorrezeptor (EGFR - Epidermal Growth Factor

Receptor) spezifisch gebunden. Das Partikel diente dazu, die laterale Bewegung des Rezeptors beobachtbar zu machen und seine Bewegung mit Hilfe der optischen Falle auf einen submikroskopisch kleinen Membranbereich zu limitieren. Dadurch war es möglich, die diffusive Bewegung über längere Zeit in diesem limitierten Membranbereich zu beobachten. In starkem Kontrast zu den Messungen an starren Objekten ergab sich dabei ein Bild hochdynamischer lateraler Strukturen in der Zellmembran. Es zeigten sich nanoskopische Areale, die den Bereich der diffusiven Bewegung des Rezeptors beschränkten. Der Vergleich mit einem lipidverankertem Protein ergab, dass diese nanoskopischen Areale in ihrer Ausprägung vom beobachteten Protein abhängig sind. Die entwickelte TNI-Mikroskopie machte es dabei möglich, zu beobachten, dass sich Position und Größe der Areale im Sekundenbereich veränderten. Die Bewegungsbeschränkung hatte zur Folge, dass der Rezeptor für ein Beobachtungsfenster von 0.5 Sekunden in bestimmten Membranbereichen bis zu 20 mal länger verweilte, als es für freie Diffusion zu erwarten gewesen wäre. Darüber hinaus war es möglich, Informationen über die Dynamik der Rezeptorbewegung im Nanometer- und Mikrometerbereich zu gewinnen. Die Analyse dieser Dynamik ergab Hinweise, dass die Diffusion des Rezeptors auf kurzen Längenskalen von der Lipiddoppelschichtstruktur der Zellmembran dominiert, auf größeren Längenskalen jedoch von der nanoskopisch heterogenen Membranstruktur stark verlangsamt wird. Es konnten außerdem erste Messungen durchgeführt werden, welche die Dynamik des Rezeptors in Hinblick auf seinen Abstand zu den beschränkenden lateralen Strukturen erfassen. Derartige Messungen sollten es in Zukunft erlauben, theoretische Modelle für den molekularen Aufbau lateraler Membranstrukturen zu testen und hydrodynamische Kopplung auch in zwei Dimensionen direkt zu vermessen. Im letzten Teil der Arbeit wurden mögliche Konsequenzen einer durch Nanostrukturen beschränkten Beweglichkeit des EGF-Rezeptors diskutiert. Diese betreffen sowohl die Aktivierungskinetik des Rezeptors als auch die laterale Informationsausbreitung auf der Membran, die beide in komplexer Weise beeinflusst werden können. Dabei ist vor allem erwähnenswert, dass die Rate der diffusiven Rezeptorbegegnung möglicherweise in stärkerer Weise als von bisherigen Modellen berücksichtigt von der Oberflächendichte der Rezeptoren in der jeweiligen Zellsorte abhängt. Schlussfolgernd kann gesagt werden, dass die vorgestellte neue Art der Mikroskopie die Erforschung von dynamischen Membrannanostrukturen wesentlich erleichtert. TNI-Mikroskopie liefert damit einen Beitrag zum Verständnis der Kinetik membrangebundener Reaktionen in lebenden Zellen. Darüber hinaus ergeben sich vielfältige Anwendungen im Bereich der Physik der weichen Materie, deren Erforschung weit über den Rahmen dieser Arbeit hinaus ging.

**Schlagwörter:**
Diffusion, Membran, Rezeptor, Zelle

# Abbrevations

| | |
|---|---|
| AFM | Atomic Force Microscope |
| EGFR | Epidermal Growth Factor Receptor |
| FRAP | Fluorescence Recovery After Photobleaching |
| GFP | Green Fluorescent Protein |
| GFP-EGFR | GFP as the ectodomain connected to EGFR |
| GPI | Glycosyl-Phosphatidyl-Inositol |
| GFP-GL-GPI | GFP as the ectodomain connected to a GPI-anchor |
| LRO | Logarithmic Relative Occupancy |
| MSD | Mean Square Displacement |
| QPD | Quadrant Photo Diode |
| RTK | Receptor Tyrosine Kinase |
| SO | Standardised Occupancy |
| SPM | Scanning Probe Microscopy |
| SPT | Single Particle Tracking |
| STM | Scanning Tunneling Microscope |
| TNIM | Thermal Noise Imaging Microscopy |

# Contents

# 1. Introduction

## Chapter outline

The lateral mobility of membrane proteins such as growth factor receptors profoundly influences the rate of any functional process which requires movement in the plane of the membrane. It therefore is of great biological interest if membrane microdomains regulate the mobility of the membrane proteins (section 1.1) and various kinds of microscopy techniques have been used to investigate this question (section 1.2). However, the detection and characterisation of such microdomains in living cells is difficult owing to their small size and putatively transient nature. In section 1.3, technical requirements for an improved investigation of how membrane microdomains regulate membrane protein mobility are formulated and it is discussed that the lateral mobility of epidermal growth factor receptor is of particular interest regarding its molecular activation mechanism.

## 1.1 Mobility of plasma membrane proteins

Every eucaryotic cell is enclosed by its plasma membrane. The plasma membrane defines the periphery of the cell, separating its contents from the surroundings. However, to allow cells to interact with their surrounding, extracellular signals have to be transmitted across the plasma membrane to the inside of the cell. One of the fundamental mechanisms by which cells in multicellular organisms communicate is the binding of extracellular ligand molecules to specialised receptor proteins that are embedded in the plasma membrane. The receptors convert the ligand-binding event into an intracellular signal that eventually changes the state of the cell. To understand the molecular mechanism of cellular signal transduction, it is necessary to consider how receptors and other membrane bound signalling partners react with each other. In 1972, Singer and Nicolson proposed "the fluid mosaic model of the structure of cell membranes". According to this model integral membrane proteins, such as cell surface receptors, are embedded within a fluid lipid bilayer that provides the basic structure of the membrane (Fig. 1.1). It was reasoned that integral membrane proteins undergo lateral diffusion and that diffusion mediated aggregation of ligand-bound receptors with signalling partners could initiate signal transduction. In fact, numerous subsequent experimental studies provided evidence that the lateral mobility of many cell surface receptor proteins is essential for their function. This may involve aggregation of receptors preceding internalisation (Yamazaki et al., 2002) or the formation of transient or long-lived associations between cell surface receptors (Hubbard and Till, 2000) and membrane bound substrates (Tolkovsky and Levitzki, 1978). The rate of these processes is expected to be strongly influenced by the diffusive mobility of the components (Hanski et al., 1979; Goldstein et al., 1981; Lauffenburger and Linderman, 1993). In particular, the dimerisation rate of receptor tyrosine kinases such as EGFR is usually perceived to be diffusion controlled (Kholodenko et al., 1999; Park et al., 2003; Hendriks et al., 2003) and thereby directly proportional to the diffusion coefficient of the receptors (Keizer, 1987; Lauffenburger and Linderman, 1993). Consequently, there is a great interest to quantitatively determine the mobility of integral membrane proteins such as cell surface receptors (Cherry et al., 1998). However, experiments indicate that diffusion of plasma membrane proteins is not as simple as in a homogeneous lipid bilayer. First, diffusion in cell membranes is typically 10-100 fold slower than in model lipid bilayers (reviewed by Almeida and Vaz, 1995). And second, the measured diffusion coefficients depended not only on the cell type under investigation, but also on spatial and temporal resolution of the experimental technique (section 1.2). Even for one molecular species, measurements yield 100-fold differences in the measured diffusion coefficient (e.g. transferrin receptor, Sako and Kusumi, 1994; Fujiwara et al., 2002).

It is currently believed that plasma membrane "domains" on the sub-micrometer scale constrain the mobility of cell membrane proteins in a complex way (Edidin, 2001b; Vereb et al., 2003). Two lines of thought and experiment have characterised plasma membrane domains.

The first considers the domains as cages for proteins. This concept evolved out of the analysis of the membrane skeleton of erythrocytes (see Fig. 1.1E). It emphasizes that the diffusion of membrane proteins is hindered by the imperfect and fluctuating lattice of the membrane skeleton (Edidin, 1992). Such diffusion barriers could severely restrict long-range diffusion of aggregates of proteins (see Fig. 1.1D). Ritchie et al. (2003) propose that this gives the cell an efficient means to arrest the motion of a signalling complex, and hence determines with positional accuracy the direction of the signal.

The second line of thought considers plasma membrane lipid domains, which are currently of great interest to cell biologists. The most studied class of putative lipid microdomains are cholesterol and glycosphingolipid-enriched "lipid rafts". These domains are thought to act as platforms with which proteins can selectively associate, leading to their lateral segregation (Simons and Ikonen, 1997; Simons and Toomre, 2000; Maxfield, 2002). Raft association is commonly defined biochemically, i.e. raft proteins are isolated as low-density fractions from cold detergent extracts of membranes (Edidin, 2001b). These fractions are reduced or lost altogether in extracts of cholesterol-depleted membranes. The importance of rafts in signalling is therefore often inferred from the effects of cholesterol depletion on signalling processes. Thus, a chemical change in membrane cholesterol content is used to infer a physical state, the association of receptors and molecules of the signalling cascade with raft-like lipid domains. However, the physical association state and even lipid domains at all are difficult to observe in intact membranes. In fact, current experiments only allow to say that lipid domains in the plasma membrane probably are small and transient (reviewed by Edidin, 2001b; Anderson and Jacobson, 2002; Maxfield, 2002). There are several reasons why membrane structures such as lipid domains are difficult to observe, especially *in vivo*. First, these structures are usually not observed in intact cells by diffraction limited conventional fluorescence microscopy. Second, electron microscopy is limited by the effectiveness of antibodies in detection of low-abundance membrane associated proteins and only provides a *static* picture. However, membrane domains are expected to be transient and/or mobile (Edidin, 2001b). The reason is that domains formed by protein-protein, protein-lipid or lipid-lipid interactions may be only kinetically stabilised by subtle energy differences on the order of the thermal energy $k_{\mathrm{B}}T$ (Parsegian, 1995). Parameters describing *dynamics* such as lifetime of membrane domains and the rates by which proteins move in and out of domains are key for understanding the kinetics of membrane bound intermolecular reactions such as trans-autophosphorylation of EGFR (Hubbard et al., 1998). The kinetics of e.g. growth factor receptor phosphorylation reactions are not only important to understand the dynamics of a cellular response, but the

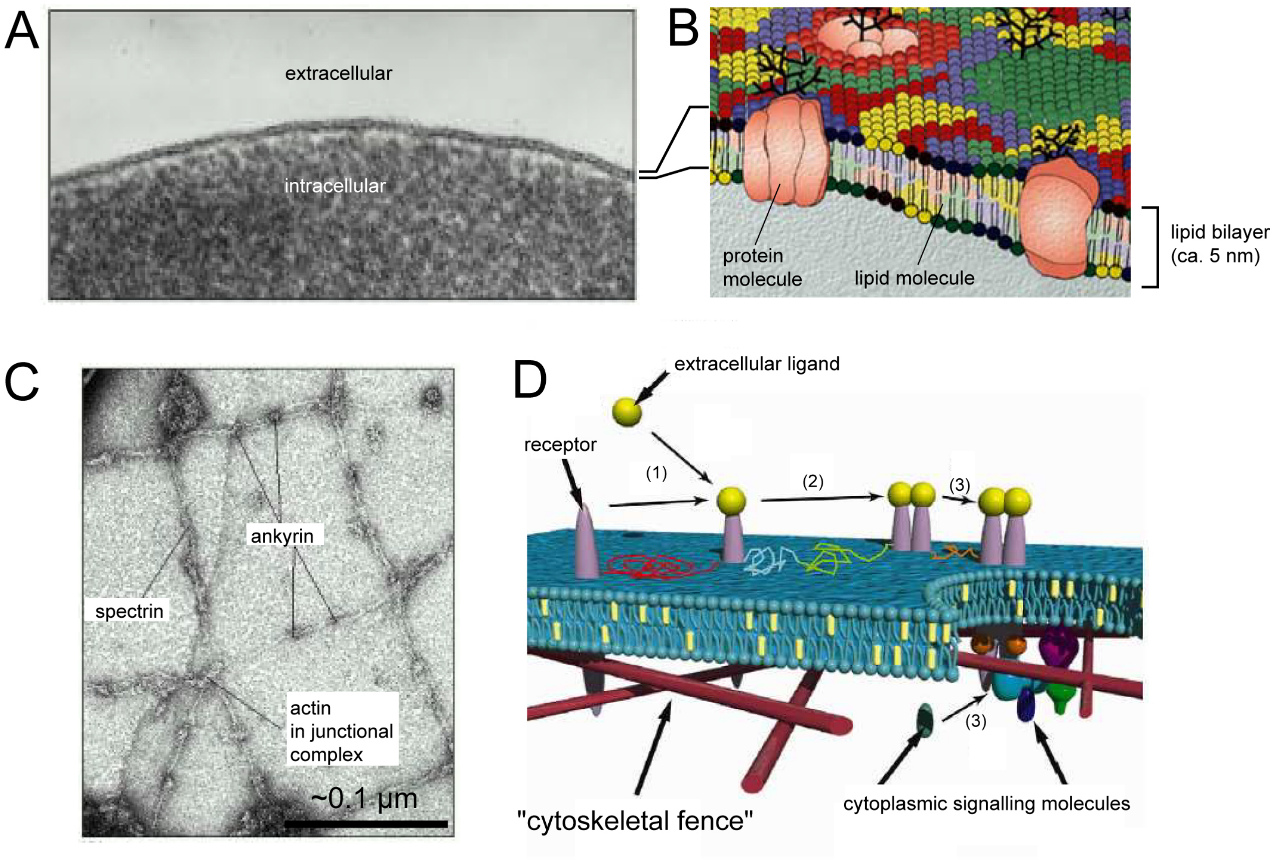

**Figure 1.1:** Scales and domains in the cellular plasma membrane. A) An electron micrograph of a plasma membrane of a human red blood cell seen in cross section (modified from Alberts et al., 2002). B) An exuberant version of "the fluid mosaic model of the structure of cell membranes" as proposed by Singer and Nicolson (1972). Different lipid species are shown in different colours and integral membrane proteins are drawn glycosylated on their extracellular portion (modified from Edidin, 2003). C) An electron micrograph of the spectrin-based cytoskeleton on the cytosolic side of the human red blood cell membrane. Spectrin dimers are linked together into a netlike meshwork by junctional complexes composed of short actin filaments. The cytoskeleton is linked to the membrane by the indirect binding of spectrin tetramers via ankyrin molecules (modified from Alberts et al., 2002). D) Oligomerisation-induced trapping model according to Ritchie et al. (2003). The cytoplasmic tail of the receptor sterically interacts with the actin-based "cytoskeletal fence". The diffusion of the receptor is therefore transiently confined to "domains" formed by the "cytoskeletal fence". Diffusion within a certain domain is indicated by differently colored position traces. (1) A receptor protein, which is diffusing between compartments in the membrane, binds a ligand molecule. (2) The receptor with ligand diffuses until it meets a similar molecule to form a dimer, slowing its transition rate between domains. (3) Signalling molecules, both membrane-bound and cytoplasmic, begin to collect around the receptor molecule forming a signalling complex. The signalling complex is now arrested in a domain owing to its size, i.e. it can no longer escape through the "cytoskeletal fence" (modified from Ritchie et al. (2003)).

kinetics of reactions can also attenuate or amplify a signal (Heinrich et al., 2002; Reynolds et al., 2003), or even change the biological output (e.g. differentiation vs. proliferation, Marshall, 1995). However, parameters describing the dynamics of membrane domains and how the presence of such domains influences the reaction kinetics of the embedded proteins can be only determined by *in vivo*.

## 1.2 Established methods to measure membrane protein mobility

Established techniques to measure membrane molecule mobility have in common that the molecular species of interest are labelled by a marker that can be tracked with a microscope. However, approaches differ in terms of spatial and temporal resolution as well as sensitivity. For instance, ”Fluorescence Recovery After Photobleaching” (FRAP) is used to observe the motion of a population of molecules on the micrometer scale, whereas ”Single Particle Tracking” (SPT) allows one to follow the motion of individual molecules on the sub-micrometer scale. Furthermore, techniques like FRAP and SPT aim to observe the inherent diffusive motion of molecules, whereas ”Surface Scanning Resistance Microscopy” (SSRM) imposes a defined path onto the motion of molecules in order to systematically scan the plasma membrane for diffusion barriers. These techniques, their limitations and the information that could be obtained about the motion of plasma membrane proteins and lipids are discussed in the following sections.

**Fluorescence Recovery After Photobleaching:** The most frequently used technique to study lateral mobility of cell surface components is FRAP, which was introduced in 1976 by Axelrod et al.. It reveals the diffusion of a population of fluorescently labelled membrane proteins or lipids from a large non-bleached membrane area, into a small photo-bleached membrane area, typically a spot of 1–2.5 $\mu$m in diameter. FRAP measurements on molecules in cellular plasma membranes typically yield diffusion coefficients in the range of 0.01–0.1 $\mu m^2/s$ (e.g. Tang and Edidin, 2003; Kenworthy et al., 2004). However, measurements in model lipid bilayers yield diffusion coefficient that are 10 to 100-fold faster, i.e. 1–10 $\mu m^2/s$ (e.g. Almeida and Vaz, 1995; Murase et al., 2004). Furthermore, one obtains information about the amount of molecules that do not move on the timescale of the experiment: the immobile fraction (e.g. Lippincott-Schwartz et al., 2003). While immobile fractions can be as large as 80% in cellular membranes, there are typically less than 20% in simple lipid bilayers (Yechiel and Edidin, 1987). Thus, FRAP experiments clearly show that the diffusion of proteins is different in the cellular plasma membrane as compared to model lipid bilayers. However, FRAP measurements are diffraction limited and monitor the average motion of many molecules. Using FRAP, it was therefore difficult to understand the slow diffusion of molecules in cellular plasma membranes. In fact, Single Particle Tracking experiments provided first evidence that there are submicrometer-scale constraints to the diffusion of plasma membrane molecules.

**Single Particle[1] Tracking:** In 1991, de Brabander et al. showed that trajectories of the motion of individual plasma membrane components can be visualised by coupling them to a 40 nm gold sphere whose center position is monitored by video-microscopy. Subsequently, numerous SPT experiments have been performed on various integral membrane molecules. These days, marker particles include gold spheres (e.g. Murase et al., 2004), latex spheres (e.g. Borgdorff and Choquet, 2002), single fluorophores (e.g. Lommerse et al., 2004), and quantum dots (e.g. Dahan et al., 2003). In general, the smaller the marker the less it influences the motion of the molecule, but the worse is the signal-to-noise in the position detection. For instance, Murase et al. (2004) reported up to ±15 nm spatial precision at up to 25 $\mu$s temporal resolution using 40 nm colloidal gold particles. Whereas Lommerse et al. (2004) achieved only ±35 nm at maximally 5 ms temporal resolution tracking yellow fluorescent protein. Using 40 nm colloidal gold, Fujiwara et al. (2002) found $D \approx 5.2\ \mu\mathrm{m}^2/\mathrm{s}$ for the transmembrane transferrin receptor in normal rat kidney fibroblastic cells at 37°C at a resolution of ±17 nm spatial and 25 $\mu$s temporal resolution. Interestingly, the apparent diffusion coefficient of the same molecule was only $D \approx 0.2\ \mu\mathrm{m}^2/\mathrm{s}$ at video rate (33 ms temporal resolution). These results suggested that, on the nanometer scale, diffusion is as fast as in a simple lipid bilayer (see Almeida and Vaz, 1995). The smaller diffusion coefficient on the 33 ms time scale was attributed to plasma membrane "domains" to which the motion of the molecule was transiently confined to. Sako and Kusumi (1994) already inferred such domains from "visual inspection" and/or statistical analysis of SPT traces. Sako and Kusumi proposed that direct interaction of the intracellular portion of the transferrin receptor with cytoskeletal structures located next to the plasma membrane caused such transient confinement to domains. However, Fujiwara et al. (2002) found that also lipids undergo "hopping motion" (infrequent transitions to adjacent membrane domains). To explain hopping motion of lipids, which can not directly interact with cytoplasmic structures, the "anchored membrane-protein picked fence model" was proposed (Fujiwara et al., 2002). Within this model, the "steric hinderance and circumferential slowing" by transmembrane proteins anchored to cytoskeletal structures is responsible for hopping motion of lipids and/or transmembrane proteins (Ritchie et al., 2003; Murase et al., 2004). Up to now, numerous SPT experiments provide evidence that most membrane molecules do

---

[1] Here, "Particle" is ment to include fluorophores. Sometimes SFM or SFVM (single fluorophore video microscopy) is used if the marker particle is a fluorophore.

not diffuse freely. Instead, they appear to be transiently confined from milliseconds to seconds within domains of tens to hundreds of nanometers (reviewed by Saxton and Jacobson, 1997). The size of domains is usually inferred from the time dependence of the molecule's mean square displacement (MSD). However, apart from the simplest cases of stable domains with stable boundaries, it is far from trivial to link an observed MSD to a particular model. The reason is that individual trajectories that could be interpreted as trapping within domains also occur in unobstructed diffusive motion with "distressingly high probability" (Saxton, 1993). Thus, the trajectory of one particle is not meaningful by itself, but a large number of particle trajectories must be recorded and analysed according to statistical criteria (Qian et al., 1991; Saxton, 1993).

**Surface Scanning Resistance Microscopy (SSRM):** In 1991, Edidin et al. labelled membrane proteins with 40 nm gold particles and dragged them across the cell surface with laser optical tweezers (Ashkin et al., 1986) until they encountered a barrier and the particle escaped the trap. The distance between such barriers was called "barrier free path" (BFP). In this study, the BFP was around 0.6 $\mu$m for a transmembrane protein with a cytoplasmic tail and around 1.7 $\mu$m for a protein with a short lipid anchor. Edidin et al. concluded that barriers on the cytoplasmic side of the plasma membrane impair the lateral movement of proteins. This interpretation was supported by experiments showing that disruption of the actin cytoskeleton or truncation of the cytoplasmic domains of transmembrane proteins increased the BFP (Edidin et al., 1994) and decreased the fraction of proteins exhibiting transient confinement as observed in SPT (Sako et al., 1998). From the truncation experiments, Edidin et al. estimated that the barriers to lateral mobility were located 2-3 nm below the cytoplasmic leaflet. More recently, Suzuki et al. (2000) employed two-dimensional scan paths in SSRM and detected barriers to lateral movement that were dynamic on a timescale of minutes. However, although two-dimensional scan paths can give an 2D image of the distribution of barriers, SSRM is most sensitive to barriers perpendicular to the scan direction, hardly sensitive to barriers parallel to the scan direction, and barriers in "intermediate orientations" likely yield signals that are not straightforward to interpret. Another limitation of SSRM is that, in order to obtain good spatial resolution, relatively stiff optical traps have to be used to minimise residual Brownian motion of the trapped particle. However, increasing trap stiffness also increases the danger that low energy barriers are destroyed or overlooked by the experiment. For instance, Suzuki et al. (2000) used a trap stiffness of around 80 fN/nm to limit the residual probe position fluctuations to about ±50 nm at 37°C. Barriers could be reliably detected[2] if the pulling force was increased by $\geq$1 pN for $\geq$100 nm. Thus, the minimal energy

---

[2] Estimated from Figure 3 in Suzuki et al. (2000).

separation of domains that could be detected was[3] $\geq 23\ k_{\mathrm{B}}T$. However, biologically relevant plasma membrane structures might be based on transient protein-protein or protein-lipid interactions that are stabilised by only few $k_{\mathrm{B}}T$ (see section 1.1) and are therefore are difficult to detect using established SSRM technology.

**Optical trap confined single particle tracking (OTC-SPT):** Optical trapping and single particle tracking techniques were also combined. Pralle et al. (2000) used an optical trap to confine the motion of a latex sphere, which was bound to a membrane protein, to a small area (radius ≤50 nm). This area was smaller than the typical distances between diffusion barriers that were inferred from SPT or have been seen with SSRM. The confinement should thereby permit to measure the mobility of plasma membrane proteins in the absence of diffusion barriers. Interestingly, diffusion coefficients of 1–5 $\mu\mathrm{m}^2/\mathrm{s}$ were obtained for various types of membrane proteins. This was the first time that diffusion in cellular membranes was found consistent the diffusion of proteins that were reconstituted in model lipid bilayers (1.7–4.8 $\mu\mathrm{m}^2/\mathrm{s}$, reviewed by Almeida and Vaz (1995)). Pralle et al. concluded that – between diffusion barriers – the plasma membrane viscosity is comparable to that of a model lipid bilayer. Furthermore, the experiments showed that the diffusive mobility of "lipid-raft" associated proteins (see section 1.1) was independent of the type of membrane anchoring and that their mobility was significantly reduced compared to non-raft proteins. Moreover, raft-associated proteins diffused as fast as non-raft proteins after cholesterol depletion (see section 1.1). An average raft radius of 26±13 nm was estimated by comparing the measured mobilities to a theoretical model by Saffman and Delbrück (1975) which connects mobility and radius of a cylindrical entity that diffuses in a membrane. These measurements provided the first evidence that lipid rafts diffuse as small entities in the plasma membrane of intact cells. However, no spatial information on constraints to diffusion of membrane proteins could be obtained using OTC-SPT.

## 1.3 Research objectives

The goal of this work is to develop a novel approach for studying Brownian motion in complex microscopic environments such as the plasma membrane in order to facilitate research on lateral mobility of membrane proteins. The physical properties of plasma membrane lateral heterogeneities that are expected to regulate membrane protein mobility (see section 1.1)

---

[3] The Boltzmann constant $k_{\mathrm{B}}$ is about $1.38 \cdot 10^{-23}$ J/K. Thus, 1 $k_{\mathrm{B}}T$ corresponds to about $4.3 \cdot 10^{-21}$ J at $T \approx 37°\mathrm{C}$ (310 K). On the other hand, 1 pN · 100 nm = $1 \cdot 10^{-19}$ J. Consequently, 1 pN · 100 nm corresponds to about 23 $k_{\mathrm{B}}T$ at 37°C.

impose some technical requirements: (i) lateral membrane heterogeneities are expected to be formed by protein-protein, protein-lipid or lipid-lipid interactions. A typical length scale in lateral membrane heterogeneities therefore is the lateral extend of individual lipids and proteins, being in the Ångström to nanometer range. (ii) When observing the 2D Brownian motion of a particle such as a membrane protein, the spatial precision $\Delta r$ is linked the to temporal resolution $\Delta t$ via the mean square displacement $\langle \Delta r^2 \rangle = 4D\Delta t$ (see section 2.2.3), where $D$ is the diffusion coefficient of the particle. Diffusion coefficients of proteins in the plasma membrane are not expected to be higher than in homogeneous model lipid bilayers, where $D$ is typically between 1 and 5 $\mu\mathrm{m}^2/\mathrm{s}$ (Almeida and Vaz, 1995). A protein with a diffusion coefficient of $D = 1$ $\mu\mathrm{m}^2/\mathrm{s}$ diffuses about 2 nm within $\Delta t = 1$ $\mu$s. Thus, tracking a protein's motion on the Ångström to nanometer scale requires a temporal resolution in the submicrosecond to microsecond range. (iii) The diffusion of membrane proteins is expected to be influenced by transient interactions with other proteins and/or lipids which may be only stabilised by energies on the order of the thermal energy $k_{\mathrm{B}}T$. Thus, a technique that aims to observe such interactions must have the corresponding sensitivity. (iv) As membrane lateral heterogeneities are expected to be transient, it is necessary to observe a membrane area at high temporal resolution and for sufficient time to capture the dynamics of these heterogeneities. And (v), as the final question is how membrane lateral heterogeneities regulate the diffusion of embedded proteins, it is advantageous to obtain *simultaneous* information on their position and structure and how they influence the diffusion of proteins.

This work aims to provide a novel microscopy technique that fulfils the above requirements, making it possible to obtain parameters relevant for the biological function of membrane bound proteins. In particular, it was chosen to study the mobility of the epidermal growth factor receptor (EGFR), because it is believed that diffusive encounters of individually diffusing EGFR can lead to trans-autoactivation (Hubbard et al., 1998), also in the absence of ligand. Detailed information on the lateral mobility of EGFR in the plasma membrane will allow accurate determination of the frequency of such diffusive encounters. Such information may help to better understand how EGFR overexpression is connected to its enhanced activation and ultimately to uncontrolled cell proliferation (Libermann, 1985; Gullick, 1991; Salomon et al., 1995). Moreover, it has been found that local stimulation of EGFR can lead to phosphorylation of EGFR in a distance of tens of micrometers from the stimulus, within tens of seconds (Verveer et al., 2000). A detailed knowledge of EGFR mobility facilitates studies of EGFR auto-activation based reaction-diffusion mechanisms that could mediate such a non-local response.

# 2. Microscope development

## Chapter outline

In this chapter, the rationale behind Thermal Noise Imaging Microscopy (TNIM) is given (section 2.1), aiming to a provide novel means of studying motion in complex microscopic environments such as the plasma membrane. The physics behind TNIM are reviewed in section 2.2 and the technical realisation of a microscope that allows one to actually perform TNIM is presented in section 2.3. The microscope features a high-resolution 3D single particle tracking scheme (Pralle et al., 1999) that however has inherent non-linearities that would hamper the interpretation of TNIM data. Thus, a novel calibration was developed (section 2.4) that corrects for non-linearities, using Brownian motion as a local calibration standard.

## 2.1 Rationale behind Thermal Noise Imaging Microscopy

The name ”Thermal Noise Imaging Microscopy” (TNIM) reflects that residual thermal position fluctuations (”thermal noise”) of a microscopic spherical particle in an optical trap are employed to scan (”image”) objects on the nanometer scale. There are several reasons why it is advantageous to use the thermal position fluctuations (diffusive motion[1]) of a particle to scan submicrometer scale objects. First, a diffusing particle only exerts thermal forces on an object, allowing the investigation of soft biological material at physiological temperatures. Second, ”diffusive scanning” is naturally isotropic and therefore well suited to investigate 3D samples such a polymer networks or the interior of a cell. And third, studying the dynamics of the scanning process itself reveals how objects influence the mobility of a particle in close

---

[1] The irregular motion of immersed microscopic particles is also called ”Brownian motion”. It is named after the botanist Robert Brown who observed erratic fluctuations of suspended pollen grains in 1827. In this work, the terms ”Brownian motion”, ”diffusive motion”, ”diffusion” and ”thermal position fluctuations” are used to describe the irregular translational motion of particles (including molecules such a proteins) owing to thermal agitation.

(nano- to micrometer scale) vicinity.

In order to make a diffusion-based scanning mechanism efficient, the motion of the particle must by confined to a region of interest, otherwise the particle "diffuses away" before the object was probed sufficiently. In the TNIM, this is achieved using a laser optical trap that can be adjusted to limit the diffusive motion of dielectric microspheres to residual thermal position fluctuations in a defined microscopic volume. TNIM has two modes of operation: in three dimensions ("3D-TNIM") and in two dimensions ("2D-TNIM") (see Fig. 2.1). In 3D-TNIM, the direct interaction of the microsphere with 3D objects is investigated. In 2D-TNIM the microsphere is specifically coupled to a membrane protein and the interaction of the protein with lateral membrane structures is probed. In 2D-TNIM, the particle serves (i) as a marker that allows one to track the protein's motion, and (ii) to confine the protein's motion (via the optical trap) to a defined microscopic membrane area.

The investigation of small and transient microscopic structures such as plasma membrane lateral heterogeneities requires high spatio-temporal resolution. In the TNIM, the laser light that is scattered from the microsphere is used to track the sphere's center position. This position detection scheme is advantageous because it allows one to track the sphere's thermal position fluctuations almost isotropically in 3D with microsecond temporal and nanometer spatial resolution (see section 2.3.2 and section 2.4)[2]. In this work, the recorded thermal position fluctuations were evaluated mainly in two ways. First, histograms of the particle's positions were computed in order to reveal the position and structure of objects that constrain the motion of the particle. In the simplest case, rigid 3D objects cause steric depletion zones, resulting in zero counts in the respective volume elements of the histogram (e.g. see Fig. 3.2). And second, the temporal dynamics of the position fluctuations were evaluated, mainly by analysing the particle's average mean square displacements within small volume (area) elements. This analysis yields the particle's local mobility, which can for instance vary due to hydrodynamic coupling to rigid 3D objects (see e.g. Fig. 3.3 or Fig. 3.5), or owing to local changes in the viscosity of the plasma membrane (see Fig. 4.12).

The development of TNIM was directed in order to investigate submicrometer-scale lateral heterogeneities in the cellular plasma membrane, which are expected to constrain the diffusion of membrane bound proteins such as epidermal growth factor receptor (see section 1.1). Tracking the motion of individual membrane proteins by attaching a marker particle is well established (SPT) and many authors have used this approach to infer the diffusive behaviour

---

[2] The "Thermal Noise Imaging Microscope" that was developed in this work also allows one to perform "Photonic Force Microscopy" (PFM). In PFM, the thermal position fluctuations of a probe particle are used to study e.g. mechanical properties of single molecules. In parallel to this work, other members of our laboratory used PFM for interesting studies on the motor molecules kinesin (Jeney et al., 2004) and myosin (Scholz et al., 2004).

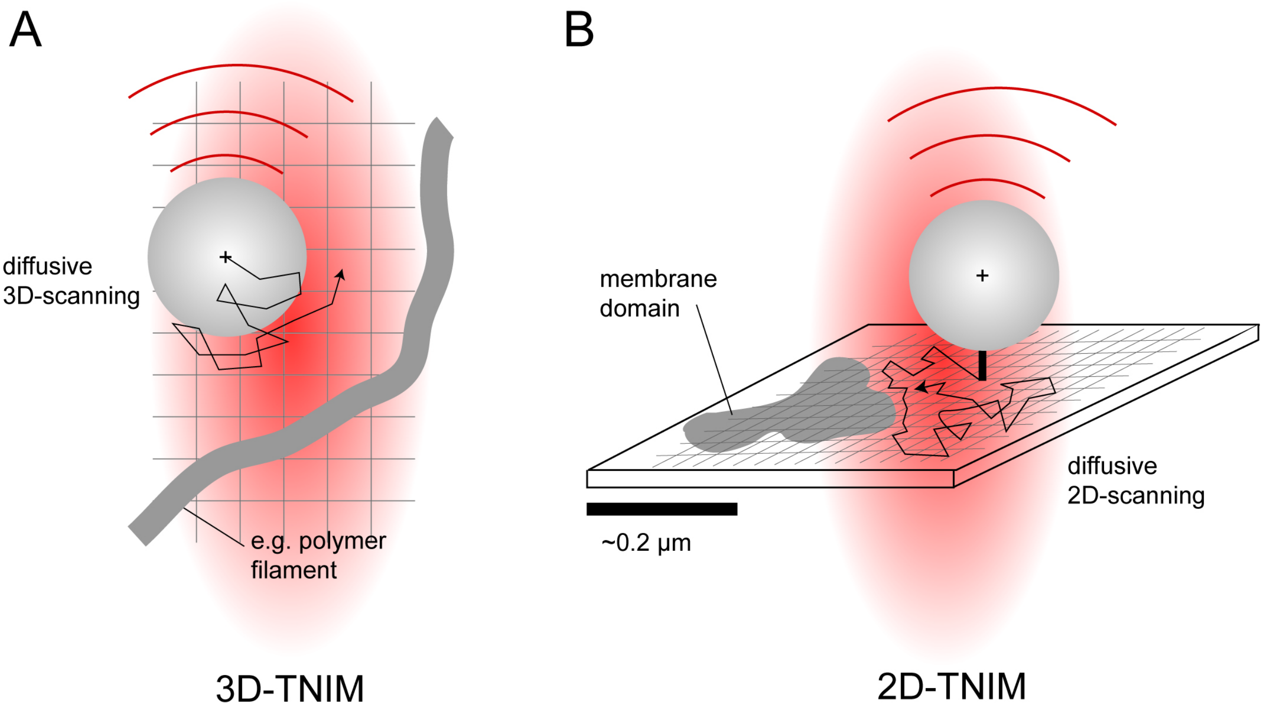

**Figure 2.1:** Thermal Noise Imaging Microscopy. A) 3D-TNIM. A weak optical trap confines the thermal position fluctuations (black arrow) of an immersed microsphere to a microscopic volume. The grey gradient depicts the focussed infra-red laser that forms the optical trap. The position of the particle center is tracked with nanometer spatial and microsecond temporal resolution using scattered trapping laser light (red solid lines). Due to the optical trap there exists a defined expectation for the frequency by which each volume (2D: area) element (indicated as grey grid) is visited by the diffusing particle. Objects that restrict the motion of the particle can therefore be reconstructed from the recorded 3D path of the particle's motion. Furthermore, analysing the displacements of the particle gives information on its local mobility, which can change due to e.g. hydrodynamic coupling to other objects. B) 2D-TNIM. In 2D-TNIM, the sphere is specifically coupled to a membrane protein of interest. Here, the sphere serves (i) as a marker particle that permits the tracking of the molecule's motion on the molecular scale and (ii) to confine the diffusion of the molecule via the optical trap. However, in 2D-TNIM the size of the molecule determines the membrane structures that can be imaged and not the size of the sphere as in 3D-TNIM. Thus, 2D-TNIM permits the imaging of nanoscale membrane domains. For instance, domains that are not accessible to the protein will be seen as less visited areas in a 2D position histogram.

of plasma membrane proteins on the submicrometer scale (see section 1.2). However, one SPT trajectory is not meaningful by itself, but a large number of particle trajectories must be recorded, and analysed according to statistical criteria (Qian et al., 1991; Saxton, 1993). This is different in 2D-TNIM, because the confinement of the diffusive motion via the optical trap ensures that the molecule probes the same membrane area over a long time. Thus, TNIM makes it possible to obtain statistically significant information ("images") of submicrometer-scale properties of the plasma membrane in one experiment. The motion of membrane proteins as confined by an optical trap has already been studied before (Pralle et al., 2000; Oddershede et al., 2002). However, the thermal position fluctuations were studied with regards to the *average* mobility of the protein within the accessible area, analysing the position autocorrelation function (Pralle et al., 2000) or the power spectral density of the recorded position fluctuations (Oddershede et al., 2002). This is fundamentally different in the TNIM as the high spatio-temporal resolution of the position detection makes it possible to detect spatial differences in the motion of the protein *within* the accessible area, allowing the imaging of membrane lateral heterogeneities on the submicrometer-scale.

In chapter 3, 3D-TNIM experiments are presented, which demonstrate that the TNIM makes it possible to obtain simultaneous information on the structure of objects that exert diffusion constraints and on the mobility of the probe particle in the vicinity to these objects. These experiments mainly served as a means of establishing the TNIM technique for the purpose of applying it in chapter 4 to study membrane protein mobility. However, 3D-TNIM is interesting on its own, one reason being that the optical tweezers hold the probe particle without mechanical connection to the microscope frame. Thus, given the sample is transparent for the trapping laser, the particle can be positioned within complex three-dimensional objects such as polymer networks. This is not possible using conventional Scanning Probe Microscopes (SPMs) such as the Atomic Force Microscope (AFM, Binnig et al. (1986)), the Scanning Tunnelling Microscope (STM, Binnig et al. (1982)) or the Scanning Near-field Optical Microscope (SNOM, Pohl et al. (1984)), because the positioning of the probe requires a stiff physical connection of both the probe (STM tip, AFM tip, or optical fibre) and the sample with the microscope frame. As this mechanical connection limits conventional SPMs to imaging of surfaces, there have been already some attempts to build a SPM based on optical tweezers (Malmquist and Hertz, 1992; Ghislain and Webb, 1993; Florin et al., 1997). However, these authors used a conventional raster scanning strategy, i.e. they moved the optical trap in steps and inferred the object properties from the average position of the trapped particle at each trap position. Such scanning resulted in only mediocre spatial resolution, because, owing to the thermal position fluctuations of the particle, an entire contact area was probed instead of a single point for each position of the optical trap. This problem is solved in 3D-TNIM,

because high-resolution tracking of the particle *within* the optical trap permits one to actually employ the thermal position fluctuations as a "natural 3D scanner".
Summarising, the TNIM makes it possible to image soft (biological) objects and simultaneously provides information on how the mobility of the probe is influenced by the presence of these objects. Moreover, both the object's structure and the probe's mobility are obtained isotropically in 3D and within 3D objects (given that the objects are transparent to the trapping laser). It is therefore expected that TNIM will become a general tool in various areas of research such as soft matter physics and life sciences. In particular, TNIM is well suited in order to investigate the mobility of proteins in their plasma membrane environment on the submicrometer-scale.

## 2.2 Physical principles

The basic ideas behind TNIM were outlined in section 2.1. Here, underlying physical principles are reviewed in more detail. This includes a discussion of the physical forces that govern the diffusive motion of an immersed microsphere in an optical trap (section 2.2.1) as well as the presentation of the *Langevin equation* (section 2.2.2), which is the corresponding equation of motion and which reveals important time-scales in the motion of the particle. Furthermore, the *Langevin equation* served as a basis for computer simulations of the particle's motion (see Appendix A). In section 2.2.3, the mean square displacement (MSD) of the particle's motion is discussed. Analysis of the MSD permits one to determine a diffusion coefficient from experimentally obtained position time traces and the MSD reports on the trapping forces in the optical trap. Finally, the theoretically expected distribution of the thermal position fluctuations of the trapped particle is examined (section 2.2.4).

### 2.2.1 Thermal and optical forces

The operating principle of TNIM is based on the thermal position fluctuations (Brownian motion) of an immersed micro-particle in an optical trap. Optical traps generate forces, $\vec{F}_{optical}$, by the use of a strongly focused beam of light in order to capture and move objects, which can range in size from tens of nanometers to tens of micrometers. Since their introduction by Ashkin et al. (1986), optical traps have become an important tool for research in the fields of biology, physical chemistry and soft condensed matter physics (Grier, 2003). In conventional optical tweezers applications, residual Brownian motion of the particle within the optical trap imposes a limiting factor for the spatial precision in positioning the particle. In TNIM, however, especially weak optical tweezers are used to allow for large thermal position fluctuations. These position fluctuations are driven by the interaction of the particle with the molecules of the surrounding fluid, $\vec{F}_{fluid}$. $\vec{F}_{fluid}$ is usually split into two parts (Uhlenbeck and Ornstein, 1930; Chandrasekhar, 1943), a random force $\vec{F}_{thermal}$ that maintains the irregular (Brownian) motion of the immersed particle, and a friction force $\vec{F}_{friction}$. For a spherical particle with radius $a$ the friction force is governed by Stokes' law:

$$\vec{F}_{friction} = -\gamma \partial \vec{r} / \partial t \tag{2.1}$$

in which the viscous drag $\gamma = 6\pi\eta a$, the viscosity of the immersion[3] fluid is $\eta$, and the particle position is $\vec{r}$. In this work, the time interval at which successive particle positions can be measured is $\delta t \geq 10^{-6}$ s. On the other hand, the time scale of collisions of the sphere with individual fluid molecules is many orders of magnitude smaller (Chandrasekhar (1943) gives $10^{-21}$ s). Consequently, the observed motion of the particle is the net effect of a large amount of collisions suffered during $\delta t \geq 10^{-6}$. It is therefore reasonable to assume (Wang and Uhlenbeck, 1945) that (i) there is no correlation in magnitude and direction of $\vec{F}_{thermal}(t + \delta t)$ and $\vec{F}_{thermal}(t)$, and (ii) the magnitude of $\vec{F}_{thermal}(t)$ is Gaussian distributed with zero mean. An explicit implementation of such a thermal force is given in chapter A, where confined Brownian motion was simulated.

The forces that the optical trap exerts on the particle, $\vec{F}_{optical}$, can be split up into two parts as well (Visscher and Brakenhoff, 1991; Rohrbach and Stelzer, 2002b), the scattering force $\vec{F}_{scatter}$, and the gradient force $\vec{F}_{gradient}$. $\vec{F}_{scatter}$ takes into account the radiation pressure that the light exerts on the particle, whereas $\vec{F}_{gradient}$ considers how dipoles, which are induced in the particle, interact with the electrical field gradient in the focus. The scattering force accelerates the particle along the direction of light propagation (optical axis, $z$) and the gradient force accelerates the particle to the point of maximal intensity (the geometrical center of the focus), see Fig. 2.2A. In the absence of the thermal forces, $\vec{F}_{scatter} = \vec{F}_{gradient}$ is the position where the particle would rest ("trap center"). Experimental (Florin et al., 1997; Tischer et al., 2004) and theoretical (Rohrbach and Stelzer, 2002b) investigations have shown that, close to the trap center, the optical forces are well approximated by three orthogonal forces derived for a harmonic trapping potential:

$$\vec{F}_{optical}(\vec{r}) = -\vec{\nabla} U_{optical}(\vec{r}), \quad U_{optical}(\vec{r}) = \frac{1}{2}(k_x x^2 + k_y y^2 + k_z z^2) \tag{2.2}$$

The force constants $k_x, k_y, k_z$ can be adjusted by changing the intensity of the trapping laser light. In this work, force constants on the order of 1 fN/nm were used. Because the intensity

---

[3] In this work, experiments were mainly performed in water at about 22°C. The viscosity of water at 22°C is $\eta \approx 0.95 \cdot 10^{-3}$ (Dean, 1985).

gradient in an optical focus is more shallow along the optical axis, $k_z$ is typically weaker than $k_x$ and $k_y$. Further, $k_x$ and $k_y$ can differ up to 40% due to the polarisation of the trapping laser (Rohrbach and Stelzer, 2002b).

### 2.2.2 Langevin equation and timescales of motion

The Brownian motion of a particle in the presence of external forces, $\vec{F}_{external}(\vec{r}, t)$, can be described by the Langevin equation (Chandrasekhar, 1943):

$$m\frac{\partial^2 \vec{r}}{\partial t^2} = -\gamma\frac{\partial \vec{r}}{\partial t} + \vec{F}_{thermal}(t) + \vec{F}_{external}(\vec{r}, t) \tag{2.3}$$

An important timescale in the Langevin equation is the *momentum relaxation time* $\tau_m = m/\gamma$, where $m$ is the mass of the particle and $\gamma$ is the viscous drag. The momentum relaxation time is the timescale for the decay of the particle's velocity due to friction. For times much longer than $\tau_m$ the motion is dominated by frictional forces and the inertial force, $\vec{F} = m\ddot{\vec{r}}$, can be neglected, i.e. overdamped motion (Uhlenbeck and Ornstein, 1930; Chandrasekhar, 1943; Wang and Uhlenbeck, 1945; Kubo, 1966). Polystyrene microspheres that are dispersed in water at ≈22°C have a momentum relaxation time in the range of nanoseconds[4] The timescale at which particle displacements can be tracked with the TNIM is technically limited to the microsecond range (section 2.3.2). Inertial forces therefore only play a minor role in the observed motion of the particle. Neglecting the term $m\ddot{\vec{r}}$ in Equation (2.3) yields the following equations of motion:

$$\gamma\frac{\partial r_i}{\partial t} = F_{thermal}(t) - k_i r_i, \; i \in \{x, y, z\} \tag{2.4}$$

The external force has been replaced by the respective component of the optical force (see Equation (2.2)). Now, another important timescale becomes evident: the *position correlation time* $\tau_i = \gamma/k_i$. This is the timescale on which a displaced particle would move to the trap center in the absence of the thermal force. In this work, the position correlation times are in the millisecond range and therefore experimentally accessible[5] The position correlation time plays a central role in Brownian motion of a particle in an optical trap as will become clear in the next section.

---

[4] The mass is calculated by $m = 4/3\pi\rho a^3$. The density of polystyrene is ca. 1.06 g/cm$^3$. The radius of the spheres that were used in this work was maximally $a = 280$ nm. The viscous drag is $\gamma = 6\pi\eta a$. The viscosity of water at ≈22°C is $\eta \approx 0.95 \cdot 10^{-3}$. For these values one obtains $\tau_m = m/\gamma \approx 20$ ns.

[5] For instance, consider a sphere with radius $a = 280$ nm that is trapped with forces constants of ≈ 1 fN/nm in water at ≈22°C. The position correlation times are $\tau \approx 5$ ms.

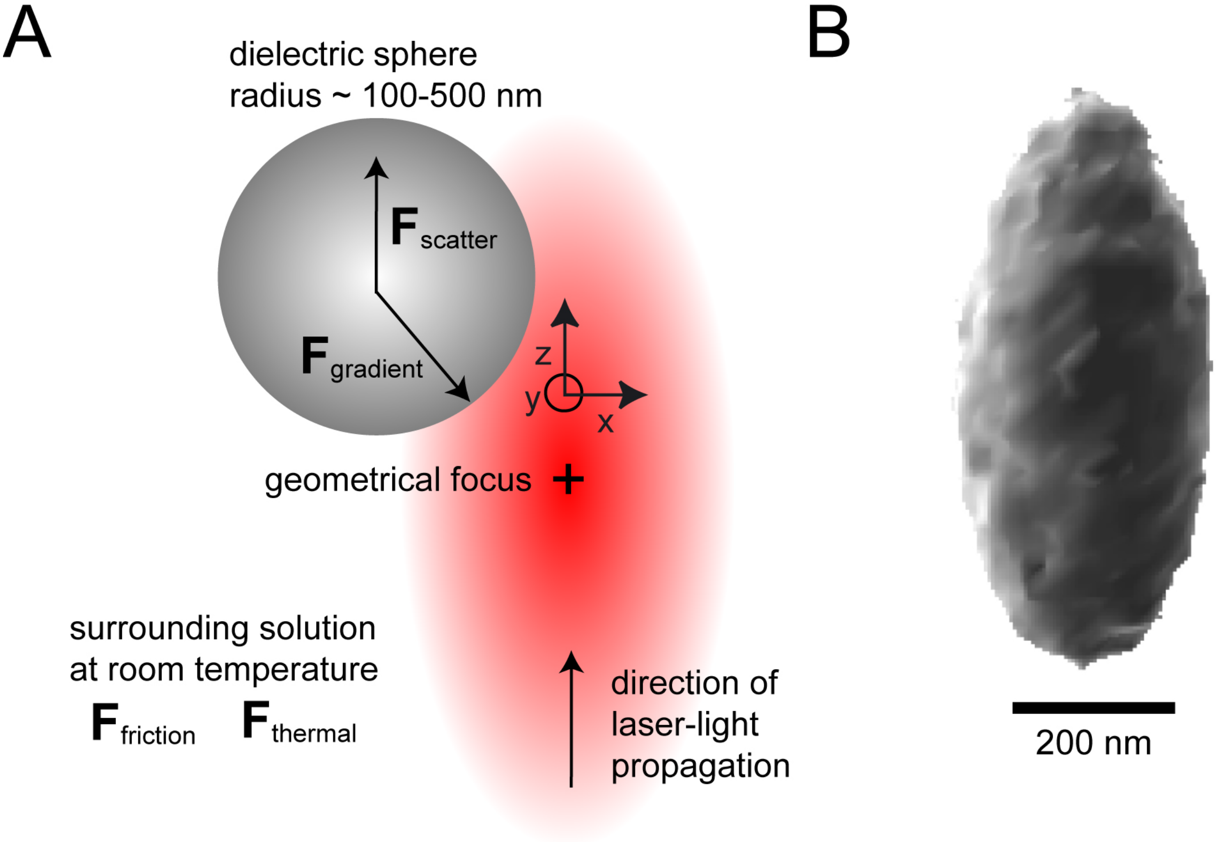

**Figure 2.2:** Forces dominating the motion of an immersed microsphere in an optical trap. A) The ellipsoidal red gradient schematically depicts the light intensity distribution of the focussed trapping laser. The origin of the $(x, y, z)$ coordinate system marks the "trap center". The trap center is the position where the optical forces $\vec{F}_{gradient}$ and $\vec{F}_{scatter}$ cancel out each other. The surrounding fluid causes thermal fluctuations of the particle's position around the trap center. B) 3D isosurface of a histogram of thermal position fluctuations of a trapped 216 nm latex sphere that were recorded for 12 s at 100 kHz at ≈22°C, using the TNIM. The sphere "explored a trapping volume" of about 300x120x120 nm$^3$. The positions are distributed according to Boltzmann statistics. The isosurface shown corresponds to an energy of ca. 3 $k_\mathrm{B}T$ above the trap center. The roughness of the isosurface is of statistical nature, it reflects the erratic thermal position fluctuations by which the particle samples the trapping volume.

### 2.2.3 Mean square displacement and diffusion coefficient

The calculation of MSD from a time series of a particle's position is a common way to quantify Brownian motion. The MSD along one axis $i \in \{x, y, z\}$ for a lag time $\Delta t$ is defined as (e.g. Box and Jenkins, 1970):

$$\begin{aligned} \mathrm{MSD_i}(\Delta t) &\equiv \left\langle (r_i(t+\Delta t) - r_i(t))^2 \right\rangle \\ &= \frac{1}{N}\sum_{k=1}^{N} (r_i(k\,\delta t + \Delta t) - r_i(k\,\delta t))^2 \end{aligned} \tag{2.5}$$

where, $N = t/\delta t$, is the number of positions that are measured during the recording time $t$ at sampling rate $\delta t^{-1}$. The MSD for free Brownian motion along one axis is (Einstein, 1905):

$$\mathrm{MSD}(\Delta t) = 2D\Delta t \tag{2.6}$$

with the *diffusion coefficient* $D = k_\mathrm{B}T/\gamma$. If the motion is isotropic, the MSD in 2D is given by $2 \cdot 2D\Delta t$ and by $3 \cdot 2D\Delta t$ in 3D. However, if Brownian motion is confined by harmonic forces such as in the optical trap, the MSD is given by (Chandrasekhar, 1943):

$$\mathrm{MSD_i}(\Delta t) = \sigma_i^2(1 - \exp(-\Delta t/\tau_i)) \approx \begin{cases} 2D\Delta t & \text{for } \Delta t \ll \tau_i \\ \sigma_i^2 & \text{for } \Delta t \gg \tau_i \end{cases} \tag{2.7}$$

where $\sigma_i = \sqrt{2k_\mathrm{B}T/k_i}$ is the width of the position distribution and $\tau_i = \gamma/k_i$ is the position autocorrelation time (see Fig. A.1B for a typical MSD in an optical trap). Thus, for lag times $\Delta t$ much shorter than the position autocorrelation time, the motion is dominated by thermal forces and nearly free diffusive motion is observed (compare to Equation (2.6)). For lag times much longer than the position autocorrelation time, the MSD is limited by $\sigma_i^2$, because the particle's Brownian position fluctuations are confined to the optical trap.

### 2.2.4 Boltzmann distributed particle positions

The probability density $\rho(\vec{r})$ for finding a Brownian particle at position $\vec{r}$ in a potential $U(\vec{r})$ is determined by Boltzmann statistics (e.g. Risken, 1989):

$$\rho(\vec{r}) = C\exp\left(-\frac{U(\vec{r})}{k_\mathrm{B}T}\right), \text{ with } C^{-1} = \int \exp\left(-\frac{U(\vec{r})}{k_\mathrm{B}T}\right)\, d^3x \tag{2.8}$$

where the integral over the whole space normalises the density. The probability $p(\vec{r}_0)$ to find the particle in a cubic volume element with center coordinates $\vec{r}_0 = (x_0, y_0, z_0)$ and edge length

$\xi$ is given by:

$$
\begin{aligned}
p(\vec{r}_0) &= \int_{x_0-\xi/2}^{x_0+\xi/2} dx \int_{y_0-\xi/2}^{y_0+\xi/2} dy \int_{z_0-\xi/2}^{z_0+\xi/2} dz\ \rho(\vec{r}) \\
&\approx C \exp\left(-\frac{U(\vec{r}_0)}{k_{\mathrm{B}}T}\right) \xi^3 \qquad (2.9)
\end{aligned}
$$

The approximation improves the smaller the volume element is as compared to the length scale on which the Boltzmann factor changes significantly. To calculate the position distribution $n(x, y, z)$ for the thermally fluctuating particle in the optical trap, Equation (2.2), Equation (2.9), and Equation (2.8) are combined:

$$
n(x, y, z) = N \frac{\sqrt{k_x k_y k_z}}{(2\pi k_{\mathrm{B}}T)^{\frac{3}{2}}} \exp\left(-\frac{k_x x^2 + k_y y^2 + k_z z^2}{2k_{\mathrm{B}}T}\right) \xi^3, \qquad (2.10)
$$

where, $N = t/\delta t$, is the number of position measurements taken during the observation time $t$ at sampling rate $\delta t^{-1}$. A position isosurface, i.e. $n(x, y, z) = constant$, therefore has an ellipsoidal shape. It is elongated along the optical axis, because the axial force constant $k_z$ is typically weaker than the lateral $k_x$ and $k_y$ (see section 2.2.1). Fig. 2.2B shows a measured position isosurface.

For investigations in the plane of the plasma membrane (2D-TNIM), only the $(x, y)$ position distribution is of interest. Projecting the 3D position distribution onto the $(x, y)$-plane yields:

$$
n(x, y) = N \frac{\sqrt{k_x k_y}}{2\pi k_{\mathrm{B}}T} \exp\left(-\frac{k_x x^2 + k_y y^2}{2k_{\mathrm{B}}T}\right) \xi^2 \qquad (2.11)
$$

The distribution of particle positions are expected to be governed by Equation (2.10) for 3D-TNIM and by Equation (2.11) for 2D-TNIM, if the motion of the particle is dominated by the optical trap. Objects that hinder the diffusion of the sphere are detected as significant changes in the particle's position distribution. The optical trapping forces $(k_x, k_y, k_z)$ determine the frequency by which certain parts of an object will be sampled. In general, positions in the trap center are sampled more frequently than positions at the periphery of the trap. The statistical accuracy by which information on an object is obtained is consequently highest close to the trap center. Positions far away from the trap center are infrequently sampled resulting in noisy data[6].

---

[6] This aspect of Thermal Noise Imaging Microscopy is discussed in more detail in section 4.2

## 2.3 Microscope set-up

### 2.3.1 General requirements

The Thermal Noise Imaging Microscope comprises the following features: (i) an optical trap that confines the Brownian motion of the probe particle to a microscopic volume; (ii) a detection scheme to track the particle's thermal position fluctuations with nanometer spatial and microsecond temporal resolution; (iii) a device to position the optical trap relative to the sample with millimetre lateral[7] and tens of micrometers axial travel; and (iv) a conventional light microscope to control the positions of probe and sample on the micrometer scale. The overall design of the microscope (e.g. mechanical integration of individual parts) was particularly challenging, because precision in the nanometer range should be achieved for measurements on biological samples. The following sections give the implementation of the main components of the TNIM and discusses their performance. An overview of all components is depicted in Fig. 2.3. Additional information on the set-up, which was developed at EMBL Heidelberg in collaboration with Dr. Alexander Rohrbach, can be found in a recent publication (Rohrbach et al., 2004).

### 2.3.2 Implementation and performance of components

#### Optical trap

**I**mplementation: An infrared ($\lambda$=1064 nm) laser beam (Laser IR, in Fig. 2.3) (IRCL-1000-1064-S, CrystaLaser, Reno, USA) is expanded 20x by a telescope (T) (S6ASS2320/126, Sill Optics, Germany) and reflected by a dicroic shortpass beam splitter (BS1) (Beamsplitter 725 DCSPXR, AHF analysentechnik, Germany), yielding a two-fold overillumation of the back focal plane of the water immersion objective lens (OL) (UPlanApo 60x NA1.2, Olympus, Japan). The objective lens focuses the IR-light through the coverslip into solution to generate the optical trap. To adjust the trapping power, the IR-light can be attenuated by a variable neutral-density filter (NDF).

**P**erformance: Laser powers between 50 mW and 100 mW have often been used for optical trapping applications in cell biology. It is however desirable to achieve stable trapping with laser powers below 10 mW to minimize cell damage caused by high-energy near-infrared lasers (e.g. König et al., 1996; Neuman et al., 1999; Celliers and Conia, 2000). Here an excellent trapping efficiency was achieved by a well centered 2-fold overillumination of the objective lens. Thus, throughout this work less than 5 mW total laser power were sufficient to confine the

---

[7] The large lateral travel is necessary to locate cells that are appropriate for 2D-TNIM experiments.

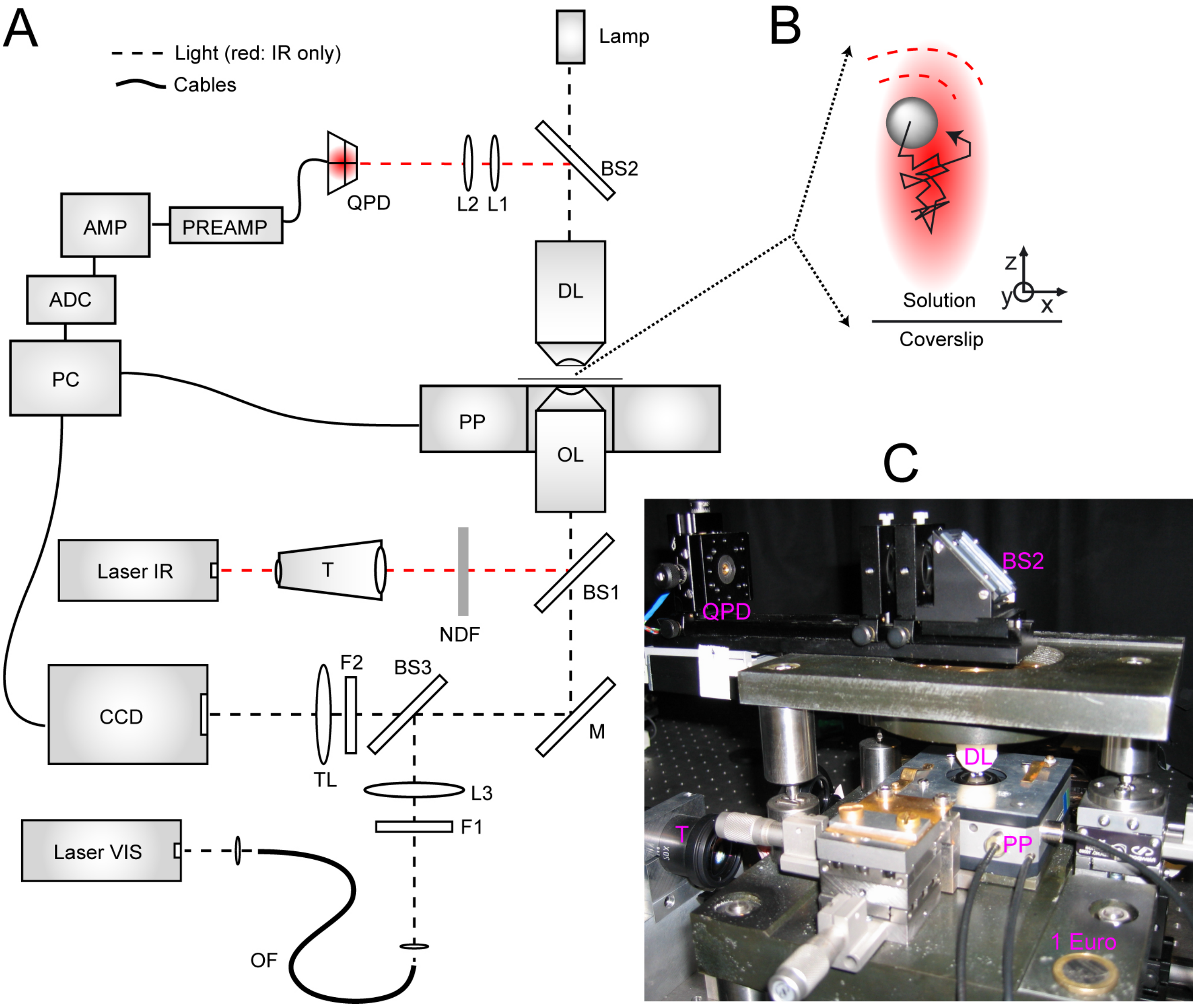

**Figure 2.3:** The Thermal Noise Imaging Microscope. A) Schematic overview. Abbreviations: analog digital converter (ADC), beam splitter (BS), charge coupled device camera (CCD), detection lens (DL), filter (F), infra-red (IR), lens (L), objective lens (OL), personal computer (PC), amplifier (AMP), pre-amplifier (PREAMP), piezo positioner (PP), quadrant photo diode (QPD), tube-lens (TL), visual light (VIS). B) Microsphere undergoing Brownian motion (zig-zag arrow) confined by the optical trap (red gradient depicts infra-red light intensity distribution in the focus). Scattered light (dashed lines) is used to determine the 3D position of the sphere in the trap (see text). C) Photograph of central microscope part.

Brownian motion of probe-spheres between 200 nm and 600 nm in diameter to an ellipsoidal volume of about ±300 nm extend in $z$ and ±150 nm in $x, y$ (see e.g. Fig. 2.2B or Fig. 2.9B). Typical force constants were $k_z$<1 fN/nm and $k_x, k_y$<4 fN/nm. For all TNIM data shown the maximal displacement of the probe from the trap center was less than 200 nm laterally and 400 nm axially. The maximal optical forces acting on the probe sphere were consequently less than 1 pN throughout this work.

### Probe position detection

**I**mplementation: Part of the IR-light is scattered by the particle in the optical trap. Scattered and un-scattered light are collected by a water dipping detection lens (DL) (IR-Achroplan 63x NA0.9, Carl Zeiss, Germany) and projected by a dicroic shortpass beam splitter (BS2) (Beamsplitter 725 DCSPXR, AHF analysentechnik, Germany) and two lenses (L1, L2) onto a InGaAs quadrant photo diode (QPD) (G6849, Hamamatsu Photonics, Japan). On the QPD, scattered and unscattered light generate an interference pattern that reports the probe position. The QPD signals are fed into a custom-built preamplifier (PREAMP) (Öffner MSR-Technik, Germany) which provides two differential signals between the segments and one signal that is proportional to the total light intensity. Subsequently, differential amplifiers (AMP) (Öffner MSR-Technik, Germany) adjust the preamplifier signals for optimal digitalizing by the data acquisition board (DAQ) (PCI-6110, National Instruments, USA) that is connected to a standard PC.

**P**erformance: To follow the three-dimensional Brownian motion of the trapped particle, the scattering of the strongly focused trapping laser on the particle is exploited. The scheme is based on a method that was first described by Pralle et al. (1999). A detailed theory of the signal generating optical processes can be found in Rohrbach and Stelzer (2002a). Here, the experimental characterisation of the specific implementation is given, with an particular emphasis on noise sources that limit the precision of the position detection. The response of the detector was measured by scanning an immobilised[8] 560 nm sphere across the focus along the $x$,$y$, and $z$ axis as shown in Fig. 2.4. For small displacements from the focal center, the differential signals of the QPD are uniquely related to the respective lateral $(x, y)$ position of the particle, while the total light intensity reports the axial $(z)$ displacement. Thus, the QPD signals can be used to determine the position of the particle in 3D within a range of about ±300 nm laterally and about ±700 nm axially. This is sufficient for the applications in this work because the optical trap was adjusted to confine the Brownian motion to smaller amplitudes (e.g. Fig. 2.9B). However, it can be also seen that the signal does in general not depend linearly on the displacement. Especially for larger displacements detector calibra-

---

[8] Spheres were immobilised as described in section D

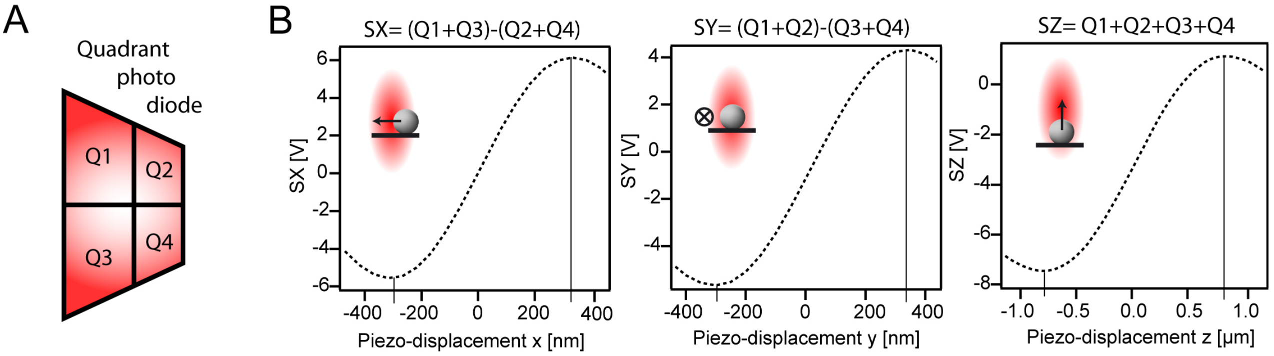

**Figure 2.4:** Particle position detection system. A) Schematic of QPD with indicated interference pattern. B) Detector response. Dashed lines show the recorded position signal obtained by scanning the focus over an immobilized 560 nm sphere as indicated in the insets. Between solid lines, position and signal are uniquely related.

tion by a single calibration factor would yield mediocre results. Thus, a novel method for in situ determination and correction of position detection nonlinearity was developed and used throughout this work (section 2.4 and Tischer et al. (2004)).

The position of the particle is deduced from the interference pattern on the QPD. Consequently, everything that, apart from a movement of the particle changes the interference pattern adds noise to the position detection. Typical noise sources are laser intensity fluctuations, electronic noise, and mechanical instabilities of the microscope. The latter causes mainly low frequency noise (drift) and is discussed in section 2.3.2. Here, the high-frequency noise is determined from the mean square displacement (MSD) of the probe particle. The MSD is expected to increase linear with $\Delta t$ for lag times $\Delta t \ll 1$ ms (Equation (2.7)). The maximal data acquisition rate is limited by the amplifier electronics to 1 MHz. Thus, the smallest lag time before the next particle position can be measured is 1 microsecond. It can be seen most obviously in the MSD of the 250 nm sphere (Fig. 2.5A) along the $z$-axis, that a line-fit is only successful if a constant offset is taken into account[9]. For the 560 nm sphere the offset is less because the relative amount of scattered light and thus the signal on the QPD is larger. Interestingly, the noise that is found in *absence* of a sphere has similar magnitude as the offset found in *presence* of the sphere. This indicates that the noise is not correlated with the sphere's motion.

These observations lead to the following conclusions: First, the absolute position measurement of the probe has an uncertainty that can be estimated from the noise-offset in the measured MSD. For the 250 nm sphere the absolute position can be measured with a precision (± one standard-deviation) of about ±5 nm axially and about ±1 nm laterally. For the 560 nm sphere

---

[9] The noise offset is largest in the $z$-signal, while the lateral positions, which are determined from the difference signals on the QPD are less affected. This indicates that the noise mainly originates from fluctuations in the total laser intensity.

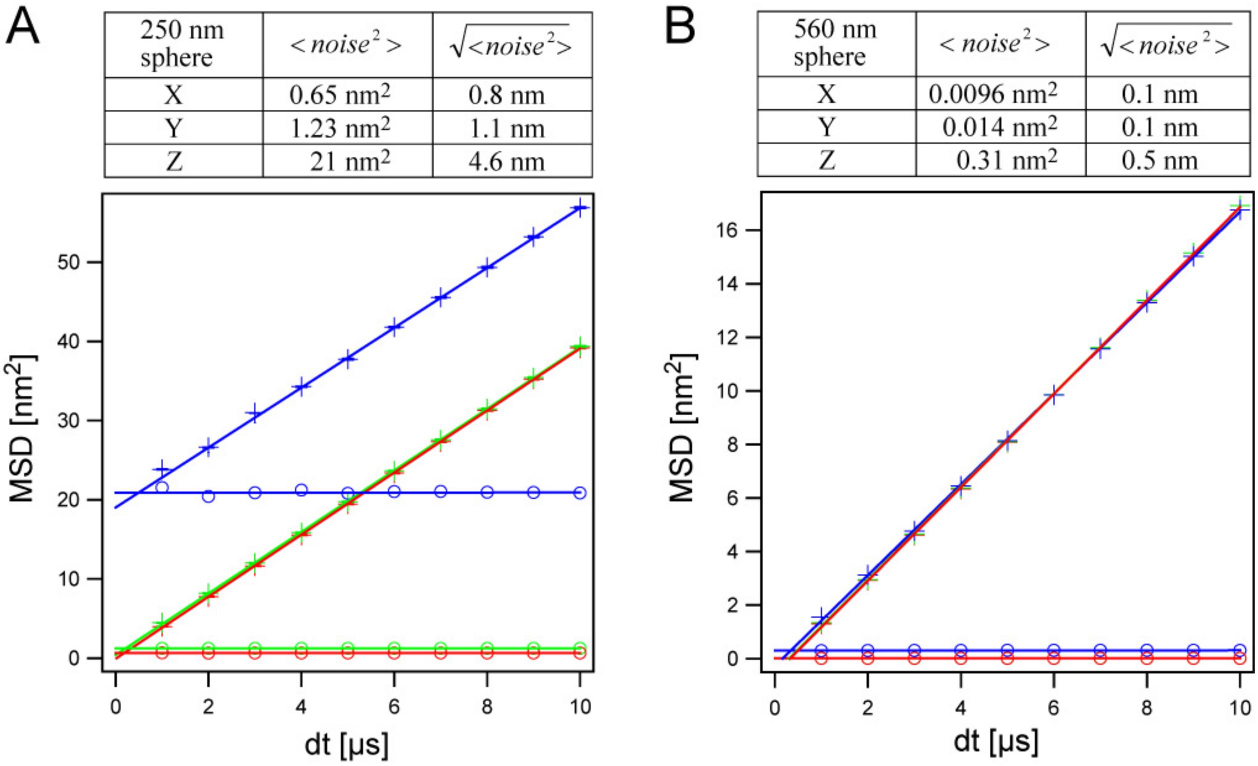

| 250 nm sphere | $<noise^2>$ | $\sqrt{<noise^2>}$ |
|---|---|---|
| X | 0.65 nm$^2$ | 0.8 nm |
| Y | 1.23 nm$^2$ | 1.1 nm |
| Z | 21 nm$^2$ | 4.6 nm |

| 560 nm sphere | $<noise^2>$ | $\sqrt{<noise^2>}$ |
|---|---|---|
| X | 0.0096 nm$^2$ | 0.1 nm |
| Y | 0.014 nm$^2$ | 0.1 nm |
| Z | 0.31 nm$^2$ | 0.5 nm |

**Figure 2.5:** High frequency noise in the position detection. A) Crosses: MSD calculated from the calibrated QPD signals of the Brownian motion of a trapped 250 nm (diam.) latex sphere. Circles: MSD calculated from calibrated QPD signals in the absence of a trapped particle, non-zero values originate from instrument noise. Solid lines are line fits. B) Same as in (A) for a 560 nm (diam.) latex sphere. (red: $X$, green: $Y$, blue: $Z$).

the axial precision is about ±0.5 nm, while the lateral precision is about ±0.1 nm. Second, because the noise adds a constant offset to the MSD, the diffusion coefficient $D$ of the probe can be still accurately determined from the slope of the MSD even at short lag times.

### Sample positioning

**I**mplementation: The sample is moved in three dimensions by a piezo positioner (PP) (Tritor 102cap, Piezosysteme Jena GmbH, Germany). The piezo positioner itself can be moved laterally by a coarse manual $x, y$-translation stage (not shown) (461-XY-M, Newport GmbH, Germany).
**P**erformance: The 3D piezo-stage has a minimal step size of about 1.2 nm and 80 $\mu$m maximal travel in closed loop mode. The manual translation stage has about 1 cm lateral travel with a precision of about 2 $\mu$m. This combination allows manual coarse positioning of the sample in the millimeter range and computer controlled fine positioning in the nanometer range. To test the mechanical stability of this positioning system the optical trap was held in a fix position on top of a sphere that was immobilised on the coverslip surface. In this set-up the position

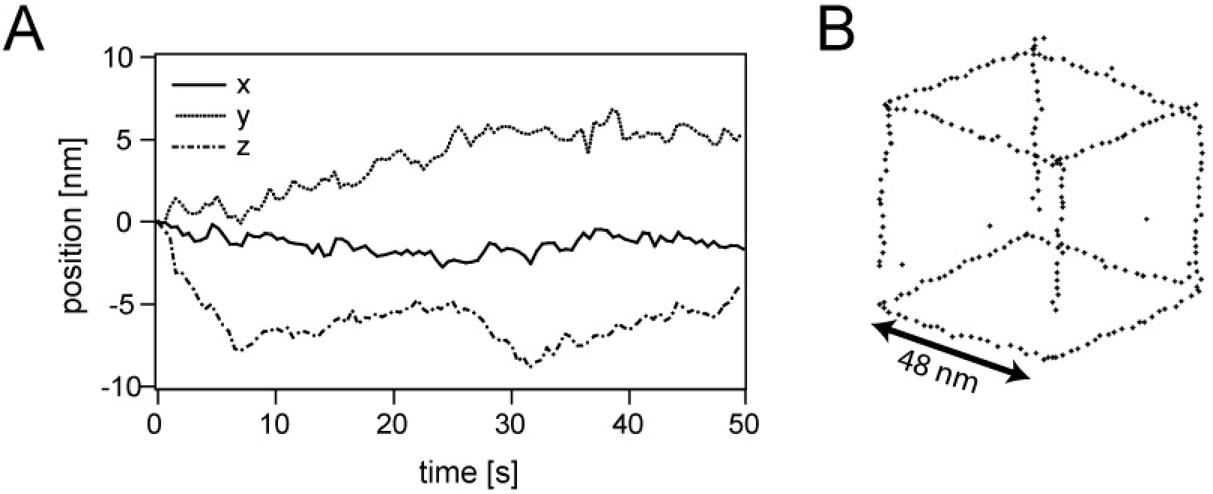

**Figure 2.6:** Mechanical stability and resolution of the positioning system. A) Long term drift. A 0.53 $\mu$m (diam.) latex sphere was attached to a coverslip and centered in the optical trap. The 3D sphere position was recorded for 50 seconds. During this time neither optical trap nor sphere were actively moved. B) Three-dimensional particle tracking. A 0.53 $\mu$m (diam.) latex sphere was attached to a coverslip and centered in the optical trap. The 3D piezo-positioners moved the sphere along a path that constitutes a cube through the focus. The detection system recorded the center positions of the sphere, which are represented by black dots. The step size was 2.4 nm. The total data acquisition time was 10 s.

detector reports drifts of the relative positions of coverslip and optical trap. This is relevant because the sample is typically connected to the coverslip while the probe resides in the optical trap. At room temperature drifts were typically around 2 nm per 10 s and about to 10 nm per 10 s axially (see Fig. 2.6A). To test the three-dimensional resolution of the positioning system, the adsorbed sphere was moved by the piezopositioner in a cubic pattern. Individual steps of 2.4 nm can be clearly resolved in all three dimensions Fig. 2.6B. Consistent with the above stability measurement, an axial drift of the coverlslip of about 5 nm during the 10 s measurement time causes the lower side of the cube to be slightly displaced.

### Brightfield and fluorescence microscopy

Implementation: For brightfield illumination the detection lens (DL) serves as a condenser to shine the light of a white light lamp (Lamp) onto the sample. The light transmitting the sample is collected by the objective lens (OL), reflected by a mirror (M) and projected by 180 mm tube lens (TL) at a camera (CCD) (C5405, Hamamatsu Photonics, Japan). For fluorescence excitation the 488 nm line of an Argon-Ion laser (2014-25ML, JDS Uniphase, Germany) was coupled into an optical fiber (OF)[10] (PMC-540-5, 4-NA008-3-APC-300-V, Schäfter and

---

[10] Argon-Ion laser need a ventilation system for cooling that causes mechanical vibrations which would hamper the mechanical stability of the microscope. Thus, the laser-light was coupled into the set-up via an

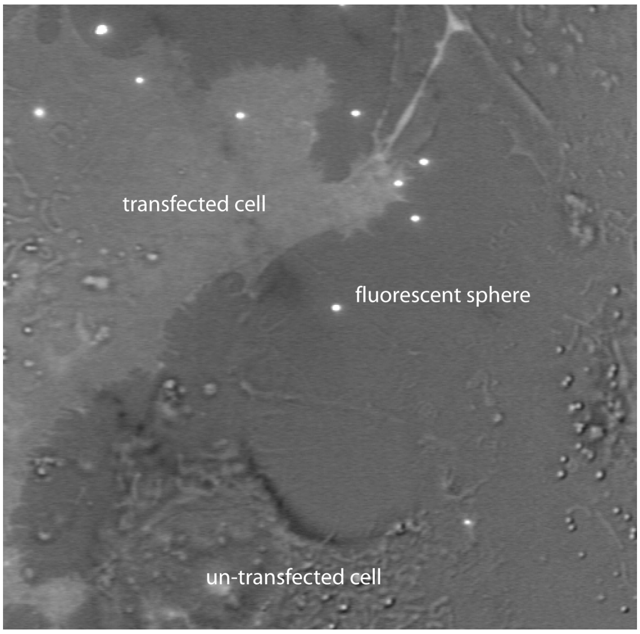

**Figure 2.7:** Simultaneous brightfield and fluorescence microscopy. Cos7 cells express GFP-EGFR. Bright dots are fluorescent 250 nm spheres.

Kirchhoff, Germany) and selected by a band pass filter (F1) (Laser clean-up filter D488/20, AHF analysentechnik, Germany). A 200 mm lens (L3) focuses the laser onto the back focal plane of the objective lens, providing widefield illumination over the whole field of view. A long pass dicroic beamsplitter (BS3) (Beamsplitter Q495LP, AHF analysentechnik, Germany) reflects the excitation light and transmits the emitted green fluorescence. A band pass filter (F2) (Emitter HQ 525/50, AHF Analysentechnik, Germany) further cleans the green fluorescence from scattered 488 nm excitation light and from scattered 1064 nm trapping laser light. **P**erformance: The sample and the probe particle can be visualised by simultaneous brightfield and fluorescence microscopy. Fluorescence is used to identify fluorescent latex spheres, which were used as probe particles, and to identify cells expressing fluorescent membrane proteins. Brightfield illumination was necessary to exclude the presence of scattering objects that could interfere with the probe position detector. Fig. 2.7 shows that cells and spheres can be readily visualised simultaneously.

### Software control

**I**mplementation: Software to control the microscope was initially developed by the diploma student Dirk Neumayer (Neumayer, 2003). It was partly adapted to suit the experiments in this work. **P**erformance: The software permits the on-line visualisation of the probe position

---

optical fiber to spatially separate the laser and its ventilation from the microscope.

fluctuations as measured by the QPD. Simultaneously the CCD image is shown and the position of the sample can be controlled in 3D by the piezo-positioner. 3D position time traces of the Brownian motion of the probe can be acquired with acquisition rates up to 1 MHz for up to 10 s. For longer acquisition times, data has to be acquired and saved in blocks. At the current implementation this however yields gaps of around 1 s between successive blocks because the PC is busy to transfer data from memory to hard disk.

### 2.3.3 Summary

A set-up was developed to perform Thermal Noise Imaging Microscopy. Brownian motion of latex microspheres, which serve as probes in TNIM, are confined by optical tweezers that are formed by a tightly focused 1064 nm laser beam. Laser powers of less than 5 mW were sufficient to confine Brownian motion of probe spheres between 200 nm and 600 nm in diameter to an ellipsoidal volume of about ±300 nm extend in $z$ and ±150 nm in $x, y$. Both the low absorbance of water at 1064 nm and the low laser powers needed are advantageous in terms of minimal laser induced damage of biological samples. Brownian motion of probe spheres could be tracked at 1 MHz continuously over many seconds in 3D by an interferometric position detection scheme that relies on laser light scattered by the probe sphere. Spatial accuracy (given as ±one standard-deviation) was approximately ±1 nm laterally and ±5 nm axially for 250 nm latex spheres and ±0.1 nm laterally and ±0.5 nm axially for 560 nm latex spheres (a major factor that currently limits the accuracy is high-frequency laser intensity noise). The microscope frame, which integrates individual optical and mechanical components, was build by the mechanical workshop at EMBL according to the author's specifications. It was designed to yield an overall stability that permits measurement on the nanometer scale on biological samples. In fact, mechanical drift of components was $\leq$1 nm/s in all directions at $\approx$22°C. In conclusion, spatial accuracy in probe position detection and mechanical stability of the set-up permit imaging of plasma membrane lateral heterogeneities with nanometer resolution. Experiments are performed semi-automatic, i.e. mainly software controlled, however some actions, e.g. coarse sample positioning, are performed manually. On the micrometer scale, experiments are controlled by simultaneous brightfield and fluorescence microscopy of the sample. Furthermore, the software immediately visualises the probe's Brownian position fluctuations thereby permitting on-line control of the experiment on the nanometer scale.

## 2.4 Determination and correction of position detection nonlinearity

In Thermal Noise Imaging Microscopy it is key that the 3D Brownian motion of the probe particle in the optical trap is followed precisely. The position detection scheme in TNIM exploits scattering of the strongly focussed trapping laser on the probe particle as described in Pralle et al. (1999). In brief, scattered and unscattered laser light generate an interference pattern that depends on the position of the particle in the optical trap. Changes in this interference pattern are monitored by a quadrant photo diode (QPD). Within a certain range, QPD signals depend nearly linearly on particle position (e.g. $x$) and thus calibration of signals (e.g. $SX$) can be approximated by multiplication with one calibration factor (e.g. $x = \beta_x SX$). Gittes and Schmidt (1997) described a method to obtain calibration factors for each direction of motion by comparing measured signal fluctuations to the thermal position fluctuations that would be expected for the given temperature of the medium. However, this approach neglects nonlinearities in the detector response (see Fig. 2.4B). Thus, using this calibration scheme for TNIM would yield mediocre results, e.g. images of objects would appear deformed.
For this reason, a novel method for determination and correction of position detection nonlinearity was developed. In the following sections, the theoretical principle and experimental realisation of the method are described. The method was routinely used for calibration of position signals throughout this work.

### 2.4.1 Theory

For simplicity, the formalism is discussed for the $x$-axis only. Experimental results in section 2.4.2 are given for all axes.
The variance of the thermal position fluctuations of a microsphere at position $\vec{r}$ is proportional to its local diffusive mobility $D_x(\vec{r})$ (see section 3.2.1)[11]:

$$\operatorname{var}(\Delta x)|_{\vec{r}} := \left\langle \Delta x^2 \right\rangle_{\vec{r}} - \left\langle \Delta x \right\rangle_{\vec{r}}^2 = 2D_x(\vec{r})\Delta t \tag{2.12}$$

---

[11] In the original publication (Tischer et al., 2004) the mean square displacement (MSD) $\left\langle \Delta x^2 \right\rangle$ is used instead of the variance. The MSD however includes systematic displacements caused by the optical trap, i.e. the sphere is accelerated toward the trap center. As argued in Tischer et al. (2004), this systematic contribution can be neglected if $\Delta t$ is chosen sufficiently small, because the thermal force dominates over the optical force at short time scales. However, the variance, where the squared drift $\left\langle \Delta x \right\rangle^2$ is subtracted, directly gives the diffusion constant (see section 3.2.1). Thus, although the argumentation in Tischer et al. (2004) is valid, taking the variance instead of the MSD improves the method's robustness.

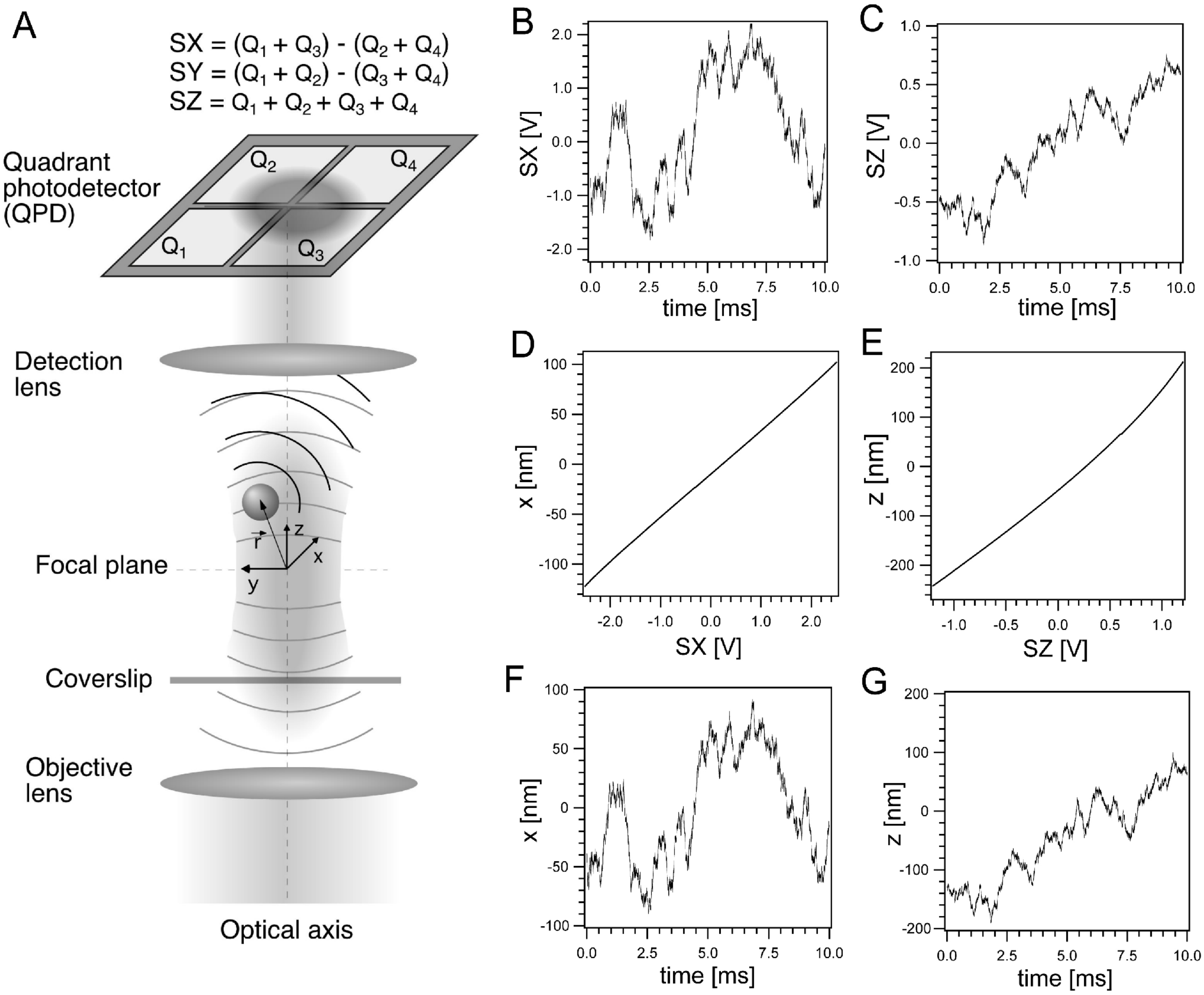

**Figure 2.8:** Three-dimensional position detection in Thermal Noise Imaging Microscopy. A) Schematics. Both forward scattered laser light from the trapped microsphere and unscattered laser light are projected onto the quadrant photodiode (QPD). The resulting interference pattern on the QPD is sensitive to the thermal position fluctuations the trapped sphere. Lateral changes in the interference pattern are dominated by the lateral position $(x, y)$ of the sphere, whereas the total intensity corresponds to the sphere's axial $(z)$ position. B),C) Measured QPD signals of the Brownian motion of a trapped microsphere ($SY$ not shown). D),E) Position vs. signal computed by Equation (2.18). The nonlinearity of $z(SZ)$ is most apparent. F),G) Sphere positions of the signals in (B,C) using the corresponding calibration in (D,E). Experimental details and corresponding detector sensitivities are given in Fig. 2.9.

In bulk solution, i.e. far away from any surfaces, the diffusion coefficient does not depend on the sphere's position $\vec{r}$ and is given by the Stokes-Einstein relation:

$$D_x(\vec{r}) \equiv D = \frac{k_\mathrm{B}T}{6\pi\eta a}, \tag{2.13}$$

where $\eta$ is the viscosity of the medium, $a$ the radius of the sphere, $T$ the temperature of the medium and $k_\mathrm{B}$ the Boltzmann constant. In an experiment all these quantities and consequently also the diffusion coefficient are known. Thus, the variance of the sphere's thermal position fluctuations is also known and can therefore provide a calibration standard. This is exploited by comparing the *expected* variance of thermal position fluctuations to the *measured* variance of the fluctuations of the QPD signal:

$$\mathrm{var}(\Delta SX)|_{SX_0} := \left\langle \Delta SX^2 \right\rangle_{SX_0} - \left\langle \Delta SX \right\rangle^2_{SX_0} \tag{2.14}$$

To obtain the measured signal fluctuations at a specific spot $SX_0$ within the detector response (Fig. 2.8D,E) the variance is evaluated only taking into account signals within a small interval $[SX_0 - \Delta SX, SX_0 + \Delta SX]$. If the signal $SX$ depended perfectly linear on the position $x$, the variance of $\Delta SX$ would be independent of $SX_0$. However, in fact there are non-linearities in the detector response and the variance depends on $SX_0$. Particle movements appear amplified or diminished in the signal time-trace, depending (to the first-order) on the slope of the signal as a function of the position:

$$\Delta SX \approx \partial_x SX|_{SX_0} \Delta x \tag{2.15}$$

where $\partial_x SX|_{SX_0}$ is the slope of the detector response at $SX_0$ (see Fig. 2.8D,E). Combining Equation (2.12), Equation (2.13), Equation (2.14), and Equation (2.15) one obtains:

$$\mathrm{var}(\Delta SX)|_{SX_0} \approx \partial_x SX|^2_{SX_0} \mathrm{var}(\Delta x) = \partial_x SX|^2_{SX_0} 2D\Delta t \tag{2.16}$$

Solving for $\partial_x SX|_{SX_0}$ and using the Stokes-Einstein relation (Equation (2.13)) for the diffusion coefficient finally yields:

$$\partial_x SX|_{SX_0} \approx \frac{\sqrt{\mathrm{var}(\Delta SX)|_{SX_0}}}{2k_\mathrm{B}T\Delta t/(6\pi\eta a)} \tag{2.17}$$

All quantities on the right hand site are either experimentally known or can be determined from the measured signal time trace. Thus the local slope of the detector response ("the local detector sensitivity") can be determined experimentally from the QPD signals of the Brownian motion of the sphere in the optical trap.

The local detector sensitivity $\partial_x SX|_{SX_0}$ is the derivative of the measured signal with respect to the position. The actual positions can be therefore reconstructed by integration:

$$x(SX) \approx \int_{SX_{min}}^{SX} \frac{1}{\partial_x SX|_{SX'}} dSX' + \text{offset} \tag{2.18}$$

The offset that depends on the minimal signal $SX_{min}$ for which the detector sensitivity could be determined. This offset just translates the coordinate system. It is usually chosen such that the trap center is at the origin.

### 2.4.2 Realisation and discussion

Detector sensitivities, i.e. local slopes of the signal with respect to the position, were measured for a 536 nm (diameter) polystyrene sphere (see Fig. 2.9A).

Positions far from the centre of the trap are sampled less frequently resulting in increased statistical noise in the determination of detector sensitivities. This statistical error is inversely proportional to the square root of the number of data points. If desired, the accuracy could therefore be increased by longer measurement of the sphere's position fluctuations.

Detector sensitivities along lateral directions ($x$, $y$) are maximal at the trap center ($x = 0$, $y = 0$) and decrease towards the rim of the trap. Along the axial direction ($z$), detector sensitivity decreases continuously from positions close to the geometrical focus (toward $+z$, compare Fig. 2.8A) by more than a factor of two. This behaviour of the detector sensitivities in both lateral and axial directions is in qualitative agreement with theoretical predictions for Rayleigh-scatterers by Pralle et al. (1999) and for arbitrary spheres in arbitrarily focused beams by Rohrbach et al. (2003).

The maximal detector sensitivity is larger along the $x$-axis (≈22 mV/nm) than along the $y$-axis (≈19 mV/nm), although both signals are identically amplified by the electronics. This is an effect of the linear polarization of the laser light, which introduces an asymmetry between $x$ and $y$ (see Rohrbach et al. (2003)).

Calibrated sphere positions can be reconstructed from measured QPD signals $SX(t)$, $SY(t)$ and $SZ(t)$ using Equation (2.18). Position histograms and variances of the sphere's thermal displacements were calculated (see Fig. 2.9B). As expected, variances of displacements are independent of the sphere's position in the optical trap, demonstrating proper signal calibration. All calibrated position histograms have Gaussian profiles, indicating that it is appropriate to approximate an optical trap as a 3D harmonic potential. Interestingly, although the shape of the uncalibrated axial signal histogram (Fig. 2.9A, lower panel) is asymmetric, the calibrated positions have a symmetric Gaussian distribution. The distortion of the histogram of the uncalibrated $SZ$ signals is caused by the strong increase in detection sensitivity towards the

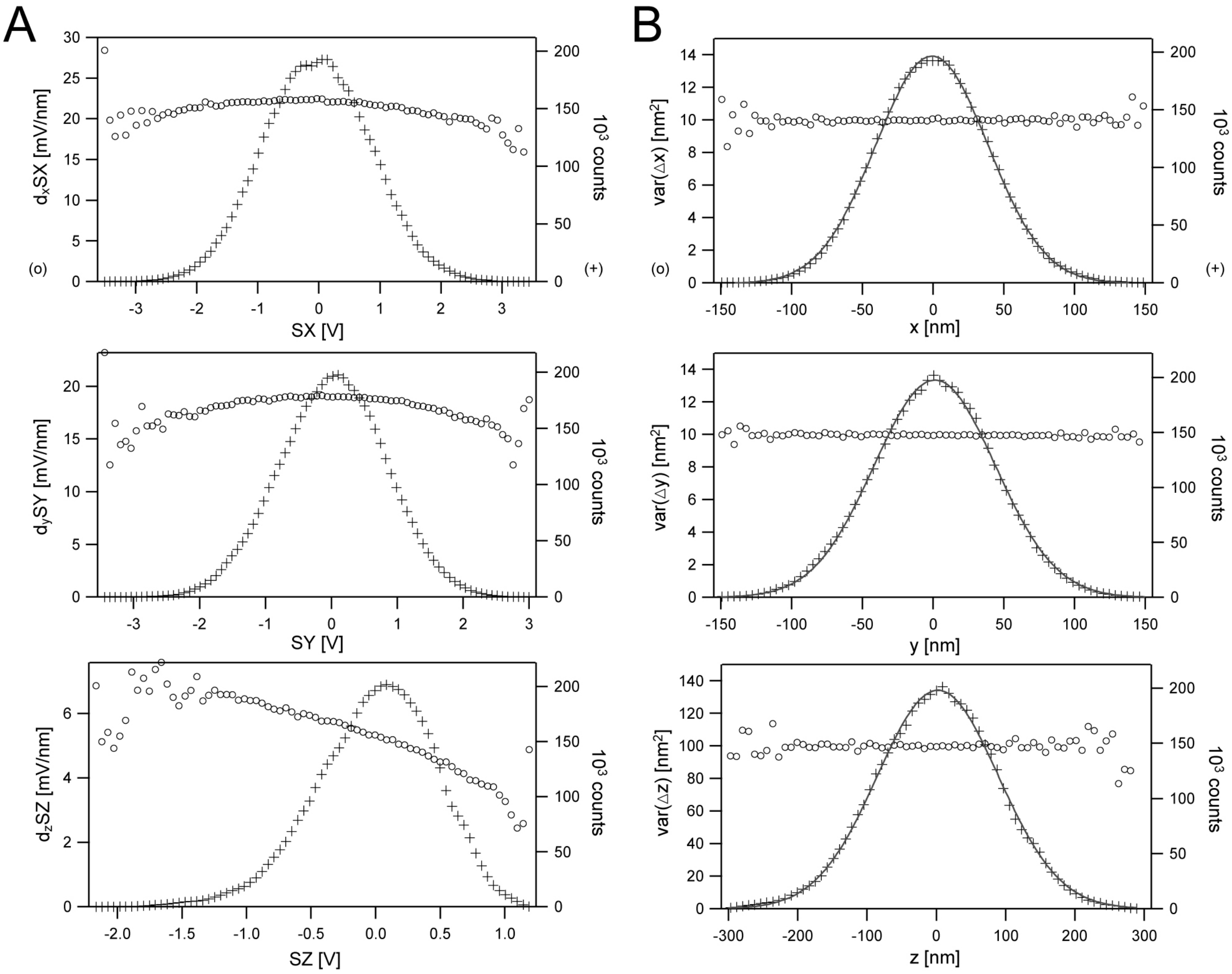

**Figure 2.9:** Determination and correction of position detector nonlinearities. A) Detector sensitivities (circles) and signal histograms (crosses) computed according to Equation (2.17) from QPD signals that resulted from the Brownian motion of a microsphere in the optical trap. B) Variances of the sphere's displacements (circles) and position frequency histograms (crosses) computed from the calibrated position traces. Gaussian profiles (solid lines) were fitted to position histograms. Experimental details: a polystyrene sphere (radius $a$=267 nm) was trapped in water at $T \approx 298$ K ($\eta_{water} \approx 0.89 \cdot 10^{-3}$ Ns/m$^2$); signals were acquired for 5 s at 1 MHz; detector sensitivities and variances of the displacements were calculated at $\Delta t = 5$ $\mu$s for motion along $x$ and $y$ and at $\Delta t = 50$ $\mu$s for motion along $z$ (compare to Fig. 2.8).

trap center (see again Fig. 2.9A, lower panel). Consequently, a calibration of the QPD's $SZ$ signal that ignores detector nonlinearities would result in an asymmetric position histogram. This demonstrates that it is important to take detector nonlinearities into account in order to accurately determine the trapping forces as well as to avoid distortions in images obtained with Thermal Noise Imaging Microscopy.

### 2.4.3 Summary

A method was developed to calibrate the detection scheme that is used for tracking the probe position in TNIM (see section 2.3.2). The method employs the diffusion constant of the trapped particle as a local calibration standard. Using this method, local detector sensitivities can be measured. Moreover, the full detector response can be calculated from the measured sensitivities. Thus, calibration of position time traces becomes possible even for detector signals that depend on the particle's position in a non-linear way. Importantly, the method works *in situ*, i.e. it does not require additional reference measurements but can be applied directly in the sample. This is particularly useful for applications where calibration measurements on fixed particles are not possible due to complex environments (e.g. in the interior of a polymer network, section 3.1). In particular, the calibration scheme developed was key for imaging of diffusive mobilities close to surfaces (section 3.2) and within the plasma membrane (section 4.4.3). By a simple calibration of the detector using one calibration factor for each axis (Gittes and Schmidt, 1997) particle mobilities would have appeared amplified or diminished by the nonlinear detector response.

# 3. 3D-TNIM:
# Imaging constrained diffusion in 3D

## Chapter outline

The main objective of this work was to use TNIM for investigation on constraints to diffusion of the transmembrane protein EGFR. However, TNIM does not only permit investigation of mobility and structure in membranes (2D-TNIM), but also within complex 3D samples (3D-TNIM). In contrast to 2D-TNIM, the marker sphere is not coupled to a membrane protein, but diffuses in 3D.

The 3D-TNIM measurements presented in this chapter validate the concept of the microscope and contain novel information on the diffusive mobility of microscopic particles in the presence of constraints. In section 3.1, it is ascertained that the interaction of the probe with nano-structures can be detected. This is achieved by tracking thermal position fluctuations of a microsphere inside an agar gel. Agar gel consist of interconnected polymer filaments that hinder the diffusion of the sphere and thereby create inaccessible volumes.

In section 3.2, the measurement of diffusive mobilities in presence of objects that constrain the motion is established. The diffusive motion of a microsphere is observed in the vicinity of glass and polymer surfaces. Results are compared to existing theoretical predictions for hydrodynamic coupling of a sphere to a single rigid surface. Moreover, diffusive mobilities of microspheres could be measured in the direct vicinity to the surface of a living cell (section 3.2.5), being important for the interpretation of 2D-TNIM experiments where microspheres are coupled to membrane proteins.

## 3.1 Imaging 3D diffusion in a polymer network

The position of a micro-sphere in an optical trap fluctuates due to the thermal energy provided by surrounding solution molecules (see section 2.2). The TNIM allows one to measure these fluctuations with nanometer resolution over many seconds. In bulk solution, the position fluctuations are restricted to a volume that is given by the optical trap (see section 2.2). The basic idea of 3D-TNIM is that the presence of an object further restricts the movements of sphere. In this section, the concept of 3D-TNIM is validated by tracking the thermal position fluctuations of a microsphere inside an agar gel. Polymer filaments within the gel are expected impose 3D constraints on the diffusion of the sphere. For instance, a molecular thin polymer filament is expected to cause a steric depletion zone with at least one sphere's diameter (Fig. 3.1A).

### 3.1.1 Experiment and results

A 108 nm (radius) microsphere was captured inside an agar gel[1]. Position fluctuations were recorded at five adjacent positions of the optical trap (Fig. 3.1B). Next, histograms $n(x, y, z)$ of the measured position fluctuations were calculated at 8 nm binning. Fig. 3.1C shows isosurfaces[2] at 5 counts per voxel[3], i.e. everywhere on the shown surface $n(x, y, z) = 5$. The isosurfaces show a clear constraint at their lower end (Fig. 3.1C). This already indicates that nano-structures can be indeed visualised with TNIM.

To probe a larger volume, position fluctuations were recorded at over 100 adjacent trap positions (Fig. 3.2A). Individual recordings were combined into a single histogram by correcting for their relative displacement. Data at the borders were discarded to avoid statistical noise in less sampled regions (see section 2.2). A reference measurement in bulk solution, i.e. in the absence of an object, showed that the sphere visited each voxel $\geq$15 times. According to Poisson statistics, the chance to obtain $\leq$5 counts in such a voxel by statistical fluctuations is $\ll$1%:

$$\sum_{n=0}^{n=5} \frac{\exp(-m)m^n}{n!} = 0.00279\ldots \quad \text{for} \quad m = 15 \tag{3.1}$$

An isosurface at 5 counts per voxel is therefore a sensitive indicator for the presence of an object. Consequently, the combined position histogram in Fig. 3.2B was visualised at 5 counts per voxel[4]. The isosurface indicates that two polymer filaments (af1 and af2) crossed the probed volume and a third filament (af3) touched it at the border. Due to probe-sample convolution (Fig. 3.1A) a mechanically stiff filament with radius $r_{fil.}$ should appear as a cylinder with a radius of at least $r_{sphere} + r_{fil.}$. It is known from electron microscope studies that the actual diameter of agar filaments is on the molecular scale (Mrani et al., 1995). At a first

---

[1] For details of the sample preparation see section D

[2] An isosurface is a surfaces within a volume that has the same parameter value. In this case the parameter is the frequency by which the a tiny volume element (voxel) has been visited by the diffusing particle.

[3] A voxel is the 3D equivalent of a pixel (2D) or a bin (1D).

[4] A more detailed analysis of TNIM data is discussed in section 4.2

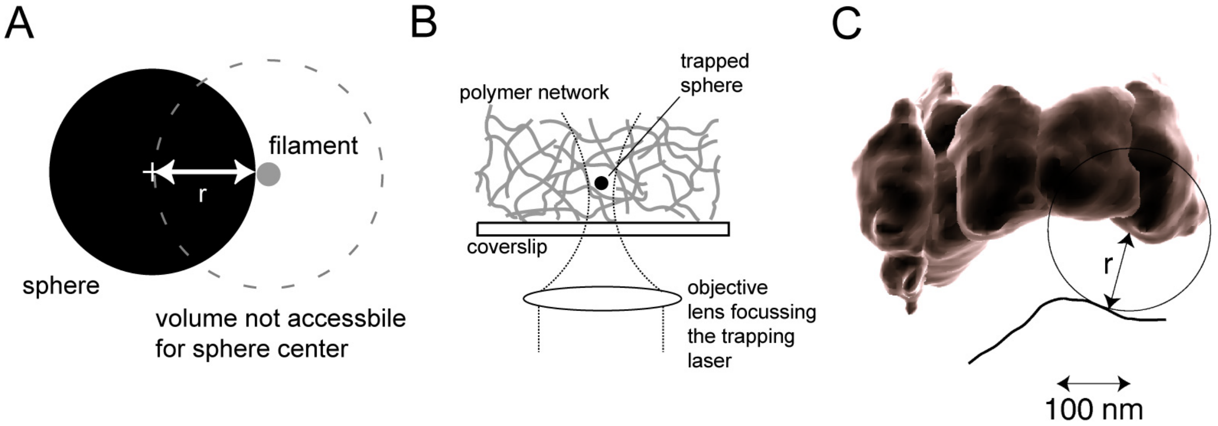

**Figure 3.1:** Principle of Thermal Noise Imaging Microscopy in a 3D polymer network. A) Mechanical amplification effect. In Thermal Noise Imaging Microscopy histograms of the positions of the center of a diffusing sphere are evaluated. Consequently, a stiff filamentous object would appear as a cylinder with a minimal diameter of $d_{min} = d_{object} + 2 \cdot r_{sphere}$. B) Experimental scheme. To image part of an agar network a latex sphere is trapped by optical tweezers and then scanned stepwise through the network. C) Superposition of five isosurfaces of histograms of thermal position fluctuations of a microsphere in an agar network. The optical trap was scanned with a step size of 80 nm. At each position the thermal position fluctuations of a 108 nm (radius) latex sphere were recorded for 0.8 s at 100 kHz. The black line indicates the object position.

glance, one would therefore expect channels with the radius of the sphere. However, because the measurements take place in solution at room-temperature one would also expect considerable thermal position fluctuations of the filaments. Such fluctuations lead to a softening of the sphere-object interface and thus allow channel diameters smaller than the diameter of the sphere. This effect was indeed found in all images recorded (not shown).

### 3.1.2 Resolution of 3D-TNIM

Several factors determine the resolution in 3D Thermal Noise Imaging Microscopy. The most important one is the diameter of the sphere. Only cavities with openings larger than the sphere diameter can be explored. — This is fundamentally different from the case in chapter 4, where the sphere is coupled to a membrane molecule. In this case size of the molecule and *not* the size of the sphere limits the spatial resolution — Furthermore, the total number of position measurements determines the meaningful binning of the position histogram and thus resolution of the image. This resolution was estimated to be about 20 nm from the roughness of isosurfaces in Fig. 3.2A. The precision in measuring the position of the probe only plays a minor role, because here about 1 nm laterally and about 5 nm axially were achieved (section 2.3.2). This is superior in comparison to the meaningful bin-width of position histograms. In general, like in conventional scanning probe microscopy, contact area between probe and sample contributes to the resolution. This effect depends on the radius of probe

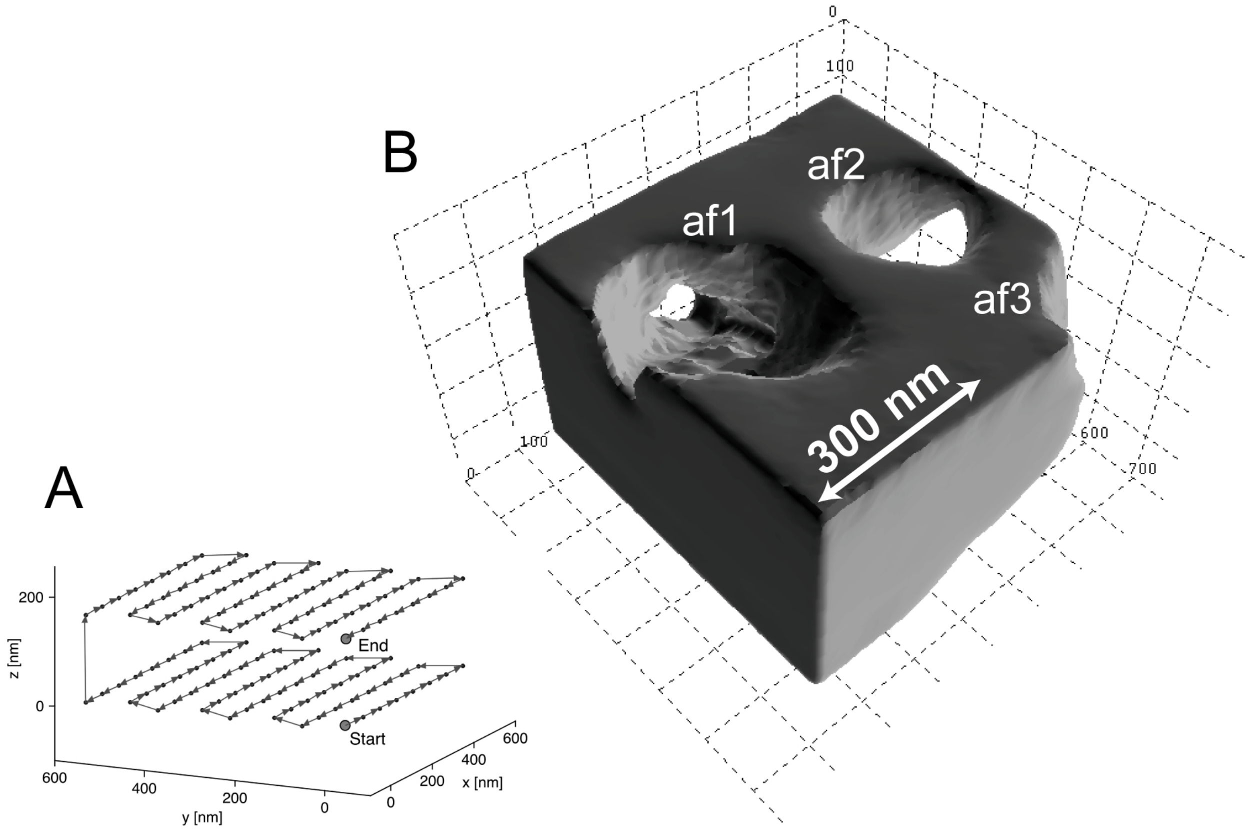

**Figure 3.2:** 3D-TNIM image of a polymer network. A) Scan path. The optical trap was scanned 8x8x2 $(x, y, z)$ steps with a step-width of 80 nm along the x and y axes, and a step width of 160 nm along the z axis. Position fluctuations were recorded for 0.8 s at 100 kHz at each spot. B) The volume accessible to the sphere fluctuations is within the isosurface. Steric depletion zones caused by the presence of agar filaments appear either as channels (af1 and af2) or as an additional constraint on the overall volume (af3).

and the properties of the sample. The speed of thermal noise imaging depends on the viscous drag on the probe particle, which is proportional to the sphere diameter. Therefore, smaller probe particles would increase both imaging speed and resolution in 3D-TNIM.

### 3.1.3 Conclusions

It has been shown that molecular objects can be detected by their interaction with a diffusing probe particle. Thus, the principle idea of TNIM (see section 2.1) is valid, and the microscope set-up developed allows one to actually realise TNIM, on the nanometer scale, in solution, at ≈22°C. In particular, the foundation has been laid to apply TNIM for imaging nano-compartments of the plasma membrane of living cells (chapter 4.3). From a more general point of view (see also Tischer et al., 2001), it was demonstrated that TNIM solves the key problem of thermal motion for the application of optical traps in Scanning Probe Microscopy. In fact, TNIM employs thermal motion as an efficient ”isotropic 3D scanner on the nanometer scale”. TNIM therefore is the first Scanning Probe Microscopy technique that can operate within 3D samples and that scans the sample with almost isotropic resolution in 3D. Moreover, because thermal motion is used for scanning, forces exerted on the sample are as small as possible. In addition to applications in life sciences, it is therefore expected that 3D-TNIM also becomes a general method in various areas of physics such as soft matter physics (see also the discussion in section 3.2.6).

## 3.2 Detecting spatially varying mobility

In this section TNIM measurements of diffusive mobilities in the presence of confining structures are established. First, the principle of imaging diffusive mobilities is introduced (section 3.2.1). Next, mobilities of a microsphere close to a glass surface are measured (section 3.2.2). The results are compared to theoretical predictions for hydrodynamic coupling of a sphere to a plain rigid surface. In section 3.2.3, the resolution and accuracy of the technique are discussed. In section 4.4, TNIM is used to measure diffusive mobility of plasma membrane molecules. This requires coupling of a marker-sphere to the plasma membrane molecule. In order to calculate the mobility of the molecule from the motion of the sphere-molecule complex, the mobility of the sphere at the plasma membrane must be known. This is measured in section 3.2.5. In general, this experiment addresses the fundamental question of hydrodynamic coupling to soft and fluid surfaces such as biological membranes. In section 3.2.4, 3D-mobilities of a microsphere are imaged in an edge, i.e. two perpendicular walls of a microfluidic polymer channel. Diffusion in an edge is a real two-dimensional problem —

like diffusion in the plasma membrane — for which hydrodynamic calculations are already so complex that no analytical formula has been published. However the geometry is yet simple enough to have an intuitive expectation. This experiment is therefore suitable for validating 2D imaging of diffusive mobilities by TNIM.

### 3.2.1 Imaging diffusive mobilities with TNIM

The mean square displacement (MSD) of a free Brownian particle along an arbitrary axis, say $x$, is given by $\langle \Delta x^2 \rangle = 2D\Delta t$ (Einstein (1905)). $D$ is the diffusion constant and $\Delta x = x(t+\Delta t) - x(t)$ the displacement at lag time $\Delta t$. The brackets denote averaging over $t$. Due to the microsecond temporal and nanometer spatial resolution of the TNIM position detector it is possible to choose $\Delta t$ such that the corresponding displacements are only few nanometers (see section 3.2.3). Spatial changes in diffusive mobilities can thus be imaged with nanometer resolution by computing the variance of local position fluctuations:

$$D_x(\vec{r}) = \frac{\mathrm{var}(\Delta x)|_{\vec{r}}}{2\Delta t} = \frac{\langle \Delta x^2 \rangle_{\vec{r}}}{2\Delta t} - \frac{\langle \Delta x \rangle_{\vec{r}}^2}{2\Delta t} \tag{3.2}$$

Importantly, the averaging $\langle . \rangle_{\vec{r}}$ takes into account only those parts of the measured position time-trace that are within a given bin (one dimension), pixel (two dimensions), or voxel (three dimensions) with center coordinates $\vec{r}$ (see Fig. 3.3). Thus, for instance, $D_x(\vec{r})$ is the local diffusion coefficient at position $\vec{r}$ for motion along the $x$-axis. The second term in Equation (3.2) vanishes for free Brownian motion, because thermally induced displacements have no preferred direction. However, systematic (non-thermal) forces, e.g. those generated by the optical trap or by surface repulsion, result in additional displacements with a non-zero average (additional information is found in Tischer et al. (2004)). In fact, the second term in Equation (3.2) can reveal sub-piconewton forces with nanometer resolution (not shown). Here, the interest lies in the diffusive mobility only, and systematic displacements are therefore substracted.

### 3.2.2 Motion at a glass surface

If the distance of an immersed particle to a surface is on the length scale of its size, it feels an increased viscous drag $\gamma$ due to hydrodynamic coupling. A corresponding decrease in the diffusion coefficient $D$ is expected according to $D = k_B T/\gamma$ (Einstein, 1905), where $T$ is the temperature of the medium. There exist theoretical predictions for the viscous drag on an immersed sphere moving parallel ($\gamma_{||}$) or perpendicular ($\gamma_{\perp}$) to a rigid surface (summarised by Happel and Brenner (1965)). Using Einstein's relation to convert the approximate formulas

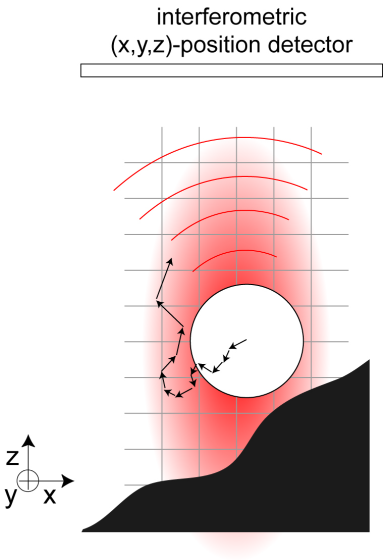

**Figure 3.3:** Imaging diffusive mobilities on the nanometer scale (2D depiction). The Brownian motion (arrows) of a microsphere (typically 0.1-1 $\mu$m in diameter) is confined by the focussed trapping laser (red gradient). The motion within the optical trap is monitored with nanometer spatial and microsecond temporal resolution by detecting the scattered laser light. The average mean square displacement within one pixel (grey grid) gives the local diffusive mobility. Typically, the mobility is reduced in the vicinity of obstacles (black).

of Happel and Brenner (1965) for $\gamma_{||}(z)$ and of Bevan and Prieve (2000) for $\gamma_{\perp}(z)$ yields:

$$\frac{D_{||}(z)}{D_0} \approx 1-\frac{9}{16}g(z)^{-1}+\frac{1}{8}g(z)^{-3}-\frac{45}{256}g(z)^{-4}-\frac{1}{16}g(z)^{-5},\ g(z)=1+\frac{z-z_0}{a} \tag{3.3}$$

$$\frac{D_{\perp}(z)}{D_0} \approx \frac{6(z-z_0)^2+2a(z-z_0)}{6(z-z_0)^2+9a(z-z_0)+2a^2}, \tag{3.4}$$

where $(z+a)-z_0$ is the distance of the sphere center to the surface at $z_0$ and $a$ is the sphere radius. The Stokes-Einstein-relation $D_0 = k_BT/(6\pi\eta a)$ gives the Diffusion constant in bulk solution with viscosity $\eta$. Diffusive mobilities of a 560 nm sphere (CP01F, streptavidin coated, diameter 560±90 nm, Bangs Laboratories, USA) were measured[5] as a function of its distance to a glass surface. Within the optical trap, changes in diffusive mobilities are measured on the nanometer scale. In order to also cover the micrometer scale, the optical trap was positioned at different distances to the glass surface (schematically depicted in Fig. 3.4A). At each position of the trap, local diffusion coefficients for motion parallel ($D_{||}$) and perpendicular ($D_{\perp}$) to the

---

[5] All experiments were performed at ≈22°C in standard phosphate buffer (PBS) containing more than 100 mM NaCl. Consequently the Debye length of electrostatic repulsion is less than 1 nm (Israelachvili, 1991). At lower salt concentrations the motion of the sphere would be significantly influenced on the 100 nm scale by electrostatic repulsion. Thus, both detection of "steric positions" of surfaces and measurement of probe mobility in close proximity to surfaces is facilitated by high salt concentrations. The tendency of particles to adsorb to surfaces at high salt concentrations was diminished by using protein-coated spheres and by adding 0.2 percent bovine serum albumine (BSA) to the medium.

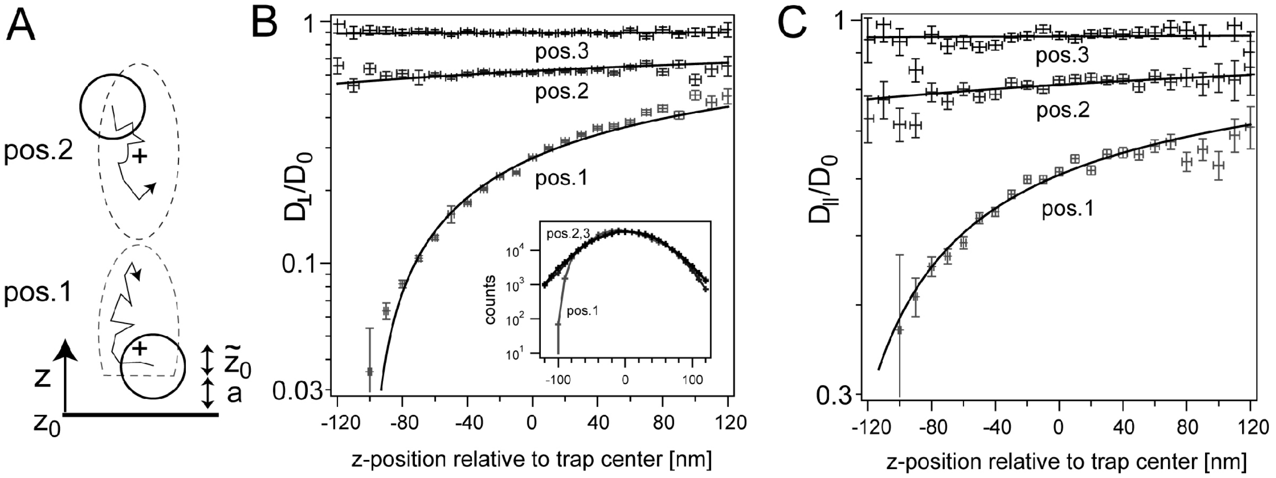

**Figure 3.4:** Diffusive mobilities parallel and perpendicular to a glass surface. A) Scheme of the experiment. The optical trap confines (indicated by dashed lines) the Brownian motion (arrows) of a 560 nm microsphere (circle). At pos.1 the glass surface additionally confines the Brownian motion. The trap was held at pos.1 and subsequently moved by the piezo stage 0.35 $\mu$m to pos.2 and then a further 2 $\mu$m to pos.3 (not shown). The crosses indicate the respective trap centers. At each position of the trap the Brownian motion of the sphere was measured 4 s at 100 kHz. B),C) Normalised diffusion coefficients for motion parallel $D_{||}$ and perpendicular $D_\perp$ to the surface as determined from the local Brownian motion according to Equation (3.2). Solid lines are fits of hydrodynamic theory (Equation (3.3),Equation (3.4)). Fit coefficients are given in the text. Vertical error bars indicate statistical accuracy. Horizontal error bars indicate spatial resolution. The inset in (B) shows position histograms (log-scale) perpendicular to the surface.

surface were computed according to Equation (3.2) at lag time $\Delta t$=20 $\mu$s. Mobility profiles within the trap, are given at each trap position are given with respect to the "trap center". The trap center is defined as the position where the sphere would rest in the *absence* of thermal forces. According to Boltzmann statistics this is equal to the position within the optical trap where the sphere is found most often in the *presence* of thermal forces (see section 2.2). For symmetry reasons changes in the mobility are only expected perpendicular to the surface. Consequently the measured 3D data were projected onto the $z$-axis.. At the glass surface the sphere's diffusive mobility is about $D_\perp \approx 0.035 \cdot D_0$ and $D_{||} \approx 0.35 \cdot D_0$, i.e. motion perpendicular to the surface decreases ten-fold more than motion parallel (compare Fig. 3.4B and Fig. 3.4C). Taking the positions of the optical trap into account, $D_{||}(z)$ and $D_\perp(z)$ were fitted to Equation (3.3) and Equation (3.4), respectively. The fits shown in Fig. 3.4B,C indicate that measurement and theory are consistent for motion parallel and perpendicular to the surface, on the nanometer as well as micrometer scale. Best "least-squares" fits — using the "FuncFit" routine of Igor Pro 4.07 (Wavemetrics, Oregon, USA) — were obtained for ($a_{||} = 245 \pm 15$ nm, $z_{0,||} = 1021 \pm 13$ nm) and for ($a_\perp = 247 \pm 8$ nm, $z_{0,\perp} = 1009 \pm 8$ nm). The fit parameter $z_0$ includes the arbitrary offset of the piezo translation stage coordinates and was therefore converted to $\tilde{z}_{0,||} = 101 \pm 13$ nm and $\tilde{z}_{0,\perp} = 113 \pm 8$ nm, which is the separation of the glass surface and the trap center at pos.1 minus the sphere radius (see Fig. 3.4A). This is a meaningful quantity because it can be compared to the position histograms in Fig. 3.4B,inset. The histogram at pos.1 indicates the position of the coverslip surface which causes an abrupt decrease in the position counts $\tilde{z}_0$=90–100 nm due to steric hindrance. This agrees to within about $\leq$20 nm with surface position $\tilde{z}_{0,||}$ and $\tilde{z}_{0,\perp}$ as found by fitting the hydrodynamic theory.

### 3.2.3 Spatial resolution and accuracy

Physically, the spatial resolution of imaging diffusive mobilities is limited by the particle displacement during the lag time $\Delta t$ at which $D(\vec{r})$ is calculated according to Equation (3.2). For instance, $D(z)$ includes particle positions within $z \pm \delta z$ with $\delta z \approx \sqrt{\langle \Delta z(\Delta t)^2 \rangle}$. Horizontal error bars in Fig. 3.4 show $\delta z$ at $\Delta t$=20 $\mu$s. Average particle displacements $\delta z$ decrease toward the glass surface due to increased viscous drag. In general, any measure that reduces the particle displacement improves the spatial resolution. For instance, using a solution with high viscosity and/or low temperature, decreasing $\delta t$, or increasing particle size will yield reduced particle displacements and thereby increase the spatial resolution of the measurement. Which of these measures is reasonable depends of course on the specific application. For instance, low temperature measurements are not possible when working with living biological samples.
Technically, the spatial resolution is limited by the precision of particle position measurements. As the detection scheme relies on the laser light that is scattered by the trapped sphere, precision is generally better for larger spheres, because more light is scattered leading to an increased signal to noise ratio (section 2.3.2). In this section 560 nm spheres (CP01F, streptavidin coated, diameter 560±90 nm, Bangs Laboratories, USA) were used, for which the precision is about ±0.5 nm along $z$ and about ±0.1 nm along $x$ and $y$. In section 3.2.5 250 nm spheres (L-6905, streptavidin coated, diameter 250±10 nm, SIGMA, USA) were used, for which the precision is ±5 nm along $z$ and ±1 nm along $x$ and $y$.
The vertical error bars in Fig. 3.4B and Fig. 3.4C give the statistical accuracy. The statistical error is small at high counts in the position histogram (see inset in Fig. 3.4B) because the average mean square displacement is determined more accurately. At the glass-surface and far away from the trap center, the number of counts and consequently the accuracy is diminished. Generally, statistical accuracy increases with data acquisition time $t$ and spatial bin-width $\xi$. Increasing bin-width is naturally accompanied by a decrease in spatial resolution. The usefulness of increasing the recording time is mainly limited by the mechanical stability of the microscope and/or the investigated structure. At the moment, the microscope features about 1 nm/s drift at room temperature (section 2.3).

### 3.2.4 Motion in a polymer edge

The Brownian motion of a 560 nm microsphere was imaged inside the right angle of a microfluidic polydimethylsiloxane (PDMS) channel (Fig. 3.5). According to the experimental symmetry, data is shown as a projection into the $(x, z)$-plane. Position histograms in bulk solution show the typical ellipsoidal shape that is governed by the optical trap (Fig. 3.5A, compare to section 2.2). In the edge of the microfluidic channel, polymer surfaces are seen as clear constraints in the 2D position histogram (Fig. 3.5B).
Diffusive mobilities were measured at $\Delta t$=25 $\mu$s for motion along $x$, $y$ and $z$ as a function of $(x, z)$ at 10 nm spacing (Fig. 3.5C). Close to the intersection of the walls (upper right corner in the image in Fig. 3.5C), the measured diffusion coefficients decreased to $\leq$7% (along $x$ and $z$) and $\leq$27% (along $y$) of the value in bulk solution, $D_0$. The mobilities generally increase if the distance to the surfaces increases. To the author's knowledge, there is no analytical formula that describes hydrodynamic coupling in such a geometry. However, Equation (3.3) and Equation (3.4) suggest that diffusive mobilities decrease generally most significantly for motion perpendicular to a surface (see also Fig. 3.4 and Fig. 3.6). This explains why mobility is largest along the $y$-axis, because this is the only direction of motion that has no perpendicular component to any surface. Further, it explains the asymmetry in $x$- and $z$-mobility close to the $(y, z)$ and $(x, y)$ surfaces of the polymer, because mobilities generally decrease more toward the respective perpendicular surface.

### 3.2.5 Motion at a cell surface

The mobility of a 250 nm sphere[6] was measured at the plasma membrane of a living Cos-7 cells, which were also used in chapter 4. Fig. 3.6A shows that the position counts decay less steeply at the cell surface than at the glass surface. This effect was found in all measurements performed ($N > 20$)[7]. Fig. 3.6B shows mobility measurements performed with one microsphere at six different lateral positions. This was done to give indications wether the results depend significantly on the respective position at the putatively heterogeneous cell surface. Individual measurements were aligned by setting the $z$-origin as the position, where surface-repulsion decreased the position counts to half their value in bulk solution (compare with Fig. 3.6A). Mobilities at $\Delta t$=20 $\mu$s were calculated according to Equation (3.2). Individual measurements show similar behavior, indicating that there are no large lateral variations in surface properties of the Cos7 cell membrane. At distances $z$>100 nm, mobilities are similar to those found at the rigid glass surface. In very close proximity to the surface the maximal decrease of the

---

[6] L-6905, streptavidin coated, diameter 250±10 nm, SIGMA, USA

[7] This was consistently found for PtK2 cells, too (not shown).

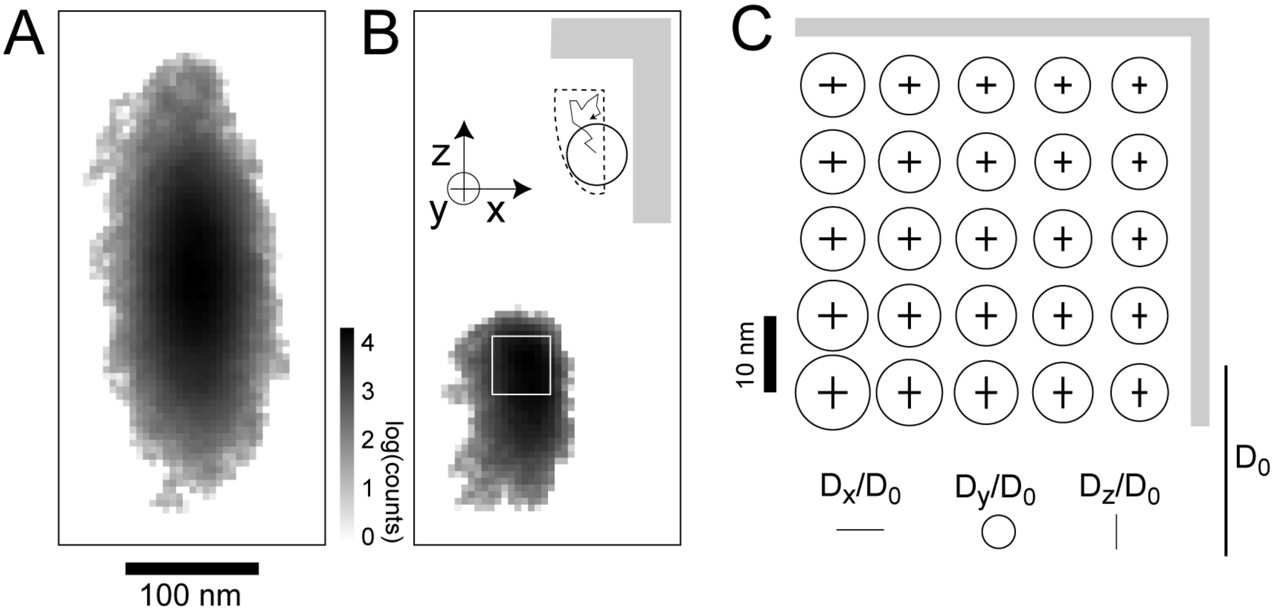

**Figure 3.5:** Diffusive mobilities at two perpendicular polymer walls. A) Position histograms of Brownian motion of a microsphere confined in an optical trap. B) Two perpendicular polymer surfaces further constrain the Brownian motion. Inset schematically shows Brownian motion of microsphere confined (dashed line) by both optical trap and polymer (gray area). C) Diffusive mobilities as computed within the region enclosed by white square in B. Size (length or diameter) of respective symbols is proportional to relative mobilities along the respective axis. Mobility in bulk solution $D_0$ is given for comparison for motion along $z$. Grey lines indicate orientation of polymer surfaces. All panels are computed from Brownian motion of a 560 nm microsphere recorded for 14 s at 200 kHz at ≈22°C.

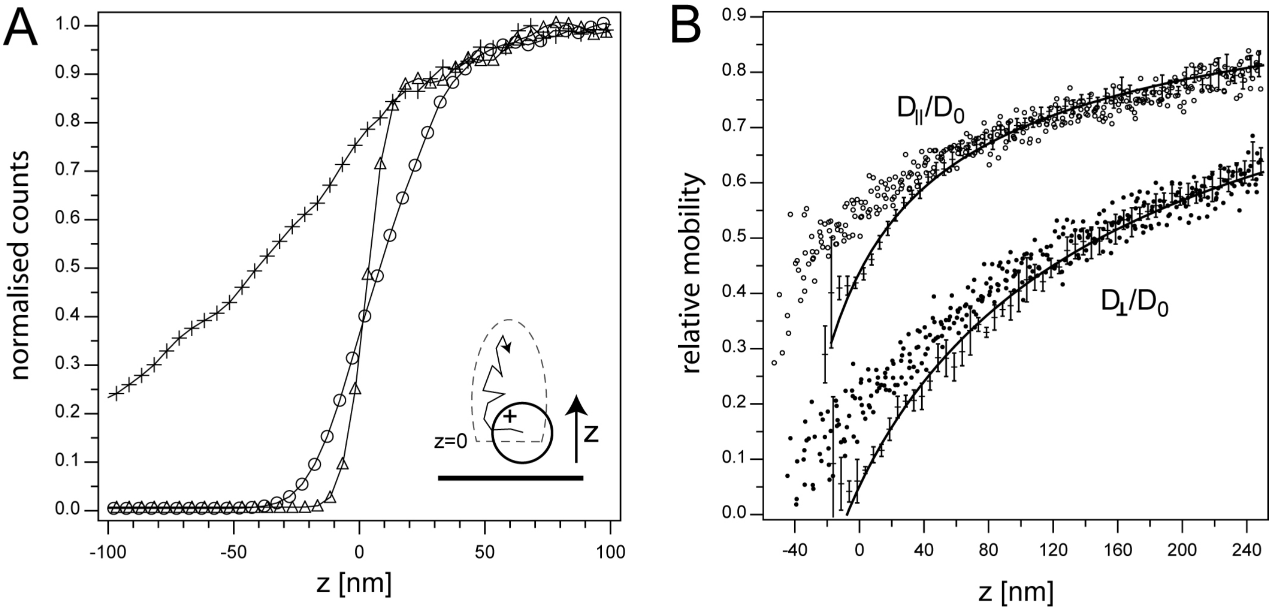

**Figure 3.6:** Diffusive mobilities of a microsphere for motion perpendicular and parallel to a cell surface. A) Normalised histograms of the sphere's thermal position fluctuations perpendicular to a glass surface (triangles) and a Cos-7 cell surface (circles) and in bulk solution (crosses). The histograms were normalised to their respective maximum. In bulk solution the shape of the histogram is dominated by the optical trap. The surfaces additionally constrain the motion of the sphere. The inset schematically shows Brownian motion of a microsphere confined (dashed lines) by both optical trap and surface. B) Relative mobilities for motion parallel ($D_{||}$) and perpendicular ($D_{\perp}$) to surfaces. Measurements at glass surface are shown as average ±one standard-deviation (N=6). Independent least-squares fits of Equation (3.3) and Equation (3.4) to individual measurements yielded $a_{||}$=133±8 nm,$z_{0,||}$=-15±4 nm and $a_{\perp}$=129±3 nm,$z_{0,\perp}$=-5±6 nm, respectively. The fit to the averages is depicted (solid lines). Individual measurements at 6 different cell surface positions are shown as scatter representations (open circles: $D_{||}$; solid circles: $D_{\perp}$). Further details: for each individual measurement positions were monitored 10 s at 100 kHz, spheres were 250 nm in diameter, bin-width 5 nm, temperature of the solution was ≈22°C.

mobilities at the cell and glass surfaces are also comparable, i.e. $D_{\perp}$ less than $0.1 \cdot D_0$ and $D_{||}$ is between $0.3 \cdot D_0$ and $0.4 \cdot D_0$. However, for $z$<100 nm the distance dependence of the mobilities are different at the soft cell surface as compared to the glass surface.

### 3.2.6 Discussion

It was demonstrated that Thermal Noise Imaging Microscopy permits one to measure spatial changes in diffusive mobilities on the nanometer scale (≤10 nm bin-width).

Diffusive mobilities of a 280 nm (radius) sphere were consistent with existing hydrodynamic theories for motion of a sphere parallel and perpendicular to a glass surface, from the nanometer to the micrometer scale. Comparing the data to the hydrodynamic theories yielded two values for the position of the glass surface (for motion parallel and perpendicular). Interestingly, within the same measurement the position of the glass surface could be also determined by the steric hindrance that the glass surface imposes on the sphere's diffusion. These three measurements of the surface position agreed within ±10 nm. Thus, diffusive mobilities are accurately measured at nanometer to micrometer distances to objects, while – simultaneously – the position of the objects can be determined on the nanometer scale.

To test TNIM in a more complex geometry, diffusive mobilities of a 280 nm (radius) sphere were imaged close to the intersection of two walls of a microfluidic polymer channel. Two-dimensional maps of 3D diffusive mobilities could be obtained at 10 nm spatial resolution. The results indicated that even in geometries that are more complex than just one surface diffusion is mainly slowed down for motion *perpendicular* to a surface. Furthermore, the experiment demonstrated that TNIM can measure changes in diffusive mobilities in 3D and on length scales that are relevant in the cellular plasma membrane.

To study diffusion of membrane molecules with TNIM, it is necessary to couple a marker-sphere to the molecule. In order to calculate the mobility of the molecule from the motion of the sphere-molecule complex, the mobility of the sphere near the plasma membrane must be known (section 3.2.5). The diffusive motion of 125 nm (radius) latex spheres was measured close to a Cos7 cell surface and, for comparison, close to a glass surface. Interestingly, the counts in the histogram of the thermal position fluctuations of the sphere decreased less abruptly at the cell surface than at the glass surface, i.e. a 50% decrease of the counts in the position histogram was observed within ca. 10 nm at the glass surface andw within ca. 30 nm at the cell surface. This effect was found in all measurements ($N > 20$) on Cos7 and on PtK2 cells (not shown). This result corresponds well to the fact that cell membranes form soft interfaces that can be thermally excited, i.e. their position is expected to fluctuate (see Brown, 2003; Lin and Brown, 2004). Correspondingly, the dependence of sphere's diffusive mobility on the distance to the surface was different at the cell membrane than at the glass surface. Interestingly, in ultimate proximity to the surface, the maximal decrease of the mobilities was similar at both cell membrane and glass surface.

In conclusion, TNIM permits to measure both the structure of objects and the hydrodynamic effects of these objects on the diffusive mobility of the probe. Importantly, both pieces of information are obtained (i) simultaneously, (ii) at ca. 10 nm resolution in 3D, and (iii) at soft biological interfaces such as cell membranes. These results show the great promise for the general applicability of TNIM for studying diffusive transport in heterogeneous media. This is important in such diverse fields of research as, molecular transport within cells, biotechnological separation methods such as electrophoresis, or the diffusive transport of polymer-based drug carriers through tissue. It is therefore expected that TNIM will become a general tool in areas of research such as soft matter physics and life sciences, and in particular for investigations of lateral nanostructures in the plasma membrane of live cells (see next chapter).

# 4. 2D-TNIM: Imaging constrained diffusion in the plasma membrane

## Chapter outline

In this chapter, TNIM is used to investigate protein mobility in the plane of the plasma membrane (2D-TNIM), requiring the specific coupling of a marker sphere to the membrane protein of interest. The proteins that were investigated and the assay for specifically coupling the marker sphere is described in section 4.1. In section 4.2, it is discussed how observed position time traces can be evaluated in order to obtain information on shape and position of submicrometer-scale lateral plasma membrane structures that constrain the diffusion of the protein. In section 4.3, the membrane environment of EGFR and of a lipid anchored GFP is imaged in intact Cos7 cells. Moreover, it is discussed how TNIM can be used to determine nanometer-scale diffusion coefficients of plasma membrane proteins (section 4.4).

## 4.1 Coupling the marker sphere to the membrane protein

The TNIM is applied to investigate the submicrometer scale mobility of EGFR and a lipid anchored GFP. This requires that these proteins are coupled to a marker particle in order to (i) permit tracking of the molecule's motion, and (ii) confine the diffusion of the molecule to a small membrane area, using the optical trap (see section 2.1). Coupling of marker particles — such as the microspheres employed in this work — to membrane proteins is generally challenging, because of nonspecific binding of the marker particle to the cell surface. The choice and characterisation of the coupling assay is consequently of critical importance for the interpretation of the subsequent experiments. The specificity of the assay that was used in this work was therefore confirmed in an extra set of experiments (section 4.1.3). Furthermore, it is shown that the TNIM allows one to observe the binding of the marker sphere to the membrane proteins with spatial and temporal high resolution (section 4.1.4).

### 4.1.1 Selection of marker spheres and protein constructs

Fluorescent latex-spheres with a radius of 125 nm and a streptavidin protein coat (L-6905, SIGMA, Saint Louis, Missouri, USA) served as marker particles. The reasons for this choice were: first, the fluorescence allows one to distinguish the spheres from small vesicles or other particles that are present when working with living cells (see e.g. Fig. 2.7). Second, the streptavidin protein coat diminishes unspecific binding of spheres to the cell membrane and is used to mediate specific binding to the protein of interest via a biotinylated antibody (see below). And third, the size and material of theses spheres permitted to trap them by the optical tweezers and to detect their position with nanometer precision (see section 2.3.2).

The membrane molecules under investigation were genetically tagged with green fluorescent protein (GFP), i.e. cDNA was used that encoded for the respective construct (see next section). This had the following advantages: first, the molecules could be investigated in a cell line of choice by transfection of cDNA. Second, cells that expressed the protein on the plasma membrane could be identified by conventional fluorescence microscopy. Third, the micrometer-scale mobility of the molecules could be measured by photobleaching the GFP, i.e. using FRAP (see Appendix B). And forth, the strepatividin coated marker spheres could be coupled to both membrane proteins using the same batch of biotinylated[1] monoclonal GFP antibodies (600-306-215, Rockland, Gilbertsville, USA) (see Fig. 4.2A). This was advantageous in order to minimise assay specific differences when comparing the diffusive behaviour of the proteins.

### 4.1.2 Protein constructs and cell line

The membrane protein of foremost interest was EGFR. GFP-EGFR, cDNA encoding for green fluorescent protein (GFP) as the ectodomain connected to EGFR was constructed by a member of the lab, Dr. Martin Offterdinger. To study if membrane lateral heterogeneities depend on membrane anchoring, the mobility of EGFR was compared to GFP connected to a glycosylphosphatidylinositol (GPI) anchor, GFP-GL-GPI, where GL stands for glycosylated[2]. GFP-EGFR is a transmembrane protein with a large (≈2 nm) cytoplasmic portion, whereas GFP-GL-GPI only resides in the outer leaflet of the lipid bilayer. Fig. 4.1A shows the constructs and their integration into a lipid bilayer.

Experiments were performed in the plasma membrane of Cos7 cells (SV40-transformed green African monkey fibroblast). Cos7 cells are adherent to glass coverslips and are therefore well suited for microscopy. Furthermore, Cos7 cells often have plasma membrane areas that are

---

[1] Biotin-(strept)avidin bonds are among the strongest noncovalent linkages in biology (Florin et al., 1994).

[2] The cDNA for this construct was generously donated by Patrick Keller (MPI-CBG in Dresden).

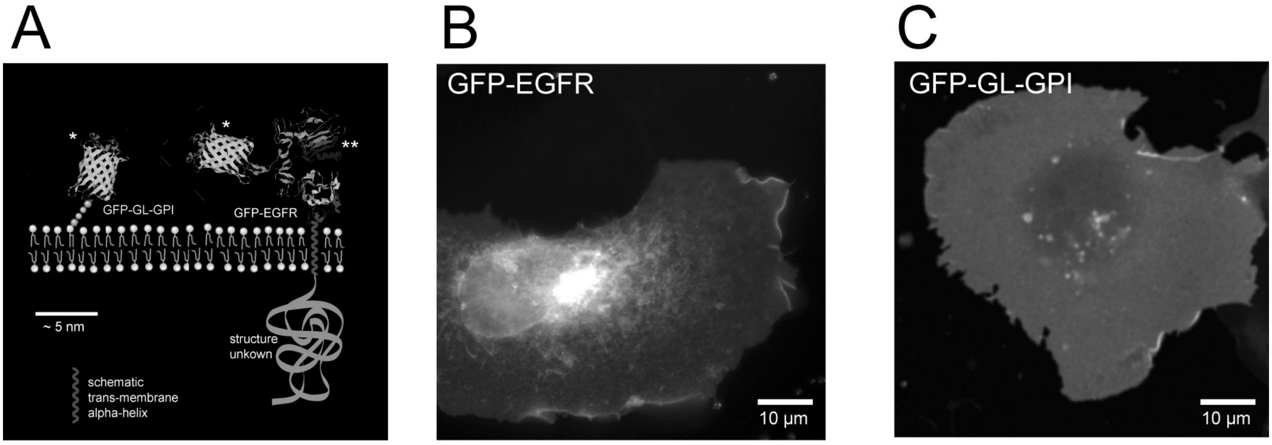

**Figure 4.1:** Membrane protein constructs studied in this work. A) Scaled depiction of the constructs within a lipid bilayer. GFP (*) and the ectodomain of EGFR (**) are ribbon structure representations of the respective published structures as obtained by x-ray crystallography (Ormo et al., 1996; Garrett et al., 2002). B,C) Fluorescence microscopy images of Cos7 cells expressing GFP-EGFR or GFP-GL-GPI. Both GFP-EGFR and GFP-GL-GPI have plasma membrane localisation. Cos7 cells expressing GFP-EGFR often showed an additional bright perinuclear stain (like in this example), most likely corresponding to intracellular membranes.

flat on the micrometer scale and are therefore particularly suitable for quantitative studies of membrane protein mobility.

### 4.1.3 Coupling specificity

To test the specificity of the coupling assay, binding of 250 nm red fluorescent streptavidin spheres[3] to GFP-GL-GPI expressing Cos7 cells was detected by fluorescence microscopy. For quantification, the ratio of red fluorescent pixels (proportional to bound spheres) and green fluorescent pixels (proportional to available binding sites) was calculated. Each image contained part of the plasma membrane of one cell (e.g. Fig. 4.2C) and each experiment in Fig. 4.2B comprises 15 images. Binding of spheres to the cell surface was diminished 6–7 fold if cells were *not* incubated with biotinylated GFP antibody. This indicates that the majority of spheres is coupled to GFP via an antibody link as depicted in Fig. 4.2A. To further validate bond formation as depicted in Fig. 4.2A, spheres were pre-incubated with 100 $\mu$M free biotin for 15 minutes in order to occupy streptavidin binding sites. As expected, spheres that were blocked with biotin showed similar low binding as in the absence of antibody (see Fig. 4.2B).

---

[3] Information about reagents and molecular biological methods is given in Appendix D

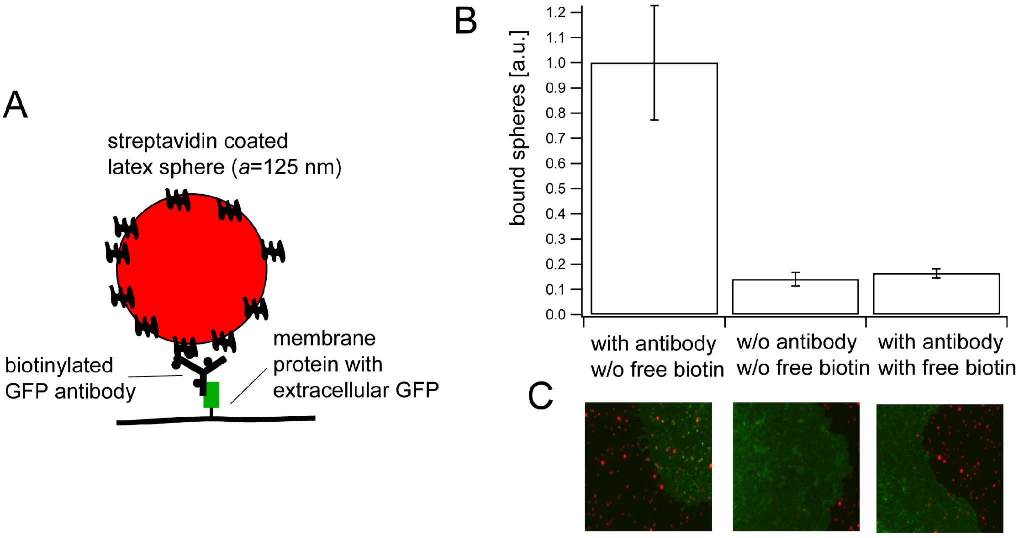

**Figure 4.2:** Coupling assay and specificity. A) Schematic depiction of coupling assay. B) Relative binding of streptavidin coated microspheres to GFP-GL-GPI expressing Cos7 cells as determined from fluorescence microscopy images such as shown in (C) ($N$=15 images were taken for each condition). C) Fluorescence microscopy images. Green color corresponds to GFP-GL-GPI fluorescence, red color corresponds to red-fluorescent strepavidin-coated latex-spheres (radius 125 nm). Spheres on cells can appear yellow (overlay of green and red).

### 4.1.4 TNIM controlled coupling

Here, it is demonstrated how the binding of the marker sphere to the membrane protein can be controlled with the TNIM. This procedure was routinely used in all experiments presented in section 4.3 and section 4.4. First, a marker sphere that is freely diffusing in bulk solution is trapped by the optical tweezers. Subsequently, the trap is moved by piezo-translators towards the surface of a Cos7 cell that expresses the GFP coupled membrane protein (Fig. 4.3A). Simultaneously, thermal position fluctuations of the trapped sphere are monitored on-line (Fig. 4.3B). Surface proximity is observed via the $z$-position fluctuations, which are reduced at the cell surface (Fig. 4.3B). When $z$-position fluctuations were reduced to about 50% of their extend in bulk solution, movement of the optical trap is stopped for the remainder of the experiment. Bond formation is detected as strong confinement of the sphere's $z$-position fluctuations to the vicinity of the plasma membrane (Fig. 4.3B). The step-like reduction in the $z$-position fluctuations can be detected with millisecond precision in the $z$-position time trace (Fig. 4.3C).

The 2D histograms of the sphere's thermal position fluctuations in Fig. 4.3D shows the position distribution in bulk solution, where thermal position fluctuations are confined by the optical trap alone (see also section 2.2). At the cell surface, the position distribution is constrained at the lower end, which is one sphere radius above the actual cell surface, because histograms show positions of the sphere center.

Histograms of the sphere's positions at the cell surface *before* binding contain information on the local flatness of the plasma membrane. In the example shown, the probed membrane area is flat on a scale of tens of nanometers. *After* binding, the $z$-position fluctuations are confined to the plasma membrane. However, the position histogram indicates that (in this example) also the lateral position fluctuations are restricted after binding (positions on the right hand side of the trap center were accessed before binding but are not accessed after binding Fig. 4.3D). This indicates that the motion of the sphere-molecule complex is hindered by structures in the plasma membrane that confine the motion of the molecule. The quantitative imaging of these structures is presented in section 4.3.

### 4.1.5 Discussion and outlook

An assay for coupling streptavidin coated microspheres to GFP-coupled membrane proteins was established in order to make 2D-TNIM experiments on membrane molecules possible. Control experiments indicated that 80–90% of the spheres bind specifically to the protein of interest. Thus, when evaluating 2D-TNIM experiments it must be kept in mind that every $6^{th}$–$7^{th}$ might report on the mobility of plasma membrane components distinct from the respective molecule of interest. Such nonspecific binding is a typical challenge when working with relatively large marker particles. Suzuki et al. (2000) reported for antibody mediated coupling of 730 nm latex spheres to cell surface proteins a specificity of 6:1 (in presence of antibody, binding of spheres was enhanced 6 fold). Murase et al. (2004) reported for antibody mediated coupling of 40 nm gold spheres to cell surface proteins a specificity of 5:1. This shows that a specificity between 6:1 and 7:1, which was obtained here, meets current requirements. The binding of the streptavidin microspheres to the GFP coupled membrane proteins is mediated by biotinylated monoclonal GFP antibodies. Specific binding of the spheres to the cell surface proteins was only achieved if (i) the cell surface proteins were incubated with the antibody (see also section D) and (ii) the streptavidin spheres were bound to the antibodies that already recognised their GFP substrates on cell surface (preincubation of spheres with antibodies was not successful, probably due to mechanical constraints that are experienced by the antibodies that are bound to the sphere). Using this assay, it can not be excluded that one antibody (which is intrinsically bivalent) is bound to two GFP-coupled cell surface proteins simultaneously. As a consequence, the experiments in section 4.4 may underestimate (maximally by a factor of 2) the diffusion coefficient of a monomeric EGFR, which is expected to diffuse faster than two EGFR that are coupled by an antibody. This uncertainty could be avoided in future experiments by developing a method that allows one to determine the exact number of molecules that are bound to the microsphere at a time, e.g. using the fluorescence of the GFP that is coupled to the proteins. This is however challenging as the GFP-proteins

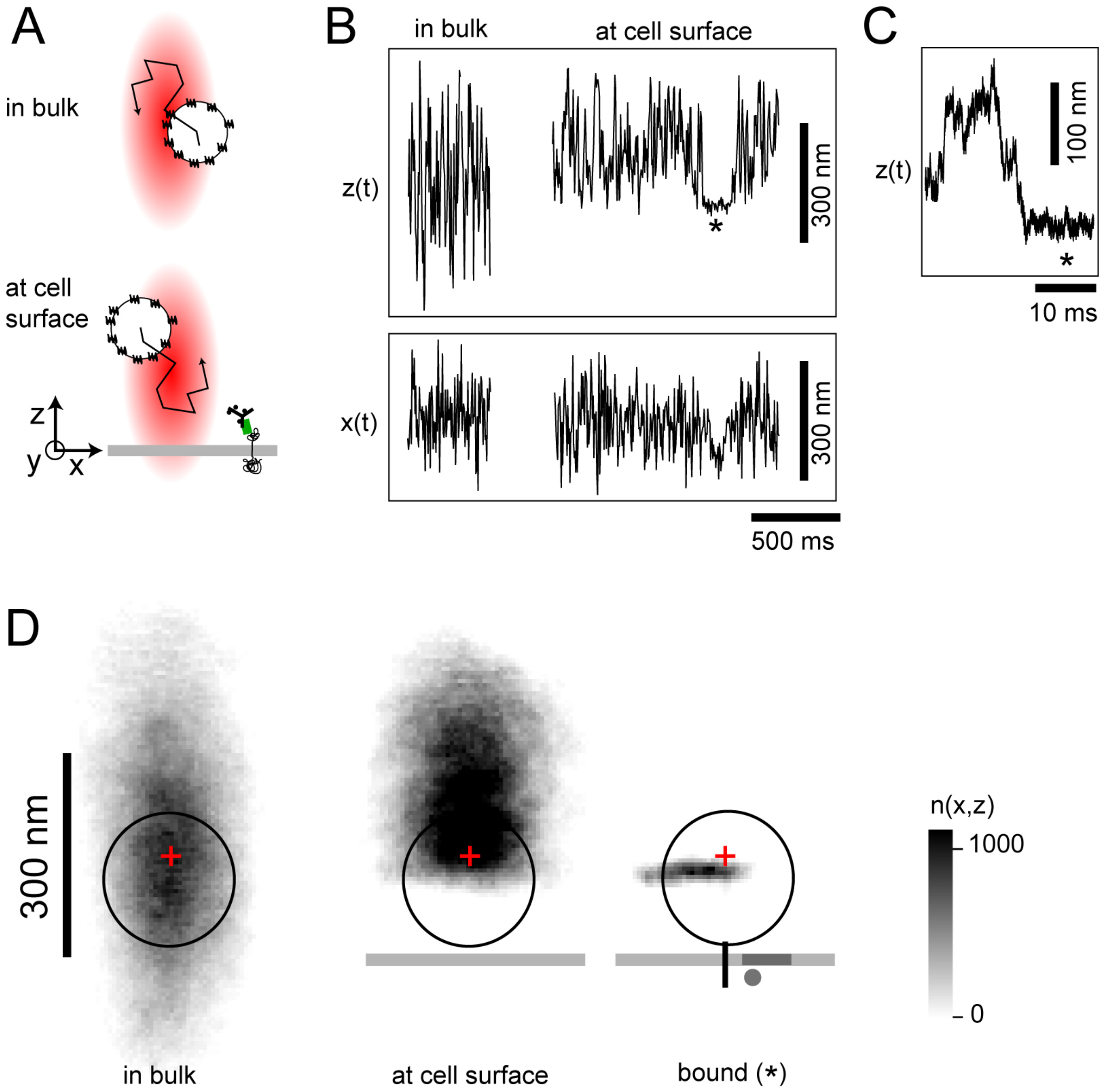

**Figure 4.3:** TNIM at a cell membrane. A) Schematics. The diffusion of a streptavidin-microsphere is confined by the optical trap (red gradient). The trap is positioned in bulk solution and then moved to the surface of a cell expressing GFP-tagged membrane molecules bound to biotinylated GFP-antibody. B) Measured position time traces of the Brownian motion of the sphere in the optical trap ($y(t)$ not shown). Positions are shown every 1 ms as lines between data points. At the cell surface, the $z$-position fluctuations are confined to the space above the cell surface. Transient binding (*) to a membrane molecule confines the motion to the cell surface. C) Enlarged view of the binding event in (B). Positions are shown every 2.5 $\mu$s as lines between data points. D) Histograms of the spheres center position calculated from 4 s (left and middle panel) or 200 ms (right panel) position fluctuations, respectively. The sphere is indicated as a black circle. The center of the optical trap is marked by a red cross. The cell surface is indicated in grey. Membrane heterogeneities hindering the lateral motion of the sphere-molecule complex are indicated in dark grey. Experimental details: sphere positions were monitored at 400 kHz; histogram binning is 5 nm; the sphere was binding to a GFP-EGFR transfected Cos7 cell; sphere radius was 125 nm.

that are bound to the microsphere would have to be distinguished from unbound GFP-proteins that diffuse in the membrane area below or next to the microsphere. It is a general challenge in SPT experiments to determine the exact number of molecules that are bound to the marker particle. In conventional SPT, marker particles are incubated with cells for minutes. Murase et al. (2004) reported that particles could be only identified as bound if they stayed at least 3 seconds on the membrane. Otherwise it was not possible to distinguish them from unbound marker particles diffusing next to the membrane. This is problematic because after the formation of the first bond, the close vicinity of the marker particle to the membrane facilitates the formation of further bonds to additional membrane molecules. Thus, to investigate diffusion of single/few membrane molecules it is advantageous to observe the motion of the marker as fast as possible after the formation of the first bond. The TNIM permits one to detect the initial binding of the marker particle and membrane molecule with millisecond temporal resolution (see Fig. 4.3). Apart from the long term observations that are discussed in section 4.3.3, only 2D-TNIM data directly (less than 1 second) after binding were evaluated ensuring that only a minimal number of membrane proteins were bound to the sphere. In fact, it was observed in most experiments that the mobility of the bound sphere gradually decreased (on a seconds timescale) after binding, indicating the formation of further bonds. In some cases a step-like reduction in the mobility was observed, indicating that the formation of individual bonds can be monitored (not shown). It would be an interesting future project to analyse this data with regards to the fundamental physics that govern the motion of a complex of proteins in a fluid lipid bilayer and also with regards to cellular signalling (see the ”oligomerisation induced trapping model” in Fig. 1.1D).

Fig. 4.3B shows a transient binding event of ca. 200 ms. The large subsequent $z$-position fluctuations indicate that the bond is released, probably due to the dissociation of the antibody from the GFP. In fact, an analysis of the distribution of binding times can reveal detailed information on antibody antigen interactions on a single molecule level as has been demonstrated by Kulin et al. (2002). Here, bonds that were stable for more than 500 ms were selected to investigate the lateral mobility of the attached membrane proteins.

The TNIM makes it possible to image the local flatness of the cell surface by the sphere's thermal position fluctuations before binding (see Fig. 4.3A). This is valuable, because a major goal of 2D-TNIM experiments is to identify structures *within* the plasma membrane that restrict the lateral mobility of the embedded molecule. It is therefore useful to control local membrane flatness, because large membrane protrusions could restrict the lateral mobility of the marker sphere. Such restrictions that act on the marker sphere would hamper the interpretation of the joint motion of marker and molecule. This is a major technological advance as video-microscopy based SPT typically lacks the axial $z$ resolution that would be necessary

to control the local plasma membrane flatness (Saxton and Jacobson, 1997).
In conclusion, a robust and general assay for binding marker particles to GFP coupled membrane proteins was established. The specificity of the assay is comparable or better compared with what is reported in recent SPT literature. Moreover, the TNIM makes it possible to observe the actual binding event with millisecond temporal resolution and to control the local flatness of the plasma membrane on a scale of tens of nanometers, thereby significantly facilitating the interpretation of the motion of the marker-protein complex.

## 4.2 Quantitative representation of 2D-TNIM data

In section 4.3, the diffusive motion of individual membrane proteins is exploited to image local properties of the plasma membrane on the molecular scale. For the evaluation of the data two important issues must be considered: first, measured position distributions are governed by both the optical trap and membrane structures. The measured distribution needs therefore to be corrected for the contribution of the optical trap. And second, the imaging process is of inherently stochastic, making it necessary to determine if observed structures are statistically significant. In the following sections, two quantification approaches for 2D-TNIM data are presented, which are both based on the evaluation of the measured "pixel occupancy" (i.e. the number of counts in each pixel of the histogram of the measured position fluctuations). Two measures are defined: (i) the Logarithmic Relative Occupancy (LRO), which corrects the measured position distribution for the optical trapping potential, and (ii) the Standardised Occupancy (SO), which indicates the statistical significance of structures that are observed in LRO images.

### 4.2.1 The Logarithmic Relative Occupancy

When unbound, the sphere's thermal position fluctuations are dominated by the optical trap. According to Boltzmann statistics, the $(x, y)$ position distribution is therefore determined by the optical trapping potential in the plane of the plasma membrane (see section 2.2.1). The corresponding position distribution $n_{tt}(x, y)$ ("tt" stands for "trap theory") for pixels with edge-length $\xi$ is (Equation (2.11))

$$n_{tt}(x, y) = N\xi^2 \frac{\sqrt{k_x k_y}}{2\pi k_\mathrm{B} T} \exp\left(-\frac{k_x x^2 + k_y y^2}{2k_\mathrm{B} T}\right). \tag{4.1}$$

The pixel occupancy is proportional to the total number, $N = t/\delta t$, of measured positions, where $t$ is the data acquisition time and $\delta t^{-1}$ the sampling frequency. Fig. 4.4B shows measured position distributions $n(x, y)$ before and after binding and the corresponding theoretically expected occupancy $n_{tt}(x, y)$.

To compare $n(x, y)$ with $n_{tt}(x, y)$, the LRO is defined:

$$\mathrm{LRO}(x, y) = \ln\left(\frac{n(x, y)}{n_{tt}(x, y))}\right) \tag{4.2}$$

The logarithm of the ratio of $n(x, y)$ and $n_{tt}(x, y)$ quantifies the deviation of the measured distribution from the theoretical expectation. For instance, LRO=0 indicates no deviation, whereas LRO=3 (LRO=-3) corresponds to a ca. 20-fold increase (decrease) in pixel occupancy. Fig. 4.4C shows the LRO as computed for the data in Fig. 4.4B. The LRO computed for the position fluctuations of the unbound sphere shows little spatial contrast, indicating that the motion of the unbound sphere is governed by the optical trap alone. The measurement did not take place in bulk solution but in direct vicinity of the plasma membrane. Protrusions that extend out of the membrane could influence the lateral motion of the sphere (see also section 4.1.4) and could could be thereby falsely interpreted as structures within plasma membrane structures, when evaluating the position fluctuations of the bound sphere. Indeed, it was sometimes observed that the position distribution before binding was not governed by the optical trap alone, and such data were generally discarded. After binding, the position distribution changes significantly: the LRO image reveals areas with up to 20-fold (LRO≈3) enhanced occupancy, whereas other areas are avoided completely ($n(x, y, )$=0 ⇔ LRO=-∞). These areas were readily accessible to the unbound sphere and can be therefore attributed to structures within the plasma membrane that restrict the diffusive motion of the molecule.

### 4.2.2 The Standardised Occupancy

The imaging process in ”Thermal Noise Imaging Microscopy” is based on Brownian motion, an intrinsically stochastic process. Thus, a measure has to be defined to quantify if observed structures are statistically significant. For confined Brownian motion in the optical trap the variance of the measured position distributions is expected to be governed by Poisson statistics for correlated data (Heermann, 2000):

$$\mathrm{var}(n(x, y)) \approx n(x, y)\left(1 + 2\frac{\tau_\xi}{\delta t}\right) \tag{4.3}$$

The latter factor in $\mathrm{var}(n(x, y))$ accounts for the possibility that the time gap $\delta t$ between subsequent observations of particle positions is on the order of the time that the particle spends in one pixel of the image ($\tau_\xi = \xi^2/(2D)$, where $\xi$ is the edge-length of one pixel), leading to correlated data. To quantify the statistical significance of differences between

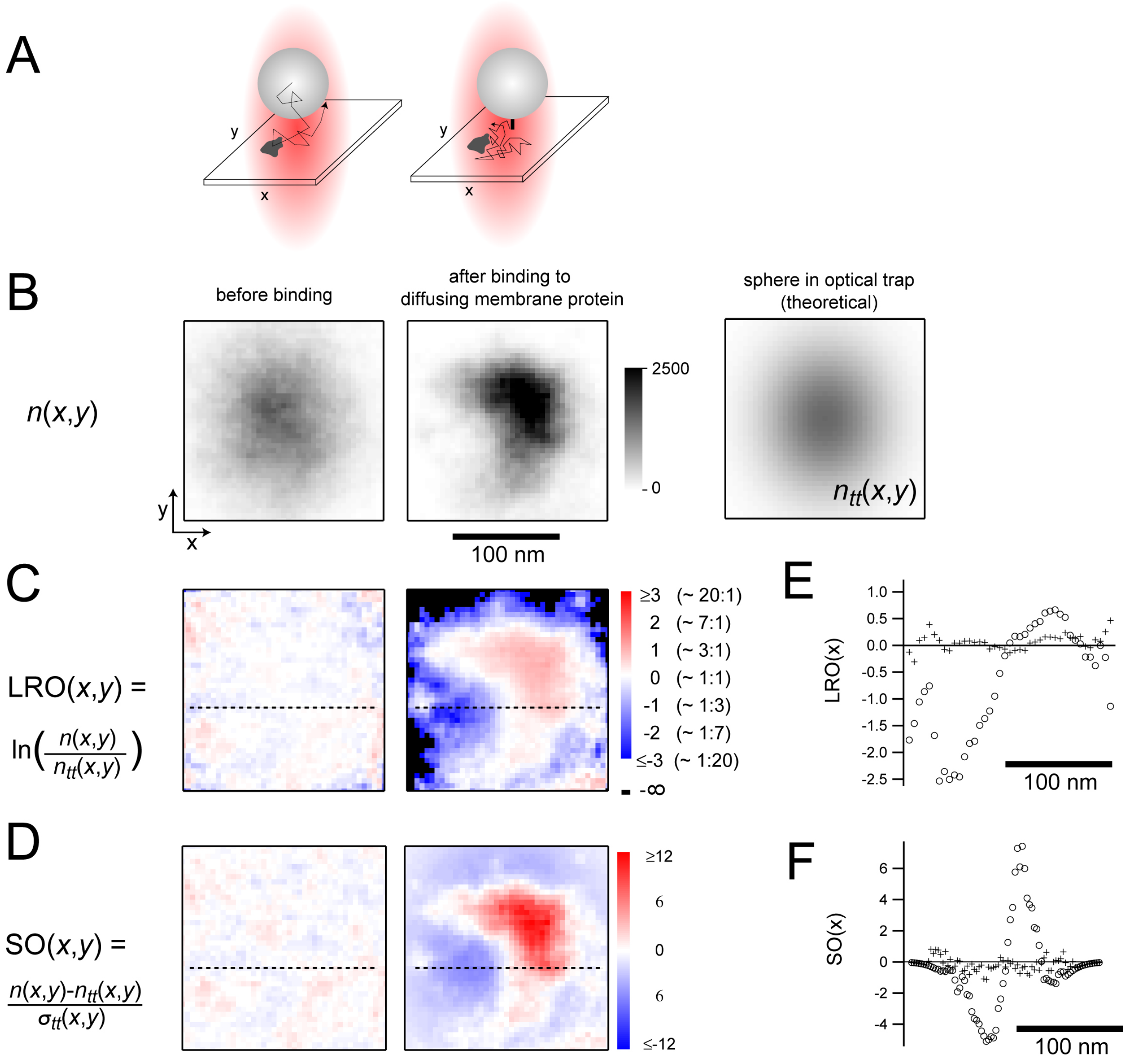

**Figure 4.4:** Quantitative representations of 2D-TNIM measurements. A) Schematics. Left panel: The Brownian motion (zig-zag arrow) of the microsphere is confined by the optical trap (red gradient) to the vicinity of the plasma membrane. Right panel: The microsphere is bound to a membrane protein and membrane lateral heterogeneities (grey area) constrain the motion of microsphere-protein complex. B) Histograms ($n(x,y)$) of the microsphere center positions. Left panel: At the cell surface before binding. Middle panel: Bound to the membrane protein. Right panel: Theoretical Boltzmann distribution of Brownian motion in the optical trap. C) LRO image as defined by Equation (4.2). Red (blue) indicates enhanced (diminished) occupancy relative to expectation for Brownian motion in the optical trap. The according fold-changes are given in brackets. For instance, 20:1 means: 20-fold more often visited by the particle than expected for a spatially homogeneous environment. D) SO images as defined by Equation (4.4). SO(x,y) gives the difference between the observed pixel occupancy and the theoretical expectation for a spatially homogeneous environment, normalised to the expected intrinsic variations owing to the imaging process. E),F) Profiles along the respective dashed lines in (C) and (D) (crosses: before binding, circles: after binding). Details: histogram binning 5 nm; $t = 2$ s per image; acquisition frequency 400 kHz; sphere binds to GFP-EGFR in a Cos7 cell membrane; sphere radius 125 nm; optical trap force constants $k_x$=2.3 fN/nm and $k_y$=1.6 fN/nm as determined from fitting a 2D Gaussian distribution to the position distribution before binding.

$n(x, y)$ and $n_{tt}(x, y)$, the "Standardised Occupancy" (SO) was defined:

$$\mathrm{SO}(x, y) = \frac{n(x, y) - n_{tt}(x, y)}{\sigma_{tt}(x, y)}, \text{ with } \quad \sigma_{tt}(x, y) = \sqrt{\mathrm{var}(n_{tt}(x, y))} \tag{4.4}$$

$\mathrm{SO}(x, y)$ normalises the observed deviations to the inherent variance of the imaging process. Fig. 4.4D shows that before binding the position distribution does not significantly deviate from confined diffusion in the optical trap. However, upon binding, the measured distribution shows deviations up to 12 $\sigma_{tt}$. Thus, the SO confirms that most structures that were seen in the LRO image in Fig. 4.4C were statistically significant. However, structures at the periphery of the imaged area are not significant in the SO representation, because positions away from the center of the optical trap are sampled less frequently (see section 2.2.4) and relative changes are determined less accurately because of low counting statistics.

### 4.2.3 Properties of the SO

The definition of the $\mathrm{SO}(x, y)$ in Equation (4.4) is similar to the definition of a standardised random variable $Z$ (Neter et al., 1991):

$$\mathrm{Z} = \frac{z - \mu_z}{\sigma_z}, \tag{4.5}$$

where $z$ is a random variable with mean $\mu$ and variance $\sigma_z^2$. It was tested if the $\mathrm{SO}(x, y)$ has the expected properties of a standardised random variable ($\mu$=0, $\sigma$=1) using position time traces as produced by Brownian dynamics simulations (see section A). Fig. 4.5A shows the result of one simulation run. For quantification, mean and standard-deviation of $\mathrm{SO}(x, y)$ images[4] were computed from 10 independent runs, yielding:

$$\begin{aligned} \langle \mathrm{SO}(x, y) \rangle &= 0.0084 \pm 0.08 & (4.6) \\ \sqrt{\left\langle (\mathrm{SO}(x, y) - \langle \mathrm{SO}(x, y) \rangle)^2 \right\rangle} &= 1.02 \pm 0.09, & (4.7) \end{aligned}$$

where brackets $\langle . \rangle$ denote averaging over all pixels in one image. It is therefore concluded that $\mathrm{SO}(x, y)$ indeed has properties of a standardised random variable when the position distribution of the particle is governed by the optical trap alone.
To check if $\mathrm{SO}(x, y)$ is sensitive to deviations, a potential $U_{add}(x, y)$ was added[5] to the optical

---

[4] The analysis as well as the graphical representation was restricted to $n_{tt}(x, y) \geq 20$.

[5] In the simulation the respective forces $F_x(x, y) = -\frac{\partial U}{\partial x}$ and $F_y(x, y) = -\frac{\partial U}{\partial y}$ were used.

trap, yielding a total potential:

$$U(x,y) = U_{trap}(x,y) + U_{add}(x,y) \tag{4.8}$$

$$U_{add}(x,y) = A \exp\left(-\left(\frac{(x-o)^2+(y-o)^2}{w^2}\right)^2\right) \tag{4.9}$$

The offset $o$ shifts the center of the additional potential relative to the center of the optical trapping potential. The width $w$ is the length-scale on which the additional potential decreases from its maximal amplitude $A$. This particular form of $U_{add}(x,y)$ was chosen because it mimics a locally less accessible membrane area. For $A = 2\ k_{\mathrm{B}}T$, $o = -20$ nm, and $w = 30$ nm the additional potential is readily detected as an area of significantly decreased occupancy (see Fig. 4.5). However, $U_{add}(x,y)$ appears deformed in the SO image, as is seen best in the line-profile in Fig. 4.5F, which does not show the symmetry of $U_{add}(x,y)$ around $x = o = -20$ nm. The reason is explained most easily by example: Consider a small area that is not accessible to the particle. If this area is positioned at the periphery of the trap, it would change the position distribution not much, because the expected pixel-occupancy at the periphery of the trap is relatively low. However, if the non-accessible area is close to the trap center it will change the position distribution more significantly, because the expected pixel-occupancy is high. Less accessible areas in the trap center appear therefore amplified in the SO images, according to their statistical significance.

### 4.2.4 Energy landscape interpretation of the LRO

If the additional potential $U_{add}(x,y)$ is temporally stable, LRO$(x,y)$ directly yields the negative of the $U_{add}(x,y)$ in units of $k_{\mathrm{B}}T$, because:

$$\mathrm{LRO}(x,y) = \ln\left(\frac{n(x,y)}{n_{tt}(x,y))}\right) = \ln\left(C\frac{\exp\left(-\frac{U_{trap}(x,y)+U_{add}(x,y)}{k_{\mathrm{B}}T}\right)}{\exp\left(-\frac{U_{trap}(x,y)}{k_{\mathrm{B}}T}\right)}\right) \tag{4.10}$$

$$= -\frac{U_{add}(x,y)}{k_{\mathrm{B}}T} + \ln(C), \tag{4.11}$$

where the offset $\ln(C)$ contains the normalising pre-factors of the Boltzmann distributions. Fig. 4.5 shows that an additional potential is indeed accurately reproduced in the LRO image.

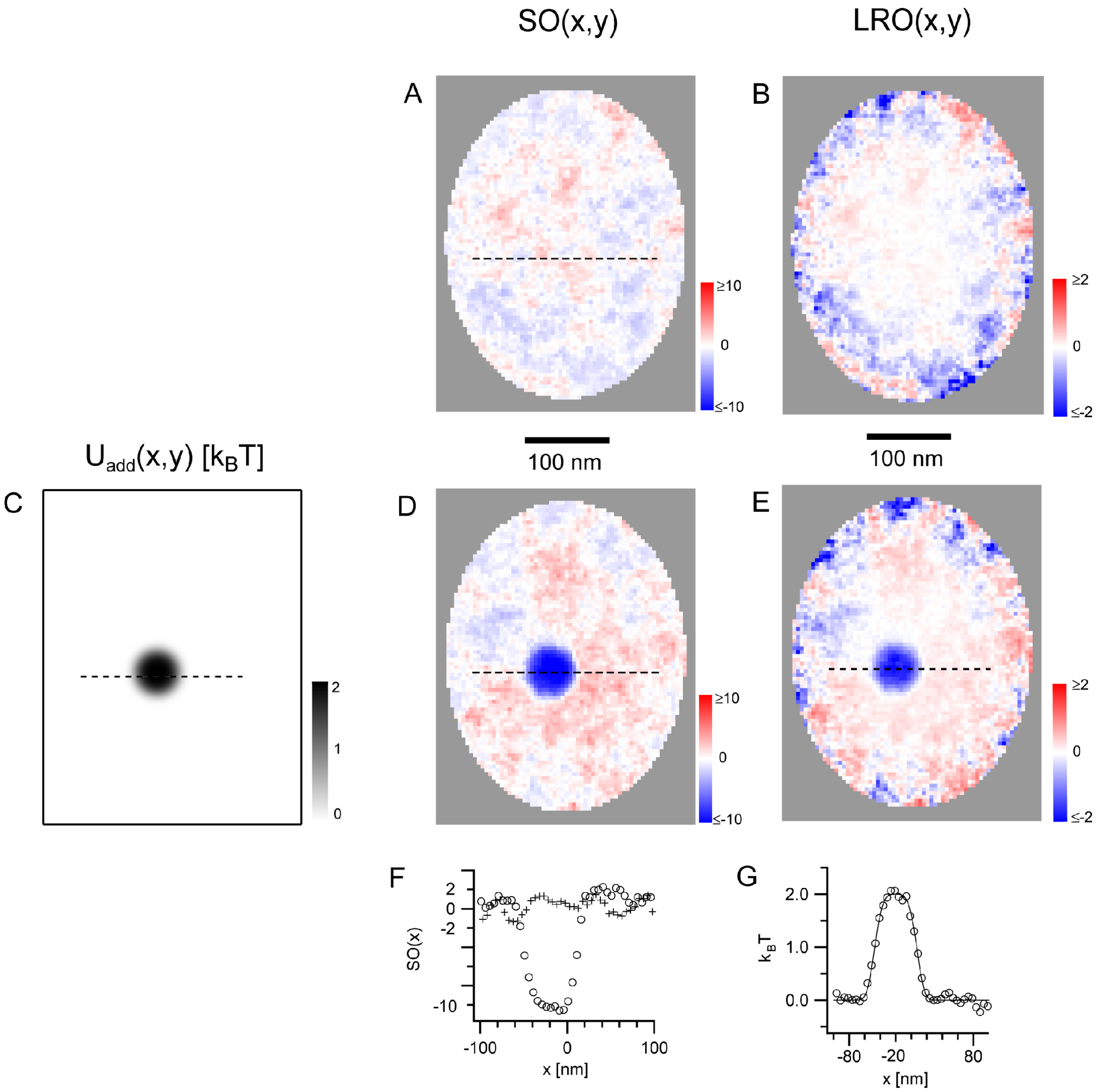

**Figure 4.5:** Brownian dynamic simulations of 2D-TNIM. The Brownian motion of the particle was simulated as confined by the optical trap alone (A, SO image; B, LRO image), or in the presence of an additional potential $U_{add}$ (C, $U_{add}$; D, corresponding SO image; E, corresponding LRO image). Images are binned at 5 nm. F) SO line profiles. SO evaluated along dashed lines in A (crosses) and D (circles). G) LRO line profile. Circles: the negative of the LRO, evaluated along the dashed line in E. Solid line: $U_{add}$, evaluated along the dashed line in C. Simulation parameters: temperature $T = 300$ K; sphere radius $a = 125$ nm; medium viscosity $\eta = 1.7 \cdot 10^{-3}$ Ns/m$^2$; trapping force constants $k_x = 1.5$ fN/nm and $k_y = 0.9$ fN/nm; sampling rate $\delta t^{-1} = 400$ kHz; total observation time $t = 4$ s.

### 4.2.5 Discussion

2D-TNIM images plasma membrane structures via the diffusive motion of individual membrane proteins. To restrict the imaging to an area of interest, the motion of the protein is confined by an optical trap that acts on an attached marker particle. The LRO was defined to correct 2D-TNIM data for the potential of the optical trap, visualising changes in pixel occupancy compared with the theoretical expectation for diffusion in a spatially homogeneous environment. Furthermore, LRO images may be interpreted as energy landscapes that quantify the interaction of the membrane molecule with the lipids and proteins in its environment. This interpretation is tempting, because it would reveal physical forces that drive partitioning of membrane molecules into certain membrane domains (see also Saxton, 1995). However, the energy interpretation of LRO images relies on Boltzmann statistics, which conventionally require energy landscapes that are static on the timescale of measurement (in TNIM typically seconds). In the case of dynamic plasma membrane structures, interpretation of LRO images requires further theoretical considerations on the applicability of Boltzmann statistics in dynamic energy landscapes.

The expected occupancy of each pixel in 2D-TNIM images has an intrinsic variance owing to the inherent randomness of diffusive motion. The SO was defined to show the difference between the measured and the theoretically expected pixel occupancy, normalised to this intrinsic variance. However, as the intrinsic variance depends on the optical trapping potential, SO images contain method specific information on the significance of observed structures, which can lead to "deformed" images. In principle, one could show both LRO and SO images for each data set to provide simultaneous information on the structure of the observed object (LRO) and the accuracy by which this structure is imaged (SO). For the sake of space it was chosen to show 2D-TNIM measurements in the LRO representation alone. However, only the central part of LRO images was shown in order to avoid the noisy areas at the periphery.

## 4.3 Submicrometer-scale constraints to membrane protein diffusion

In this section, it is demonstrated that TNIM makes it possible to study the diffusive motion of individual membrane proteins within a defined submicrometer-scale membrane area. First, it is shown that the TNIM's sensitivity allows one to distinguish constraints to the diffusion of proteins with different membrane anchoring. Next, it is shown that a detailed analysis of the data provides information on the position and shape (structure), and the temporal stability (dynamics) of these diffusion constraints. Such information is key for understanding how submicrometer-scale plasma membrane lateral heterogeneities regulate the mobility and thereby the function of membrane bound proteins such a growth factor receptors (see section 1.1 and chapter 5). The results are presented and also discussed in detail in section 4.3.2 and section 4.3.3, whereas section 4.3.4 contains a more general discussion and suggestions for future investigations.

### 4.3.1 Method

In every measurement, a 125 nm (radius) streptavidin sphere (marker particle) was trapped in bulk solution and positioned at the surface of a GFP-EGFR or GFP-GL-GPI expressing Cos7 cell, which has been incubated prior to the experiment with biotinylated GFP antibody (see Appendix D) in order to mediate the binding of the streptavidin sphere to the GFP coupled membrane protein (see section 4.1.2). Once the cell surface was approached (see section 4.1.4), position time traces of the sphere's diffusive motion were recorded at 400 kHz and stored in blocks of 4 s. LRO images based on position data of the indicated time windows were calculated as described in section 4.2.

### 4.3.2 Protein-specific constraints to diffusion

Constraints to diffusion of membrane-bound proteins are thought to be mediated by plasma membrane lateral heterogeneities that arise from the interaction of certain proteins and lipids. As the specific interaction of proteins with other proteins and/or with lipids depends on their molecular properties, it is in general expected that not all proteins "see" the same diffusion constraints. In particular, proteins with different membrane anchoring are likely to interact differently with the proteins and lipids in their local environment. Here, it was tested if GFP-EGFR and GFP-GL-GPI see a different membrane environment. GFP-EGFR is a transmembrane protein with a large (≈2 nm) cytoplasmic portion, whereas GFP-GL-GPI is a GFP that is anchored to the membrane via a lipid (GPI) that is located in the outer leaflet of the plasma membrane lipid bilayer (see Fig. 4.1). Using TNIM, it was measured "how freely" GFP-EGFR and GFP-GL-GPI are allowed to diffuse in their submicrometer-scale membrane environment. This was achieved by computing LRO images from 0.5 s directly before and from 0.5 s directly after the binding of the marker sphere. The reason for choosing this time window was that 0.5 s are long enough to allow the protein to efficiently sample the imaged area, but the transient exclusion from dynamic membrane structures is not averaged out. The percentage area accessed was computed as the percentage of pixels that the diffusing protein visited once or more ($n(x,y) \geq 0 \Leftrightarrow \text{LRO}(x,y) \neq -\infty$).

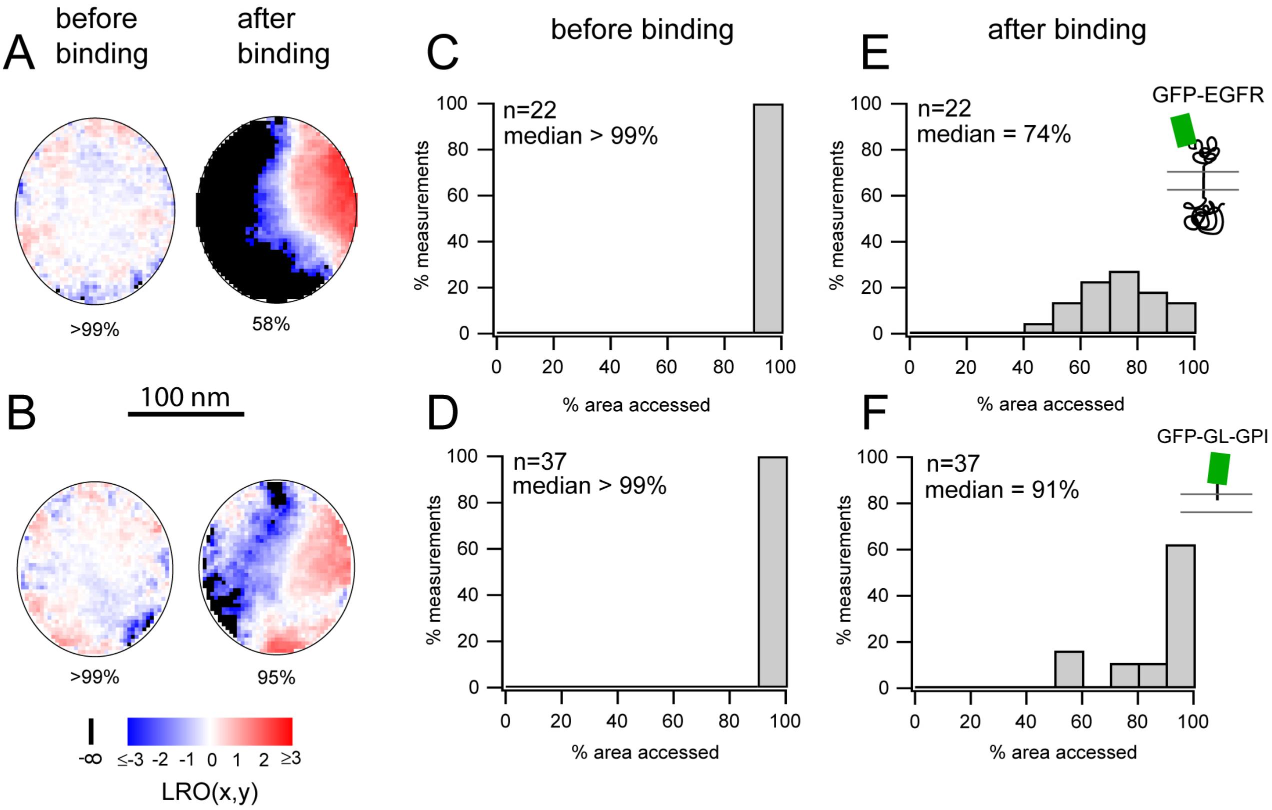

**Figure 4.6:** Membrane accessibility for GFP-EGFR and GFP-GL-GPI as measured with 2D-TNIM. A,B) Example LRO images. Left: marker-sphere at cell surface before binding. Right: after binding to GFP-EGFR (A) or GFP-GL-GPI (B). The percentage of pixels that were visited once or more (accessed area, $n(x, y) \geq 0 \Leftrightarrow \mathrm{LRO}(x, y) \neq -\infty$) is indicated. C,D) Percentage of accessed area *before* binding to GFP-EGFR (C) or GFP-GL-GPI (D) in 22 or 37 measurements, respectively. D,F) Percentage of accessed area *after* binding to GFP-EGFR (E) or GFP-GL-GPI (F) in 22 or 37 measurements, respectively.

### Results and discussion

The examples in Fig. 4.6A,B and the histograms in Fig. 4.6C,D show that the unbound marker sphere was free to access most of the imaged area, indicating that its diffusion was not restricted by cellular structures that extended out of the plane of the plasma membrane (see also section 4.2.1 and section 4.1.4). Such unrestricted lateral diffusion of the marker sphere *before* binding facilitates the interpretation of the diffusion *after* binding, because diffusion constraints can be attributed to structures within the plane of the membrane as felt by the protein. Simply put, Fig. 4.6C and Fig. 4.6D show that ”the control behaves well”. After binding to GFP-EGFR, the marker sphere did generally access less area than before binding (compare Fig. 4.6C and Fig. 4.6E), indicating that lateral membrane structures constrain diffusion of GFP-EGFR on the submicrometer scale. Furthermore, the membrane area accessed was different in individual measurements, indicating that the Cos7 plasma membrane is heterogeneous on the submicrometer scale. Most measurements on GFP-GL-GPI yielded a higher membrane accessibility than the measurements on GFP-EGFR (compare Fig. 4.6E and Fig. 4.6F), indicating that diffusion of EGFR is additionally constrained by structures that are formed by lipids and/or proteins in the inner plasma membrane leaflet and/or directly below the plasma membrane, because these are structures that GFP-GL-GPI can not directly interact with. This interpretation is supported by experiments showing respectively that disruption of the actin cytoskeleton or truncation of the cytoplasmic domains of transmembrane proteins increases the ”barrier free path” in SSRM measurements (Edidin et al., 1994) and decreases the fraction of proteins exhibiting transient confinement in SPT experiments (Sako et al., 1998) (see also section 1.2).

About 15% of the measurements on GFP-GL-GPI appeared as a separated peak in the histogram of accessed areas (Fig. 4.6F) at 50 to 60 percent accessed membrane area. Although more measurements are needed to confirm the existence of a separate popuplation, this observation is interesting with regard to the measurement of the binding specificity of the marker spheres, which indicated that every $6^{th}$ to $7^{th}$ sphere may not bind GFP-GL-GPI but some other membrane component. For this reason ($1/6.5 \cdot 100\% \approx 15\%$), the separate population in Fig. 4.6F may report the membrane accessibility for some other plasma membrane components (measurements on GFP-EGFR probably also contained few unspecific events, however they did not appear as a distinct population). An alternative explanation is that there are different populations of GFP-GL-GPI proteins that interact differently with their plasma membrane environment. In fact, there is evidence that a part of GFP-GL-GPI resides in specific lipid domains (”lipid-rafts”, see Pralle et al., 2000 and Kenworthy et al., 2004). It would therefore be an interesting future project to study if disruption of lipid rafts by cholesterol depletion (see section 1.1 or Edidin (2001b)) changes the membrane area that is accessible to GFP-GL-GPI, since there is still a debate if lipid domains such as "lipid rafts" exists *in vivo*, and if they exist, how they change the diffusive behaviour of the embedded proteins.

In conclusion, the different membrane accessibility of GFP-EGFR and GFP-GL-GPI provide evidence that GFP-EGFR interacts with structures in the inner plasma membrane leaflet and/or directly below the plasma membrane (e.g. cytoskeletal barriers), and that TNIM detects specific differences regarding the submicrometer-scale plasma membrane environment of different proteins.

### 4.3.3 Spatio-temporal dynamics of constraints

Membrane domains are generally expected to be transient and mobile (Edidin, 2001b), because they can be formed by protein-protein, protein-lipid or lipid-lipid interactions that are only kinetically stabilised by energy differences on the order of the thermal energy $k_{\mathrm{B}}T$ (Parsegian, 1995). However, one also expects stable "diffusion barriers" such as those formed by cytoskeletal structures next to the plasma membrane (see section 1.1). Thanks to the confinement of the marker-protein complex by the optical trap, TNIM can monitor the diffusion of membrane proteins in a defined membrane area over a long time. This makes it possible to obtain information on the spatio-temporal dynamics of constraints to diffusion and on resulting "membrane domains" to which the diffusion of the proteins may be confined to. *Spatial* aspects such as the size of membrane domains are important because they for instance determine how many interacting proteins are within one domain at a time, whereas *temporal* aspects, such as the lifetime of domains and transition rates of proteins from one domain to another, determine how fast a protein can react with proteins in other domains (see also chapter 5). The following examples demonstrate the detailed information on structure and dynamics of diffusion constraints that can be obtained by 2D-TNIM.

For the data shown in this section, sequences of 0.5 s LRO images were computed where the time frame was shifted by 0.125 s from one image to the next. All figures in this section are arranged such that the images in the same row contain overlapping data to reveal dynamics, whereas images in the same column are temporally independent and thereby reveal stable structures. In the lower right corner of each figure an image is shown that is computed from the total time of the sequence. Structures that are seen in temporally independent images and in the image computed from the total time are indicative of stable membrane lateral heterogeneities.

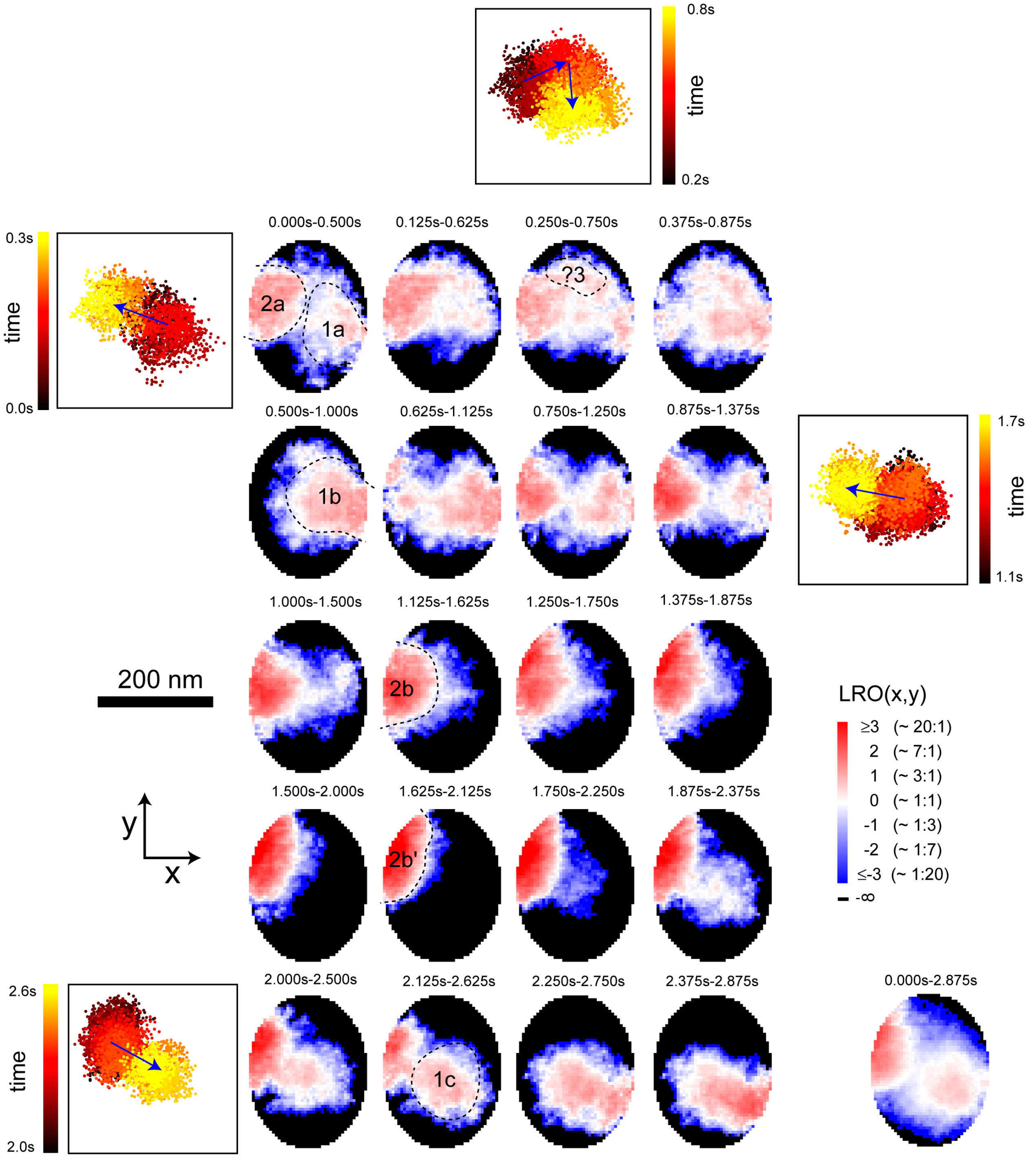

**Figure 4.7:** Temporal sequence of LRO images of one membrane area as obtained with GFP-EGFR in the plasma membrane of a Cos7 cell. The time windows from which LRO images are computed are given above the respective image. Images in the same column are temporally independent, whereas images in the same row contain temporally overlapping data. The image in the lower right corner covers the whole time of the sequence. Color encoded $x(t), y(t)$ traces indicate step-like transitions between membrane domains. Domain boundaries are indicated by dashed lines.

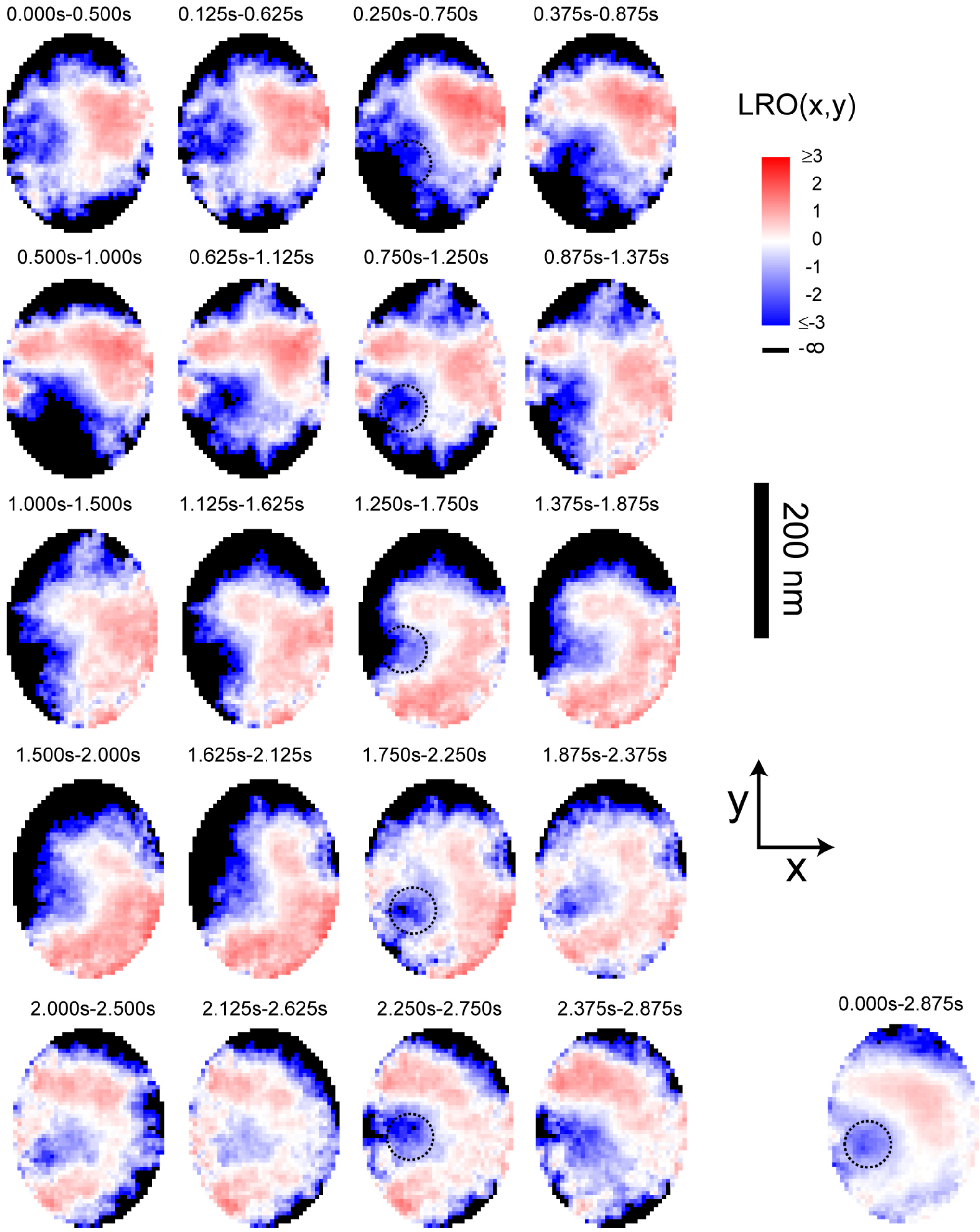

**Figure 4.8:** Temporal sequence of LRO images of one membrane area as obtained with GFP-EGFR in the membrane of a Cos7 cell. The dominant feature of this measurement is a small area (indicated by a dashed circle) that is consistently less visited than the surrounding membrane area (the same data set is also shown in Fig. 4.4).

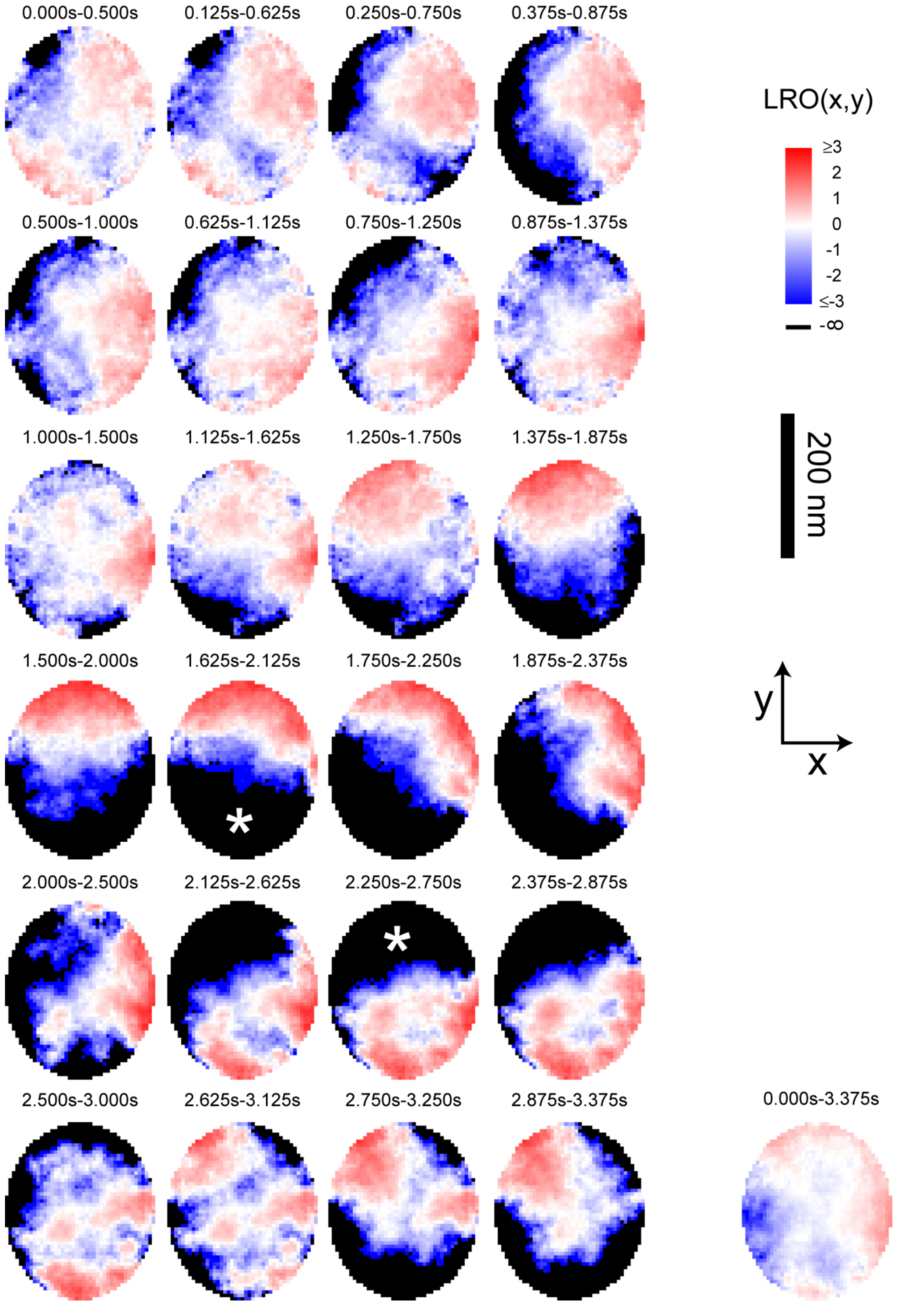

**Figure 4.9:** Temporal sequence of LRO images of one membrane area as obtained with GFP-GL-GPI in the membrane of a Cos7 cell. The stars mark two dynamic (seconds timescale) "exclusion areas".

### Results and discussion

The measurements in Fig. 4.7 indicate that the diffusion of EGFR can be transiently confined to submicrometer-scale membrane domains. The evidence for this statement will be discussed in detail in order to explain the image formation process for 2D-TNIM. In Fig. 4.7, the first image and the corresponding color encoded position time trace (0.0s-0.3s) indicate a step-like transition of EGFR from area $1a$ to $2a$. Subsequently (0.2s-0.8s), EGFR leaves area $2a$ and moves into area $1b$, possibly via a third domain in the upper part of the imaged area. Since this area is only visited for a short time ($\leq$0.1 s) it is hardly observed in the LRO-image, computed from a time window of 0.5 s. Interestingly, the size and position of the areas $1a$ and $1b$ are similar, indicating that it might be one domain, which is revisited, "domain 1". EGFR leaves the area $1b$ — again in a step-like motion (1.1s-1.7s) — into an area $2b$. The areas $2a$ and $2b$ appear similar in shape and position, indicating that these two areas might also reflect one domain, "domain 2", that is visited twice. Images during 1.125s-1.625s and 1.625s-2.125s (temporally independent data) both show the enhanced residence of EGFR in spatially similar areas $2b$ and $2b'$. The main difference in the images is due to the residual occupancy of area $1b$ that is still visible in the LRO-image computed from 1.125s-1.625s. It is therefore likely that both areas $2b$ and $2b'$ reflect "domain 2", imaged at different times. Finally EGFR leaves area $2b'$ and enters area $1c$, again in a step-like transition (2.0s-2.6s). Area $1c$ is more centered and lower than area $1a$ and $1b$. It is therefore difficult to decide if it reflects "domain 1" which slightly changed position or another domain that is located in the lower part of the image. In summary, this measurement provides evidence for repeated step-like transitions of EGFR between membrane domains that are separated by "diffusion barriers", i.e. line-like structures that are infrequently (seconds timescale) crossed by the molecule.

The dominant feature of the recording presented in Fig. 4.8 is an area of ca. 50 nm in diameter that is less accessible throughout the whole measurement (i.e. over $\approx$3 s). The existence of such exclusion from plasma membrane "nano-domains" is heavily debated in the biophysical literature (see e.g. Edidin, 2001b). The data in Fig. 4.8 clearly shows that 2D-TNIM makes it possible to image such domains and to obtain information on their spatio-temporal characteristics. Here, the center position of the domain was stable on the nanometer scale over seconds.

As discussed in section 4.2.4, LRO images could be interpreted as physical energy landscapes if the constraints to diffusion are stable on the timescale of the measurement. If so, the energy would represent the interaction of the diffusing protein with the surrounding molecules. Assuming that such an interpretation is allowed for the relatively stable exclusion area in Fig. 4.8, the forces that exclude the protein from diffusing in this area would correspond to an energy difference of about 2 $k_B$T compared with the surrounding membrane area. Thus,

this measurements indicates that TNIM is sensitive to membrane domains that are stabilised by thermal energies.
The data presented in Fig. 4.9 reveals the transient exclusion of GFP-GPI from an area with a width of ≥100 nm. In this case the exact size of the "exclusion area" can not be determined, because it extends out of the imaged area. However, it is seen that the exclusion area changes shape and position within a second. This demonstrates that 2D-TNIM can detect dynamics of plasma membrane domains at least on the seconds time scale. Notably, these transient exclusions, which are marked (*) in Fig. 4.9, are not seen in the LRO-image of the total observation time, because the time that the protein was excluded from these areas was comparably short. Thus, computing LRO images from time windows of different lengths is a means to study membrane structures of corresponding temporal stability.

### 4.3.4 Discussion and outlook

Tracking the motion of individual membrane proteins by attaching a marker particle is well established (SPT) and many authors have used this approach to infer the diffusive behaviour of plasma membrane proteins on the submicrometer scale (see section 1.2). However, one SPT trajectory is not meaningful by itself, but a large number of particle trajectories must be recorded, and analysed according to statistical criteria (Qian et al., 1991; Saxton, 1993). This is different in 2D-TNIM, because the confinement of the diffusive motion via the optical trap ensures that the molecule probes the same membrane area over a long time. Thus, statistically significant information (images) of local properties of the plasma membrane are obtained in one experiment and, furthermore, 2D-TNIM images report the specific plasma membrane environment of the protein that is used as a probe (see section 4.3.2). Time series of LRO images (section 4.3.3) demonstrated that the TNIM can provide detailed information on which part of the plasma membrane is accessible to a specific membrane bound protein at a given time. In particular, evidence was obtained that EGFR does not diffuse freely, but is excluded from submicrometer scale membrane areas, thereby providing experimental support to the notion that the cell partitions membrane bound signalling proteins such as EGFR in order to regulate their diffusive encounter and thereby their biological activity (Edidin, 2001b; Vereb et al., 2003). In general, 2D-TNIM images contain information on the interaction of plasma membrane proteins within their local environment. In 2D-TNIM the question arises as for every imaging method, if the detailed information that is contained in an image can be reduced, allowing the data to be categorised with regards to specific parameters that are of relevance for the biological function of the observed protein. Relevant parameters are expected to be (see also chapter 5): the length scales of membrane domains as formed by diffusion constraints; the temporal stability of the diffusion constraints; the "permeability" of the constraints, and the connectivity of membrane areas that are free of constraints to diffusion. A suggestion for future analysis of 2D-TNIM images would be the use of image autocorrelation to extract spatial information on membrane domains, and the use of cross-correlation on time series to reveal the dynamics of membrane domains. To obtain information on the connectivity of accessible membrane areas might require the scanning of larger membrane areas, especially if the protein of interest experiences only few constraints such as GFP-GL-GPI. This could be achieved by moving the optical trap (e.g. in steps of 100 nm) and by combining LRO images from subsequent trap positions. It has already been demonstrated in section 3.1 that this is a successful strategy to scan large volumes in 3D polymer networks. In the plasma membrane however, this is more challenging owing to the dynamics of the imaged structures. It would therefore be advantageous to minimise the time at each trap position, posing the question: what is a minimal time that is needed to obtain a meaningful 2D-TNIM image of one membrane area? This would depend on the desired accuracy. The imaging process in 2D-TNIM is diffusive motion and the accuracy depends on the expected occupancy[6] of each pixel, which rises linearly with observation time $t$ (see Equation (4.1)), and to a first approximation (Poisson (counting) statistics), the expected variance in each pixel is proportional to $1/\sqrt{t}$ (see Equation (4.3)). However, the presence of diffusion constraints changes the occupancy and therefore also the accuracy (if the motion is restricted to a small area, this area will be imaged with higher accuracy than a larger area in a given time). Further theoretical analysis and computer simulations are expected to reveal additional details on how temporal resolution and statistical accuracy are related in "diffusion-based" imaging such as it is performed in TNIM. Such analysis is also of interest with regards to the interpretation of LRO images as physical energy landscapes. If plasma membrane structures were stable, LRO images could be interpreted as the energy that separates membrane domains from each other (see section 4.2.4). This interpretation is tempting, because it would reveal the strength of the molecular forces that drive partitioning of membrane molecules into certain domains. However, structures in the membrane are dynamic and thereby preclude the application of conventional Boltzmann statistics, required for the energy landscape interpretation of the LRO, as described in section 4.2.4. Also here, further theoretical studies and computer simulations are expected to reveal how information such as physical forces and energies can be extracted from TNIM data, especially in the presence of dynamics structures. In addition, such an analysis may reveal further means (e.g. based on dynamic probability distributions, $p(x, y, t)$) to quantify the motion of membrane proteins.

In conclusion, it has been demonstrated that it is possible to employ individual membrane proteins to "scan" the accessibility of a defined submicrometer scale plasma membrane area. This

---

[6] Occupancy: the number of counts in each pixel of the histogram of the measured position fluctuations (see also section 4.2)

allows obtaining novel information on the spatial and temporal characteristics of submicrometer-scale constraints to the diffusion of plasma membrane proteins, permitting the better understanding of the kinetics by which proteins such as EGFR react with signalling partners in the membrane (see chapter 5).

## 4.4 Nanometer-scale diffusion coefficient of membrane proteins

The 2D-TNIM measurements in section 4.3 revealed submicrometer-scale constraints to the diffusive motion of EGFR, implying membrane ”domains” to which the diffusion of EGFR is temporarily restricted. It is important to know how fast membrane proteins such as EGFR diffuse within such domains, because this determines the rate at which they can interact with signalling partners in the same domain. The high spatio-temporal resolution of the TNIM makes it possible to follow the nanometer-scale motion of membrane proteins. The TNIM is therefore well suited to measure diffusion coefficients *within* submicrometer scale domains. It is crucial that both spatial and temporal resolution are high, because at low temporal resolution, most measurements will include one or more interactions of the protein with domain boundaries and do therefore underestimate the true mobility on the nanometer scale (see Fig. 4.10). With the TNIM high spatio-temporal resolution is achieved by attaching a relatively large marker particle (125 nm (radius) polystyrene sphere) to the protein of interest, yielding a ”marker-protein-complex” (MPC), a strategy commonly used in high-resolution SPT (see section 1.2). However, even though the marker is typically much larger than the protein, it does not fully dominate the motion of the MPC, because the marker resides in the extracellular medium whereas part of the protein resides in the viscous cell membrane. The extracellular medium has approximately the viscosity of water and the lipid bilayer that forms the cell membrane has a viscosity that is about 100-fold higher (e.g. Peters and Cherry, 1982 and Pralle et al. (2000)). Thus, although the protein is comparably small it is still possible to infer its mobility from the observed combined motion of the marker and the protein. Here, it is discussed how the TNIM permits one to determine the contribution of the marker to the mobility of the MPC with high accuracy. Using this information, the nanometer-scale diffusion coefficient of EGFR is calculated.

### 4.4.1 Method and results

It is assumed that the viscous drag on the marker particle and the membrane protein add up to the total viscous drag on the MPC (see e.g. Lee et al., 1993; Pralle et al., 2000; Broday,

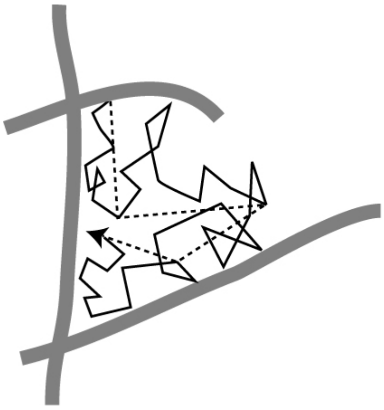

**Figure 4.10:** Diffusive displacements in the presence of constraints. Displacements observed at low temporal resolution (dashed lines) can include frequent interactions with "domain boundaries" (grey). Displacements measured at higher temporal resolution (solid lines) include on average less interactions with domain boundaries.

2002):

$$\gamma_{\mathrm{MPC}} = \gamma_{\mathrm{marker}} + \gamma_{\mathrm{protein}} \tag{4.12}$$

Although frequently used, this assumption is not trivial. In fact, the detailed physics of the combined motion of the marker and the protein depend on the surface properties of the cells and on the mechanical connection of the marker and the protein (see e.g. Broday, 2002). Here, the TNIM provides a technological advance, because the mobility of the marker can be determined directly at the membrane, directly before binding (see below). Thus, local properties of the plasma membrane that affect $\gamma_{marker}$ can be taken into account. Using $D = k_B T/\gamma$ (Einstein, 1905), Equation (4.12) yields the diffusion coefficient of the protein, corrected for the contribution of the marker:

$$D_{\mathrm{protein}} = \left( \frac{1}{D_{\mathrm{MPC}}} - \frac{1}{D_{\mathrm{marker}}} \right)^{-1} \tag{4.13}$$

Using this formula, it is possible to calculate the diffusion coefficient of the protein alone, given the diffusion coefficient of the marker particle can be determined before ($D_{\mathrm{marker}}$) and after ($D_{\mathrm{MPC}}$) formation of the MPC. Experimentally, the diffusion coefficient is determined from the mean square displacement (MSD) of the particle. In this context, only the motion parallel to the membrane is of interest (i.e. in the $(x, y)$ plane). The average mean square displacement $\mathrm{MSD}_{xy}(\Delta t)$ at lag time $\Delta t$ during a time interval $[t_i, t_{i+1}]$ was computed from

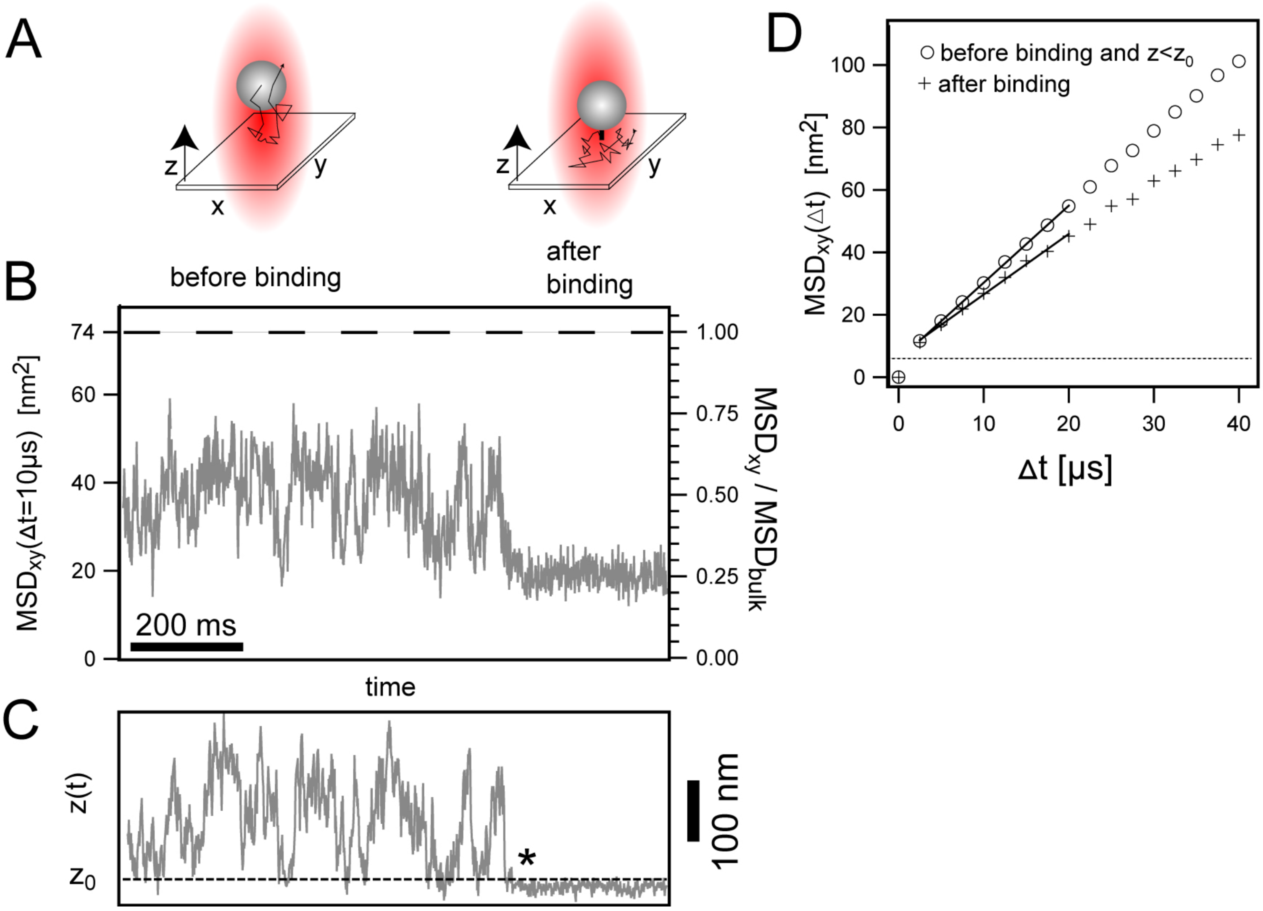

**Figure 4.11:** Diffusion coefficients of membrane proteins on the nanometer scale, measured with TNIM.
A) Schematics of the experiment. The Brownian motion of the marker-sphere is confined to the cell surface by the optical trap (left panel) and allowed to bind a membrane molecule (right panel). B) Mean square displacement for motion parallel to the cell surface (MSD$_{xy}$), at lag time $\Delta t = 10\ \mu$s. Each point represents an average over 1 ms. The right axis gives the MSD$_{xy}$ normalised to the average MSD in bulk solution (dashed line). C) Sphere position fluctuations perpendicular ($z$) to the cell surface. After binding (*) the sphere is confined to the membrane and $z(t) < z_0$ (dashed line). D) MSD$_{xy}$ before (o) and after (+) binding as a function of the lag time $\Delta t$. The MSD$_{xy}$ before binding was computed using only $x(t), y(t)$ where $z(t) < z_0$. The dashed line indicates an offset that is due to instrument noise and was subtracted in (B). Experimental details: a 125 nm (radius) streptavidin sphere was trapped above a Cos7 cell expressing GFP-EGFR. Cells were pre-incubated with biotinylated monoclonal GFP antibody to allow the sphere to bind. The $(x, y, z)$-position fluctuations of the sphere were monitored at 400 kHz.

the measured particle positions according to (see also section 2.2.3):

$$\mathrm{MSD}_{xy}(t_i, \Delta t) = \frac{1}{n}\sum_{k=1}^{n} \quad (x(t_i + (k+1)\Delta t) - x(t_i + k\Delta t))^2$$
$$+ (y(t_i + (k+1)\Delta t) - y(t_i + k\Delta t))^2 \tag{4.14}$$

with $n = (t_{i+1} - t_i)/\Delta t$.

### Mobility of the marker particle at the cell surface

Fig. 4.11B shows the $\mathrm{MSD}_{xy}$ of a 125 nm (radius) sphere while it is trapped at the surface of a Cos7 cell. The $z$-position time trace in Fig. 4.11C shows the thermal position fluctuations of the sphere perpendicular to the membrane. The $\mathrm{MSD}_{xy}$ and the $z$-position are correlated (compare Fig. 4.11B and Fig. 4.11C). The lateral mobility ($\mathrm{MSD}_{xy}$) is high if the distance to the cell membrane is large and vice versa. This is expected, because the diffusive mobility of a microsphere significantly decreases at the cell surface, partly due to hydrodynamic coupling (compare to section 3.2.5). The step-like reduction of the $z$ fluctuations in Fig. 4.11C indicates the formation of the MPC (”binding”). This is accompanied by a significant reduction of the average lateral mobility. The average lateral mobility of the sphere decreases upon binding, because (i) the sphere remains in close vicinity of the membrane, and (ii) because the attached protein slows down its motion according to Equation (4.12). To determine the diffusion coefficient of the protein these effects have to be separated.

### Mobility of the bound marker particle

Fig. 4.11D shows the lateral mobility of the MPC as a function of the lag time $\Delta t$. For short lag times, the $\mathrm{MSD}_{xy}$ rises approximately linearly[7]. This permits to calculate a diffusion coefficient ($D$) that describes the nanometer-scale mobility of the MPC. The diffusion coefficient was calculated by fitting the data to (see section 2.2.3):

$$\mathrm{MSD}_{xy}(\Delta t) = 4D\Delta t + o \tag{4.15}$$

where the offset $o$ accounts for instrument noise (see section 2.3). Fitting Equation (4.15) to the data that is shown in Fig. 4.11D yields $D_{\mathrm{MPC}}{\approx}0.52\ \mu\mathrm{m}^2/\mathrm{s}$.

---

[7] For longer $\Delta t$ the $\mathrm{MSD}_{xy}$ levels off due to lateral membrane structures that constrain diffusion and due to and the confinement by the optical trap (see section 2.2.3). The $\mathrm{MSD}_{xy}$ was not used to infer the properties of lateral membrane structures, because the quantification methods presented in section 4.2 (e.g. LRO-images) provide such information more directly.

#### Calculating the mobility of the protein alone

To calculate the diffusion coefficient of the protein alone, $D_{\text{marker}}$ is needed as well (see Equation (4.13)). The TNIM makes its possible to determine $D_{\text{marker}}$ at the same distance to the membrane as the marker has after binding, because the distance $z$ and the lateral mobility can be measured simultaneously. This is exploited by calculating the $\text{MSD}_{xy}$ before binding, however using only values $x(t)$ and $y(t)$ where $z(t)<z_0$ ($z_0$ is the maximal sphere-membrane separation after binding, compare to Fig. 4.11D). Fitting Equation (4.15) to the resulting $\text{MSD}_{xy}$ yields $D_{\text{marker}} \approx 0.62$ $\mu\text{m}^2/\text{s}$. Because both $\text{MSD}_{xy}$ before and after binding were calculated at the same sphere-membrane separation, the decrease upon binding (here ca. 20%) is attributed to the attached protein. Using $D_{\text{MPC}}$ and $D_{\text{marker}}$, the diffusion coefficient of the protein alone can be calculated according to Equation (4.13), yielding $D_{\text{protein}} \approx 3.5$ $\mu\text{m}^2/\text{s}$.

#### Nanometer-scale diffusion coefficient of EGFR

Using above method in 14 independent experiments on GFP-EGFR in Cos7 cells at ≈22°C yielded an average diffusion coefficient of

$$D = (2.8 \pm 0.4)\ \mu\text{m}^2/\text{s} \quad (n = 14)$$

Notably, the diffusion coefficients were calculated at lag times $\Delta t \leq 20$ $\mu$s, yielding corresponding displacements of the MPC of typically less than $\sqrt{50\ \text{nm}^2}=7$ nm (see Fig. 4.11D). Thus, these measurements reflect the mobility of GFP-EGFR on the nanometer scale.

### 4.4.2 Discussion

It is generally challenging to determine the mobility of membrane proteins on the nanometer scale, because single particle tracking techniques that have the necessary resolution require the use of relatively large marker particles (see section 1.2) that slow down the diffusion of the attached protein. The situation is further complicated by the fact that the bound marker particle is typically only a few nanometer above the plasma membrane and surface effects such as hydrodynamic coupling influence its mobility. Here, it was shown that the TNIM allows measuring the mobility of the marker sphere at the plasma membrane *directly before binding* in the *same distance* as it has after binding. This information can be used to determine the mobility of the protein alone, assuming that the viscous drag on the marker-protein complex is the sum of the viscous drags on the marker and the protein (Lee et al., 1993; Pralle et al., 2000; Broday, 2002). This method was used to obtain a nanometer-scale diffusion coefficient ("$D_{nano}$") of EGFR. An average value ($n = 14$) of $D_{nano} = 2.8 \pm 0.4$ $\mu\text{m}^2/\text{s}$ was obtained at

22°C in the plasma membrane of Cos7 cells on length scales smaller than 10 nm. On the nanometer scale, one would expect that the mobility of EGFR is dominated by the interaction of its transmembrane helix with the surrounding lipid molecules (see Fig. 4.1A). Smith et al. (1979) measured the diffusion coefficient of reconstituted proteins with a single transmembrane helix in a homogeneous phospholipid bilayer[8] and obtained $D = 3 \pm 0.8$ $\mu$m$^2$/s at 25°C and $4.8 \pm 1$ $\mu$m$^2$/s at 37°C using FRAP (see section 1.2). The measurement at 25°C agrees well with $D_{nano}$ of EGFR and thereby indicates that the nanometer-scale diffusion of EGFR is dominated by the lipid bilayer structure of the cell membrane. This view is further corroborated by two other studies that found mobilities consistent with the measurements by Smith et al. (1979). Using high-resolution SPT, Pralle et al. (2000) and Fujiwara et al. (2002) respectively obtained 4.2 $\mu$m$^2$/s and 5.2 $\mu$m$^2$/s for transmembrane proteins at 37°C. The agreement with the measurement by Smith et al. (1979) is remarkable, knowing that the membrane composition of most eucaryotic cells is rather complex (even on the nanometer scale) as they not only contain large amounts of cholesterol, but also a mixture of different phospholipids (Alberts et al., 2002). It would therefore be interesting to systematically measure in one cell line how the nanometer-scale mobility of plasma membrane proteins depends on temperature. Comparing such measurements with measurements in model lipid bilayers may provide novel insight into how cells regulate the fluidity of the plasma membrane (Alberts et al., 2002).

In a homogeneous lipid bilayer one expects that the diffusion coefficients on the nanometer and on the micrometer scale are similar and that FRAP experiments can therefore be used to infer the nanoscale mobility of embedded proteins. However, FRAP experiments on EGFR mobility in cells yield values that are more than 10-fold lower than the $D_{nano}$ that was measured with the TNIM (values range from 0.015 to 0.2 $\mu$m$^2$/s, see Schlessinger et al., 1978; Zidovetzki et al., 1981; Hillman and Schlessinger, 1982; Rees et al., 1984; Livneh et al., 1986; Benveniste et al., 1988). The 2D-TNIM measurements in section 4.3 suggest that submicrometer-scale constraints to diffusion are the reason for the low mobility of EGFR on the micrometer scale. However, none of the mentioned studies used the same cell line that was used in this work. To directly test if the mobility of EGFR is less on the micrometer scale than nanometer scale, FRAP experiments were performed on GFP-EGFR in Cos7 cells (see Appendix B). It was found that diffusion of EGFR is indeed over an order of a magnitude slower in the same cell line.

---

[8] M-13 coat protein was reconstituted in a DMPC bilayer. DMPC: 1,2-dimyristoyl-sn-glycero-3-phosphatidylcholine

### 4.4.3 Outlook: spatially resolved membrane protein mobility

Above section showed that the TNIM makes it possible to determine an average nanometer-scale mobility of a membrane protein. However, it was shown in section 3.2 that the TNIM can even resolve *spatial variations* of diffusive mobilities on the nanometer scale. In these measurements diffusion was influenced by hydrodynamic coupling of the probe sphere to rigid microscopic structures (3D-TNIM).

Fig. 4.12 shows the first spatially resolved TNIM measurements of membrane protein mobility, computed at lag time $\Delta t$=10 $\mu s$ (see section 3.2.1). The mobilities in Fig. 4.12C are normalised to the average mobility of the marker sphere before binding ($\langle D_{bb} \rangle$). Before binding, there is no systematic spatial contrast in the local mobility map (see Fig. 4.12C:left and Fig. 4.12D), only the statistical noise increases toward the periphery of the optical trap as it is expected (see section 3.2.3). However, once the marker sphere is bound there is a systematic decrease towards the "domain boundary" (the LRO-images indicate a confinement of GFP-EGFR to one membrane domain of ca. 150 nm in diameter, see Fig. 4.12B). Both the confinement and the local mobilities appear very similar in two independent time windows of the measurement, indicating stable domain boundaries and a stable measurement.

In conclusion, evidence is provided that the TNIM is sensitive to spatial variations of membrane protein mobility, showing great promise for testing current models of membrane domain formation. For instance, the "anchored membrane-protein picked model" that was recently reviewed by Ritchie et al. (2003) is based on the "circumferential slowing and steric hindrance of transmembrane proteins anchored to the actin-based membrane skeleton" (Murase et al., 2004). According to this model one would expect a decreased mobility close to membrane domain boundaries (Sperotto and Mouritsen, 1991; Almeida et al., 1992). However, there is yet no experimental evidence for such effects and the TNIM could be used to systematically investigate this and other models. In fact, the shown measurement provides preliminary evidence for slow diffusion at domain boundaries.

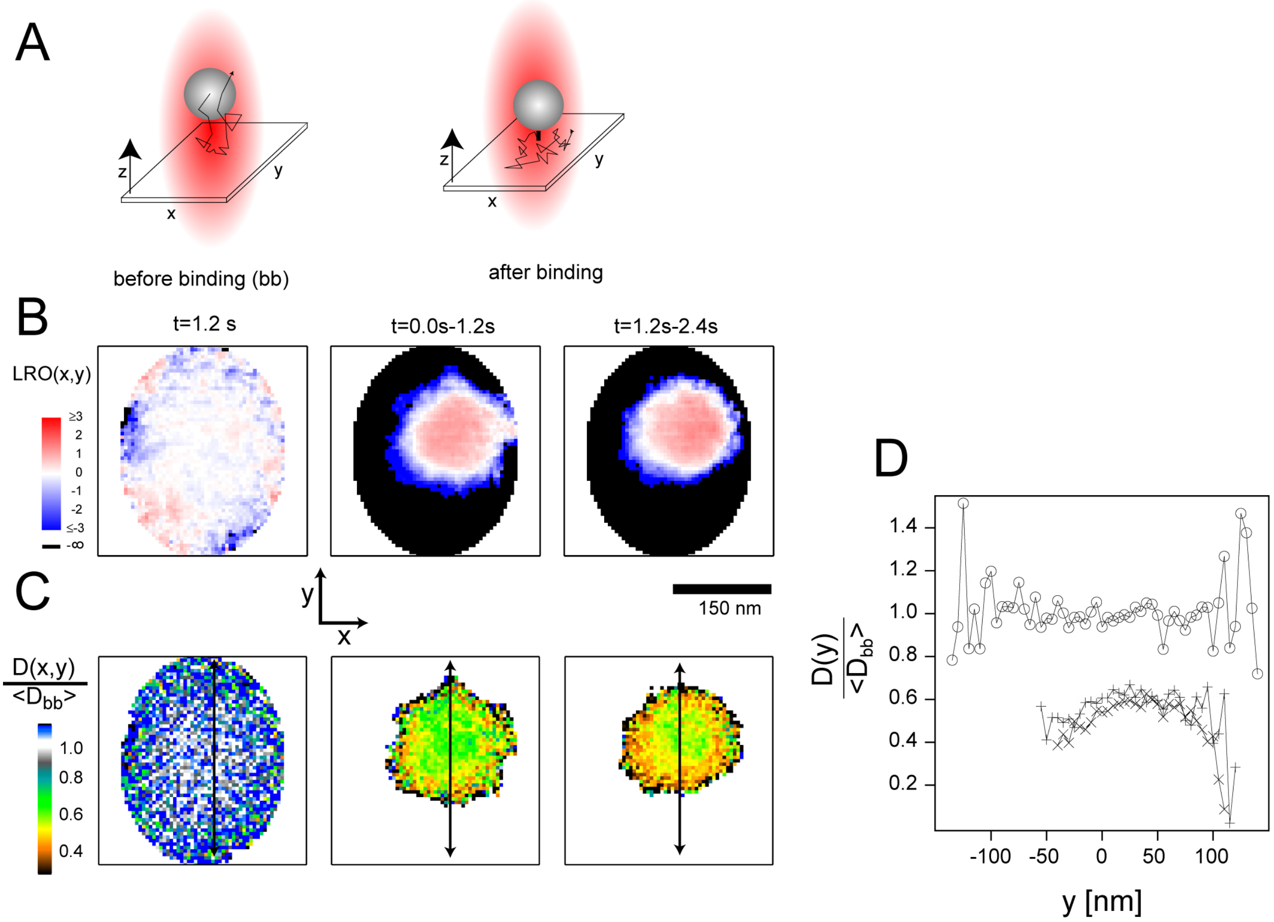

**Figure 4.12:** Measuring spatially resolved membrane protein mobility with the TNIM.
A) Schematics of the experiment. B) LRO-images. Left panel: LRO image computed from 1.2 s before binding. Middle and right panel: LRO-images computed from the indicated time window after binding. C) Mobility maps. The mobility for motion in $x, y$ in each pixel is normalised to the average mobility before binding. D) Mobility line-profiles along the arrows in (B) before binding (o), and after binding (+: t=0s–1.2s) (x: t=1.2s–2.4s). Experimental details: marker-sphere radius 125 nm; pixel-width 5 nm; positions were measured at 400 kHz; the binding was to GFP-EGFR in a Cos-7 cell.

# 5. EGFR diffusion and activation

## Chapter outline

On a molecular level, EGFR activation is thought to comprise the following steps: (i) two EGFR encounter each other by diffusion, (ii) eventually an encounter leads to binding (dimerisation), and (iii) transautophosphorylation occurs (one receptor phosphorylates the other). The EGFR mobility measurements in this work provide novel quantitative insight into the first step, namely the diffusive encounter. In fact, kinetic parameters describing both the binding step and the catalytic step are currently not known for EGFR under physiologically relevant conditions. However, the mobility measurements in this work allow one to estimate the *maximal* rate of EGFR activation, because the diffusive encounters of EGFRs impose a physical limit to the reaction. Still, it is not trivial to determine such diffusion-limited reaction kinetics, because diffusion takes places in the highly heterogeneous plasma membrane (see chapter 4). Even in homogeneous media, different calculations of the rate of bi-molecular diffusive encounters of identical reactants are reported (reviewed by e.g. Keizer, 1987). Within the scope of this work however, it is important that all approaches (e.g. mean passage time theory, statistical nonequilibrium thermodynamic theory, or numerical simulations) predict that the encounter rate is proportional to the reactants diffusion coefficient. In this chapter, this result is used to estimate the maximal (diffusion limited) rate of EGFR activation, given the experimental data on the mobility of EGFR that were obtained in this work.

## 5.1 Introduction

The epidermal growth factor receptor (EGFR) is an intensively studied transmembrane protein belonging to the family of receptor tyrosine kinases (RTKs) that control important cellular processes such as proliferation, migration, or differentiation (Schlessinger, 2000). EGFR consist of an extracellular portion that binds EGF, a single transmembrane helix, and a cytoplasmic portion that possesses tyrosine kinase activity (Fig. 5.1). The binding of EGF to monomeric receptors is thought to stabilise a dimeric receptor configuration that facilitates transautophosphorylation of tyrosine residues in the juxtaposed cytoplasmic domains of the dimer (Hubbard and Till, 2000). Autophosphorylated phosphotyrosine residues within specific sequence contexts serve as recruitment sites for proteins containing phosphotyrosine-recognition modules, such as the Src homology 2 (SH2) domain or the phosphotyrosine-binding (PTB) domain (Pawson, 2002). The binding of these adapter proteins initiates specific signalling cascades such as the MAPK pathway that mediate the cellular response (Yarden and Sliwkowski, 2001).

## 5.2 Diffusion mediated encounters of EGFR

Although ligand stabilised dimerisation is the main (physiological) trigger of EGFR activation, there is also evidence that ligand-independent collisions (transient dimerisation) of EGFR can result in transautophosphorylation (Hubbard et al., 1998; Reynolds et al., 2003). It is thought that the diffusive encounter of individual EGFR is the essential first step in both ligand dependent and ligand independent EGFR activation. Here, the rate of diffusion mediated encounters of EGFRs is discussed in the light of the experimental data on EGFR mobility and surface density that were obtained in this work.

### 5.2.1 Theory

The rate constant $k_D$ at which the diffusive encounter of two reactants takes place in a two-dimensional system is given by (see e.g. Lauffenburger and Linderman, 1993)[1]:

$$k_D = \frac{2\pi D}{\ln(d/r_e)}, \quad \text{for} \quad d \gg r_e \tag{5.1}$$

---

[1] Interestingly, it is not trivial to calculate the encounter rate in 2D systems and different authors come to different conclusions regarding the exact form of Equation (5.1). Keizer (1987) discusses different approaches to calculate $k_D$, which result in different constants $C$ that are subtracted from the term $\ln(d/r_e)$ in the denominator of Equation (5.1). Reported values of $C$ vary from minimally 0 (Lauffenburger and Linderman, 1993) to maximally 0.75 (Berg and Purcell, 1977). Adam and Delbrück (1968) and Keizer (1985) report values inbetween. The exact value of $C$ does not effect the discussions in this chapter and for the sake of simplicity we therefore set $C = 0$.

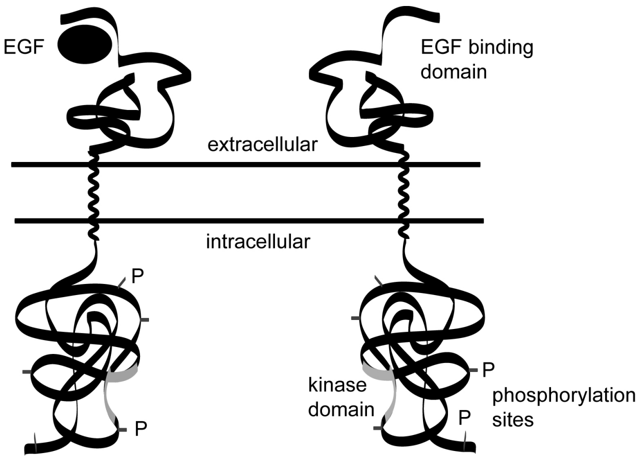

**Figure 5.1:** Schematic depiction of two EGF receptors, one bound to EGF. EGFR consist of an extracellular portion which binds EGF, a transmembrane helix, and a cytoplasmic portion which possesses tyrosine kinase activity (depicted in grey). EGFR possesses multiple intracellular tyrosine residues that can be phosphorylated (depicted as dashes).

Thus, the encounter rate constant is proportional to reactants' diffusion coefficient $D$. Furthermore, $k_D$ depends on the ratio of the two length scales that characterise diffusive encounter. First, $d$ is the characteristic distance between the molecules, which is specified by $\pi d^2 = \sigma_R^{-1}$, where $\sigma_R$ is the surface density of molecules in $\#/\mu\mathrm{m}^2$ (Lauffenburger and Linderman, 1993)[2]. And second, $r_e$ is a fictitious *encounter radius* which reflects the distance at which binding can occur. A comparison of Equation (5.1) to experimental data shows that $r_e$ typically corresponds to the physical extend of the reactants (Keizer, 1987). For calculating the values shown in Fig. 5.2C and Fig. 5.3B $r_e$ was set to 1 nm, reflecting the typical length scale[3] of the lateral extensions of the EGFR protein (see Fig. 4.1A). Replacing $d$ and $r_e$ in Equation (5.1) yields:

$$k_D = \frac{2\pi D}{\ln\left(1/\left(\sqrt{\pi\sigma_R}\cdot r_e\right)\right)} \tag{5.2}$$

Consequently, the kinetics of the diffusion limited formation of receptor dimers are described by

$$\frac{d\sigma_{RR}}{dt} = k_D \sigma_R^2 \tag{5.3}$$

where $\sigma_{RR}$ is the surface density of dimeric receptors.

---

[2] If $N$ is the total number of receptors in a membrane with area $A$, then $d$ can be calculated from the relation $N\pi d^2 = A$, where $\sigma_R = N/A$

[3] For comparison, a rather large value for $r_e$ appears to be around 4 nm (see Fig. 4.1A). $r_e = 4$ nm yields for the logarithm in the denominator of Equation (5.2) about 1.5 for $\sigma_R = 1000/\mu\mathrm{m}^2$ and about 4.9 for $\sigma_R = 1/\mu\mathrm{m}^2$, whereas $r_e = 1$ nm yields about 2.9 for $\sigma_R = 1000/\mu\mathrm{m}^2$ and about 6.3 for $\sigma_R = 1/\mu\mathrm{m}^2$, respectively. The explicit choice of $r_e$ may therefore affect the calculated encounter rate by about a factor of two, given relevant surface densities of EGFR (compare to Fig. 5.2C).

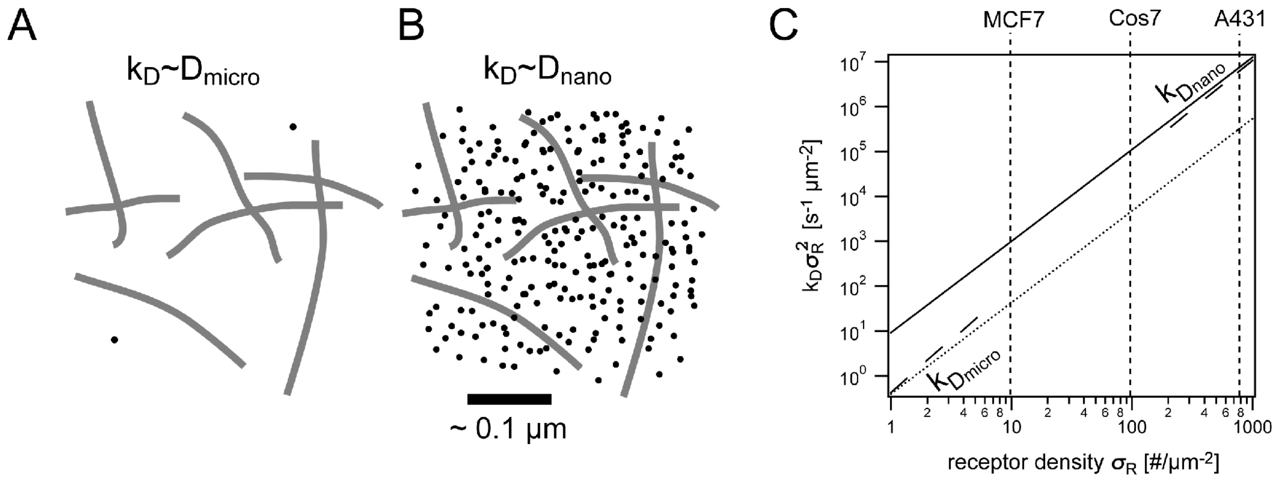

**Figure 5.2:** Encounter rates in the presence of constraints to diffusion on the submicrometer scale. A,B) Schematic depiction of receptor molecules (dots) in a heterogeneous membrane. The grey lines indicate diffusion barriers. C) Encounters per time per area. The bi-molecular encounter rate constant $k_D$ was calculated according to Equation (5.2) using the diffusion coefficient of EGFR as measured in Cos7 cells on the nanometer scale $D_{nano} = 2.8 \pm 0.4$ $\mu$m$^2$/s (solid line) and on the micrometer scale $D_{micro} = 0.12 \pm 0.02$ $\mu$m$^2$/s (dotted line). The broken line indicates an encounter rate that takes into account membrane lateral heterogeneities on the submicrometer scale. The dashed vertical lines indicate the EGFR surface densities that were measured in Appendix C.

### 5.2.2 Discussion

The encounter of individual EGF receptors is important for their activation, because it promotes their dimerisation which is essential for transautophosphorylation. Mathematical models of EGFR mediated signal transduction consequently comprise kinetic equations such as Equation (5.3), that include a rate constant $k_D$ at which the diffusive encounter of two receptors takes place (Lauffenburger and Linderman, 1993; Kholodenko et al., 1999; Hendriks et al., 2003). Importantly, the rate constant $k_D$ is proportional to the diffusion coefficient of the receptor. In this work, diffusion coefficients of EGFR have been obtained at two length scales. TNIM measurements yielded $D_{nano} = 2.8 \pm 0.4$ $\mu$m$^2$/s on length scales smaller than about 10 nanometer (section 4.4), whereas FRAP measurements yielded $D_{micro} = 0.12 \pm 0.02$ $\mu$m$^2$/s on length scales larger than about 0.3 micrometer (section B). Furthermore, TNIM measurements provided evidence for lateral membrane structures that constrain the diffusion of EGFR on the submicrometer scale (section 4.4). These findings indicate that it is not sufficient to use one diffusion coefficient in order to describe the kinetics by which the receptors encounter each other. Rather, a scenario as depicted in Fig. 5.2 seems more realistic. At low receptor surface densities, the encounter rate $k_D$ is dominated by constrained diffusion on the submicrometer scale and is better described using $D = D_{micro}$ in Equation (5.2). At high receptor surface densities, receptors can interact on small length scales where diffusion is less constrained and $k_D$ is better described using $D_{nano}$. In Fig. 5.2C the diffusion limited rate of receptor dimerisation (Equation (5.3)) is depicted as a function of the receptor surface density $\sigma_R$, calculated for both $D_{nano}$ and $D_{micro}$.

Current models of EGFR signalling assume that $k_D$ is described by one diffusion coefficient that is between 0.01–0.1 $\mu\text{m}^2/\text{s}$, as is typically obtained for membrane bound proteins by micrometer scale FRAP measurements (Lauffenburger and Linderman, 1993; Kholodenko et al., 1999; Hendriks et al., 2003). The kinetics of EGFR dimerisation may therefore be underestimated by factors of 10 to 100, depending on EGFR surface density. In fact, how much the encounter rate influences the overall kinetics of EGFR activation depends on many parameters such as the affinity of receptors or the intrinsic catalytic kinase rate constant. Almost all of these values are currently not known for physiologically relevant conditions, owing to the experimental difficulties in working with membrane bound proteins. Such important information might become available in the future using fluorescent bio-sensors that report the state of EGFR *in vivo* (Offterdinger et al., 2004). The combination of these parameters with the encounter rates determined from parameters measured with TNIM are expected to yield an improved quantitative understanding of EGFR activation kinetics.

In addition to the kinetics of ligand mediated EGFR dimerisation, the frequency by which individual EGFR encounter each other is also important with regard to ligand independent EGFR autoactivation, which is associated with uncontrolled cell proliferation (Libermann, 1985; Gullick, 1991; Salomon et al., 1995). EGFR possesses basal kinase activity (i.e. diffusive encounters of EGFR can lead to transautophosphorylation in the absence of ligand, see e.g. Reynolds et al., 2003). According to the model that is depicted in Fig. 5.2, diffusive encounters and subsequent transautophosphorylation events would be rare at low EGFR surface densities and could therefore be counteracted by the "house-keeping" activity of protein tyrosine phosphatase (PTP) (Östman and Böhmer, 2001). However, upon EGFR overexpression, the number of auto-activation events could rise strongly, not only because there are more receptors but also because receptors can interact on small length scales, where diffusion is less constrained. To further study the important connection of EGFR surface density, encounter rates and trans-autoactivation events, it is proposed to perform computer simulations on diffusion-reaction events in nonhomogeneous 2D media. Important parameters like the length scale of diffusion constraints, temporal stability of diffusion constraints, the "permeability" of constraints and the connectivity of membrane areas that are free of constraints to diffusion will become available through further analysis of 2D-TNIM data.

## 5.3 Lateral signal propagation in the membrane

Submicrometer-scale constraints to diffusion of EGFR have interesting implications for EGFR signal propagation within the membrane. On one hand, the binding of the growth factor EGF to monomeric receptors could mediate fast dimerisation, because adjacent receptors could interact within one membrane domain. On the other hand, the activated dimeric complex would diffuse relatively slowly over long distances, because of constraints to diffusion on the submicrometer scale. Plasma membrane diffusion constraints on the submicrometer scale appear therefore ideal to allow for a fast ligand-initiated dimerisation response, but still preserve information on where the dimerisation occurred. This is advantageous regarding the role of EGFR in cell migration, where it is important to preserve the directionality of the signal (see e.g. Kempiak et al., 2003).

However, there are also reports that describe that local stimulation of EGFR in fibroblast cells results in the global phosphorylation of EGFR as soon as 1 minute after stimulation (Verveer et al., 2000; Sawano et al., 2002; Reynolds et al., 2003). There are also reports about non-local phosphorylation responses of nerve growth factor (NGF) receptor TrkA (a member of the RTK family) to stimulation with NGF. 1 to 15 minutes after application of NGF to distal neuronal axons, increased TrkA phosphorylation was observed in the approximately 1 millimetre distant cell bodies. However, no NGF could be detected in the cell bodies even 30 minutes after stimulation (Senger and Campenot, 1997; MacInnis and Campenot, 2002). It is not well understood what the underlying mechanism of such RTK signal propagation is. The long range (micrometer-scale) diffusion of locally activated receptors is highly unlikely. Given the mobility of EGFR on the micrometer scale in Cos7 cells ($D_{micro} \approx 0.12\ \mu\text{m}^2$, see section B) it would require about $\Delta t \approx 14$ minutes to propagate a signal a distance of $\rho$=20 $\mu$m (typical extend of fibroblast cells) by simple diffusion ($\Delta\rho^2 \approx 4 D_{micro} \Delta t$), which is too slow to explain the experimentally observed time-scales (see above). Senger and Campenot (1997) and Reynolds et al. (2003) proposed that non-local phosphorylation responses could be mediated by self-propagated phosphorylation that travels along the plasma membrane. The key idea behind this notion is that RTKs such as EGFR are autocatalytic proteins and the intrinsic kinase activity of many RTKs is enhanced upon phosphorylation: insulin receptor (Ellis et al., 1986), fibroblast growth factor receptor (Mohammadi et al., 1996), EGFR (Bertics and Gill, 1985; Hsu et al., 1991), vascular endothelial growth factor receptor (Kendall et al., 1999), platelet derived growth factor receptor (Fantl et al., 1989), Met (Longati et al., 1994), and TrkA (Mitra, 1991). This ranges from a modest three-fold enhancement of the basal kinase activity to the case where there is no detectable kinase activity in the unphosphorylated form of the receptor. It appears therefore feasible that cascades of phosphorylation-activation events propagate along the plasma membrane, where the diffusive encounter of an activated receptor with a non-activated receptor leads to the phosphorylation and thereby activation of the latter. It is well known that such a coupling of reaction and diffusion is advantageous in order to transmit a signal over long distances (see e.g. Murray, 2002 and references therein). Recently, it has also been appreciated that intracellular signal propagation could be mediated by autocatalytic reactions (Castiglione et al., 2002; Kholodenko, 2003). Here, diffusion limited (i.e. maximal) speeds of phosphorylation propagation in the plane of the plasma membrane are discussed in the light of the experimental data on EGFR mobility and surface density that has been obtained in this work.

### 5.3.1 Theory

To estimate the speed by which RTK activation could spread within the plasma membrane it is for simplicity assumed that only phosphorylated receptors possess kinase activity (i.e. there is no basal kinase activity). It is further assumed that all reactions are diffusion limited and that once the receptors phosphorylate each other they separate quickly such that the fraction of receptors in a complex can be neglected. Under these assumptions the average time that an activated receptor diffuses until it meets and phosphorylates an unphosphorylated substrate receptor can be estimated by the reciprocal of the pseudo-first order rate constant $k_D\sigma_R$ (Keizer, 1987):

$$\Delta t = (k_D\sigma_R)^{-1} \tag{5.4}$$

where $\sigma_R$ is the local concentration of unphosphorylated receptors (it is essential to point out that as phosphorylation proceeds dynamically, the density of unphosphorylated receptors $\sigma_R$ will diminish, ultimately leading to a complete stop of phosphorylation propagation). The distance that phosphorylation is propagated during $\Delta t$ can be estimated from the receptors mean square displacement in the plane of the membrane, which is given by (see section 2.2.3):

$$\left\langle \Delta r^2 \right\rangle = \sqrt{4D\Delta t} \tag{5.5}$$

leading to an average travelled distance of

$$\Delta r \approx \sqrt{4D\Delta t} \tag{5.6}$$

This is sufficient to calculate the diffusion limited speed $v_{max}$ of phosphorylation propagation (using Equation (5.4) and Equation (5.6)):

$$v_{max} = \frac{\Delta r}{\Delta t} = \sqrt{\frac{4D}{\Delta t}} = 2\sqrt{D k_D \sigma_R} \tag{5.7}$$

Replacing $k_D$ by Equation (5.2) finally yields:

$$v_{max} \approx 2D\sqrt{\frac{2\pi\sigma_R}{\ln\left(1/\left(\sqrt{\pi\sigma_R}\cdot r_e\right)\right)}} \tag{5.8}$$

Thus, this analysis indicates that the diffusion limited speed of phosphorylation propagation is proportional to the diffusion coefficient of the receptor. Equation (5.8) indicates further that the speed also increases (in a more complex way) with the surface density of receptors. This result reflects the mechanism of phosphorylation propagation because both high mobility and short distances between adjacent receptors facilitate phosphorylation propagation.

### 5.3.2 Discussion

Fig. 5.3B shows the diffusion limited speeds (i.e. assuming diffusion limited transautophosphorylation reactions) of phosphorylation propagation for a physiologically relevant range of parameters. Interestingly, diffusion limited phosphorylation propagation is fast enough to capture the experimental time scales of micrometers per second (see above), even at low expression levels such as in MCF7 cells. However, one must for many reasons expect that the described mechanism will be slower *in vivo*. One reason is that transautophosphorylation of receptors is in general a complex process that includes the diffusive encounter, but also the actual binding step and the catalytic phosphorylation step. In fact, a complete model of phosphorylation propagation must include all these steps, where each step will reduce the overall speed of propagation. In addition, protein tyrosine phosphatase (PTP) that counteract phosphorylation can be expected to decrease the speed of phosphorylation propagation, because they counteract the propagation by dephosphorylation of receptors (see also Castiglione et al. (2002)). At high expression levels, however, the calculated diffusion limited speed, $v_{max}$, is 10 to 100 fold higher than necessary to explain the experimental observation. Thus, even if phosphorylation propagation is slower *in vivo* by factors of ten to hundred, the experimentally observed results may be explained by such a mechanism. The speed of phosphorylation propagation in the presence of diffusion barriers such as observed by 2D-TNIM (chapter 4.3) will depend on the length scale of diffusion barriers, the transition rate above ("permeability of") diffusion barriers, and the connectivity of membrane areas that are free of diffusion bar-

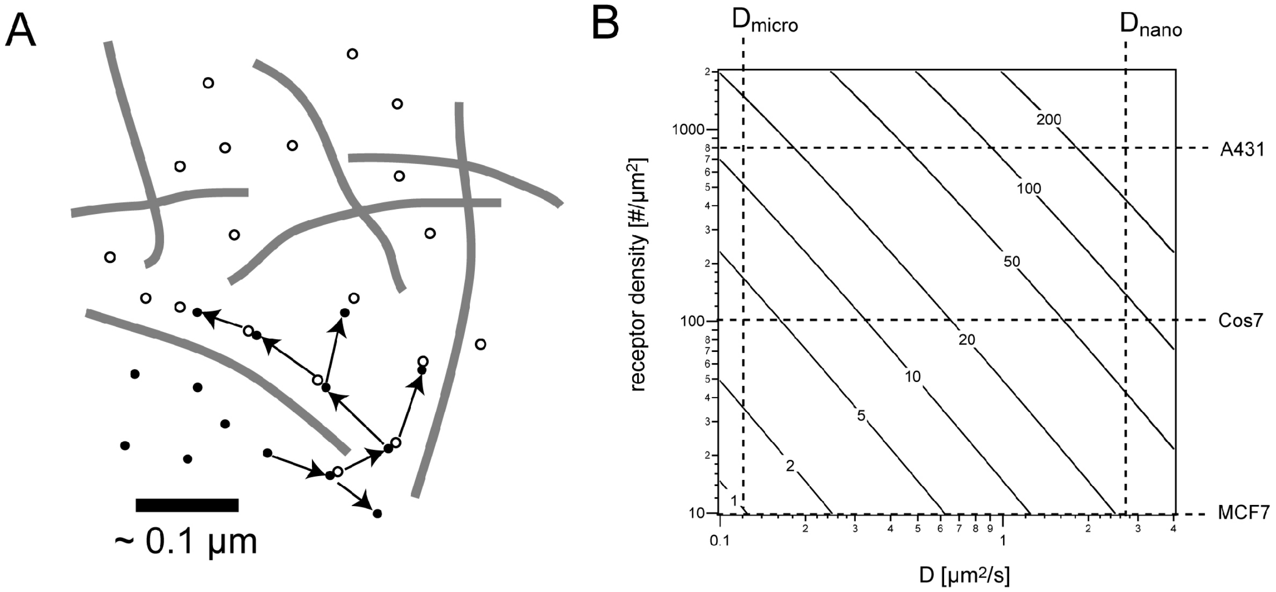

**Figure 5.3:** Lateral signal propagation in the membrane. A) Signal propagation in the presence of diffusion barriers. Activated receptors (filled circles) trans-autoactivate adjacent inactive receptor (open circles). The encounter of receptors is mediated by diffusive motion (arrows). B) Maximal speeds of phosphorylation propagation by trans-autoactivation assuming diffusion limited reaction kinetics. Contour lines give speeds in $\mu$m/s. Dashed horizontal lines indicate EGFR surface densities as determined in Appendix C. Dashed vertical lines indicate the diffusion coefficient of EGFR on the micrometer scale (section B) and on the nanometer scale (section 4.4).

riers. For instance, Fig. 5.3A depicts a scenario where local diffusion-reaction events could propagate a signal relatively fast "around" barriers and thereby develop a high speed even in the presence of barriers. A detailed analysis of the speeds that can be expected for lateral signal propagation in the plasma membrane will most likely require computer simulations of diffusion-reaction events in nonhomogeneous media (see for instance Castiglione et al. (2002)). 2D-TNIM data can provide realistic parameters that could serve as a basis for such studies. It is important to mention that although auto-phosphorylation enhances the kinase activity of many RTKs, there usually is residual (basal) kinase activity in the unphosphorylated state of the receptor. In the presence of basal kinase activity, sporadically activated receptors could trigger a phosphorylation wavefront. As such events would steadily occur, the cell would be always in the "activated state". To maintain a functional phosphorylation propagation mechanism in the presence of basal kinase activity, a counteracting mechanism is needed that makes the system robust against basal kinase activity, but still allows propagation of phosphorylation if a local stimulus overcomes a certain threshold. Possible mechanisms by which such a threshold could be generated in a physiological context are discussed by Ferrell and Xiong (2001) and Reynolds et al. (2003).

In conclusion, RTK trans-activation has the inherent potential to amplify and propagate a local stimulus with speeds of micrometers per second. As such propagation would take place within the first input layer of the signalling cascade, namely the receptor, it is a means to specifically amplify a local signal.

# 6. Conclusions

In this work, Thermal Noise Imaging Microscopy (TNIM) was developed for studying diffusion in heterogeneous submicrometer-scale environments. The development of TNIM was directed to facilitate ongoing research on the regulation of the lateral mobility of integral membrane proteins.

The ultimate goal of TNIM was to use the Brownian motion of individual proteins in order to "scan" the accessibility of their submicrometer-scale membrane environment. Initially, the key ideas underlying TNIM were validated in a series of experiments where the motion of a microsphere was studied in relatively rigid 3D environments. The motion of a microsphere was observed within a dense polymer network. Computing 3D histograms of the microsphere's positions revealed inaccessible volume elements, indicative of individual polymer filaments. As in all TNIM experiments, it was crucial that the Brownian motion of the particle was confined by the optical trap, because this ensured that volume elements were sufficiently sampled to obtain statistically significant information on their accessibility. This experiment demonstrated that it is indeed possible to employ the Brownian motion of a single particle to scan the accessibility of its submicrometer-scale environment, which is one key idea of TNIM. However, for understanding how proteins move in the membrane and how particles move through heterogeneous material in general, it is not only important to know the steric constraints to diffusion, but also how objects influence a particle's mobility over microscopic distances, e.g. owing to hydrodynamic coupling. To obtain such information with nanometer precision, a detector calibration scheme was developed that allowed the *in situ* detection of, and subsequent correction for, non-linearities in position signals obtained from laser light scattered by the microsphere. Using this calibration scheme it was possible to measure nanometer scale variations in the mobility of the microsphere in the vicinity of objects such as a solid glass surface or a soft cell surface. These experiments demonstrated that TNIM measurements provide simultaneous information on (i) steric constraints to diffusion and on (ii) variations of the particle's mobility. Importantly, these informations are obtained isotropically in three dimensions, with nanometer resolution, and in the vicinity of soft (biological) material. These results show the great promise for the general applicability of TNIM for studying fundamental hydrodynamics, which are e.g. important for diffusive transport in heterogeneous media such as the interior of a cell. In particular, the experiments on the microsphere have laid the foundations for TNIM studies on the lateral mobility of membrane-bound proteins.

As there is evidence that diffusion-mediated encounters of adjacent EGFRs can lead to their (ligand-independent) trans-autophosphorylation and thereby activation, it was considered of particular interest to employ TNIM for studying the mobility of EGFR. Specifically coupling EGFR to the optically trapped microsphere enabled the observation of the receptor's nanoscale motion in a defined submicrometer-scale membrane area. Analysing the receptor's motion, time series of images were obtained, where each image revealed which membrane areas were accessible to the diffusive motion of EGFR during a given time window. Experiments where the microsphere was coupled to a lipid anchored protein showed, on average, more accessible areas. These were important results as they showed that (i) the Brownian motion of individual proteins can be employed to obtain images of membrane accessibility on the submicrometer-scale and that (ii) the images obtained are specific for the protein that is used as a probe. The analysis of these images indicated that the local accessibility of the plasma membrane can vary strongly within tens of nanometers. Moreover, it was in many cases observed that the position and shape of the accessible membrane regions changed significantly within less than a second, consistent with the notion of a highly dynamic partitioning of proteins in the fluid plasma membrane. Lastly, evidence was presented that also spatial variations in the mobility of membrane proteins can be measured with few nanometer resolution. Information of this kind is crucial to distinguish between current models of membrane domain formation. For instance, the slowing of a protein's diffusion close to domain boundaries formed by actin-anchored transmembrane proteins has been theoretically proposed and can now be experimentally studied.

It is generally challenging to determine diffusion coefficients of membrane proteins on the nanometer scale, because techniques that have the necessary resolution require the use of relatively large marker particles that slow down the diffusion of the attached protein. The situation is further complicated by the fact that the bound marker particle is typically only a few nanometer above the plasma membrane and surface effects such as hydrodynamic coupling influence its mobility. Here, it was shown that TNIM allows measuring the mobility of the marker sphere at the plasma membrane directly before binding at the same distance as it has after binding. This makes it possible to correct for the slowing of the protein by the attached microsphere with high accuracy. In doing so, evidence was obtained that EGFR diffuses on the nanometer scale more than an order of a magnitude faster than on the micrometer-scale as determined using established FRAP technology. Remarkably, diffusion on the nanometer scale was comparable to what is measured for similar proteins in homogeneous model lipid bilayers.

These results suggest that the mobility of EGFR on the nanometer scale is dominated by the lipid bilayer structure of the plasma membrane, whereas constraints on the submicrometer scale hinder its diffusion on the micrometer scale. This could be a general property of the lateral structure of the plasma membrane as Fujiwara et al. (2002) and Murase et al. (2004), who used high-resolution SPT to track the motion of transferrin receptor and various lipids, also report fast diffusion on small length scales.

The strong length scale dependence of the effective diffusion constant of EGFR is of particular interest, because it implies that the rate at which receptors encounter each other by diffusion depends on their average distance and thereby on the surface density of EGFR in a given cell line. This is an effect that should be accounted for in models that aim to predict the kinetics of ligand induced EGFR dimerisation. Moreover, it also implies that the frequency of receptor encounters strongly rises at high receptor densities not only because there are more receptors, but also because receptors do interact on shorter length scales where mobility is less restricted. This is of biological interest as it is discussed if ligand independent EGFR autoactivation may overcome the ”house-keeping” activity of protein tyrosine phosphatase and thereby promote uncontrolled cell proliferation at overly high EGFR expression levels. In addition, evidence was presented that a sequence of diffusion-mediated trans-autoactivation events could spread EGFR activation with speeds of micrometers per second across the membrane, even in the presence of submicrometer-scale constraints to diffusion that hinder long range diffusion of receptors. This is interesting as there is experimental evidence for non-local phosphorylation responses of local EGFR stimulation that could be explained by phosphorylation propagation at such speeds.

In conclusion, it has been shown that the Brownian motion of a particle is an efficient means to scan microscopic volumes, if it is confined to a region of interest. The analysis of the particle’s position time trace provides simultaneous information on the local accessibility of the medium (”accessibility maps”) and on local variations in the particle’s mobility (”mobility maps”), on the nanometer scale. Such data will facilitate ongoing research on diffusive transport in heterogeneous media in general, and on the kinetics of diffusion-mediated reactions in the cellular plasma membrane, in particular.

# A. Simulating constrained diffusion

In this work, novel procedures for the evaluation of Brownian motion were developed (e.g. quantitative visualisation of two-dimensional TNIM data in section 4.2). To test these procedures it was important to have "clean data" (i.e. position time traces free of experimental noise or drift). Here, the simulation of Brownian position time traces by the Langevin equation (section 2.2.2) is described and an implementation is validated. The following is based on section 2.2. Quantities that have been defined there, are not necessarily described again.

### Integrated Langevin equation

Confined Brownian motion was simulated using the integrated form of the Langevin Equation (Equation (2.4)) according to Ermak and McCammon (1978):

$$\begin{aligned} r_i^{n+1} &= r_i^n + \frac{\delta t}{\gamma}\left(-k_i r_i^n + F_{thermal}^n\right) \\ F_{thermal}^n &= \sqrt{2\frac{k_B T \gamma}{\delta t}}\zeta(n) \end{aligned} \tag{A.1}$$

where $r_i^n$ is the particle position along $i \in \{x, y, z\}$ at time $t = n\delta t$. $\zeta(n)$ is a Gaussian random variable with zero mean and variance one[1]. This choice of the thermal force ensures a Gaussian and temporally uncorrelated stochastic force. Further, the chosen amplitude guarantees that the displacements are consistent with the Einstein-Stokes formula $D = k_B T/\gamma$.

### Algorithm validation

To simulate position times traces, an algorithm based on Equation (A.1) was implemented in Igor Pro 4.07 (Wavemetrics, Oregon, USA). In order to validate the implementation, two-dimensional confined Brownian motion of a sphere with radius $a = 125$ nm at $T = 293$ K in a medium with viscosity $\eta = 1 \cdot 10^{-3}$ Ns/m$^2$ was simulated for 4 s at $\delta t = 2.5$ $\mu$s, where

---

[1] The algorithm was implemented in Igor Pro (Wavemetrics). The function "gnoise(1)" was used to generate a random variable for each time step $n$.

$\gamma = 6\pi\eta a$. The force constants chosen were $k_x = 1.5$ $\mu$N/m and $k_y = 0.9$ $\mu$N/m. As expected (see section 2.2.4 and Fig. A.1A), the simulated positions were Boltzmann distributed:

$$\begin{aligned} n(x) &\propto \exp\left(-x^2/\sigma_x^2\right) && \text{(A.2)} \\ n(y) &\propto \exp\left(-y^2/\sigma_y^2\right) && \text{(A.3)} \end{aligned}$$

Fitting the position distributions of 5 independent simulation runs to Equation (A.2) and Equation (A.3) yielded $\sigma_x = 74.1 \pm 0.9$ nm and $\sigma_y = 97.2 \pm 1.5$ nm. The theoretical expectations are $\sigma_x = \sqrt{2k_BT/k_x} \approx 74$ nm and $\sigma_y = \sqrt{2k_BT/k_x} \approx 96$ nm (see section 2.2.4), given the above mentioned parameters that were used in the simulation. Thus, the equilibrium behaviour of the simulation is consistent with the theoretical expectation.

To check the dynamics, the mean square displacement of the position fluctuations was computed according to Equation (2.5). The theoretical expectation is (Equation (2.7)):

$$\begin{aligned} \mathrm{MSD_x}(\Delta t) &= \sigma_x^2\left(1 - \exp(-\Delta t/\tau_x)\right) && \text{(A.4)} \\ \mathrm{MSD_y}(\Delta t) &= \sigma_y^2\left(1 - \exp(-\Delta t/\tau_y)\right) && \text{(A.5)} \end{aligned}$$

The simulated data were well fit by Equation (A.4) and Equation (A.5) on all relevant timescales (see Fig. A.1B). Fitting 5 independent simulation runs yielded $\tau_x = 1.575 \pm 0.015$ ms, $\tau_y = 2.65 \pm 0.05$ ms, $\sigma_x = 74.4 \pm 0.5$ nm, and $\sigma_y = 96.0 \pm 0.8$ nm. The theoretical expectation for the position autocorrelation times are $\tau_x = k_x/(6\pi\eta a) \approx 1.57$ ms and $\tau_y = k_y/(6\pi\eta a) \approx 2.61$ ms (see section 2.2.3). The theoretical expectations for $\sigma_x$ and $\sigma_y$ are the same as mentioned above. Thus, both the plateau value and the position autocorrelation times as determined from the MSD are consistent with the theoretical expectations.

### Conclusions

An algorithm to simulate confined Brownian motion based on the Langevin equation was implemented and tested. Test runs in a 2D harmonic potential showed the theoretically expected Boltzmann distribution of positions. Furthermore, the theoretically expected MSD is reproduced on all relevant timescales (microseconds to seconds). Thus, the implemented algorithm could be routinely used to produce test data for the validation of the procedures that were developed in this work.

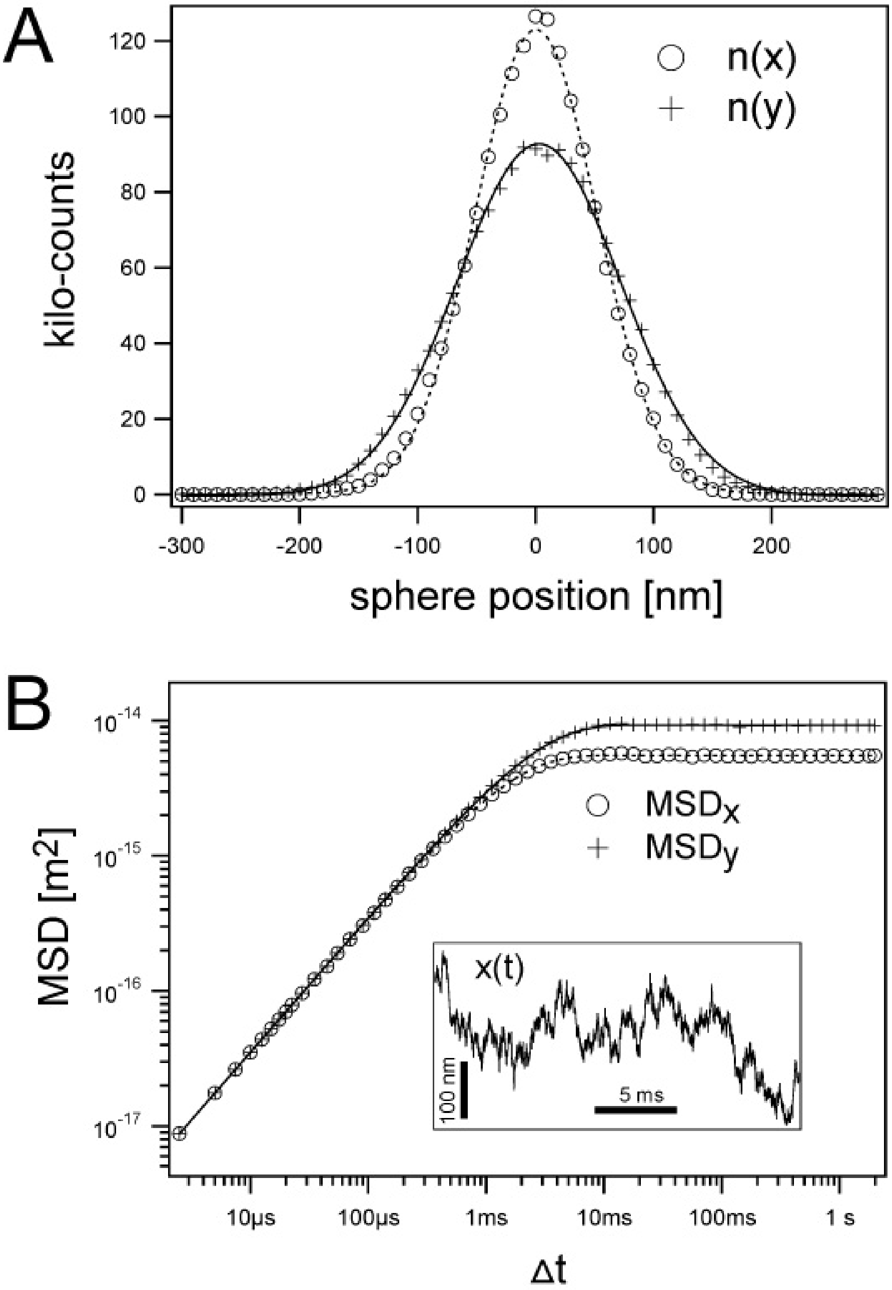

**Figure A.1:** Simulation of Brownian motion as confined in a harmonic potential. A) Position histograms. According to Boltzmann statistics the histograms are fit by Gaussian curves. The different shapes reflect the different force constants $k_x$=1.5 $\mu$N/m and $k_y$=0.9 $\mu$N/m. B) Mean square displacements (MSD). The MSD were fit to the theoretical expectations according to Equation (2.7). The inset shows part of a simulated position time trace. Details: Brownian position fluctuations were simulated according to Equation (A.1) for 4 seconds with a sampling time of 2.5 $\mu$s.

# B. Micrometer-scale diffusion of EGFR

In section 4.4, the nanometer scale mobility of GFP-EGFR was measured in the plasma membrane of Cos7 cells. Here, FRAP experiments are performed to determine the mobility of EGFR in the same cell line, but on the micrometer scale. FRAP is a well established technique where photobleaching is combined with time-lapse imaging to measure the diffusion of a population of molecules on the micrometer scale (see section 1.2 or Lippincott-Schwartz et al. (2003)).

### FRAP measurements

FRAP experiments were conducted on a standard confocal microscope (LSM510, Confocor, Zeiss). Cos7 cells expressing GFP-EGFR where imaged using the 488 nm line of an argon ion laser for excitation. The scan time for one image (128x128 pixels) was 98.3 ms. After acquisition of 5 images, both the 458 nm and 488 nm lines were scanned continuously for 2 s at maximal power across the whole image in $x$-direction (see Fig. B.1), while leaving the beam centered in $y$. This resulted in a photobleached stripe in the subsequent GFP image Fig. B.1B. The fraction of bleached molecules $b_i(x,y)$ in the $i^{th}$ image was computed as:

$$b_i(x,y) = 1 - \frac{f_i(x,y)}{n(x,y)}, \quad n(x,y) = \frac{1}{5}\sum_{i=1}^{5} f_i(x,y), \tag{B.1}$$

where $f_i(x,y)$ is the $i^{th}$ fluorescence image and $n(x,y)$ is the average fluorophore distribution before bleaching (see Fig. B.1D for an example). To obtain the mobility of the GFP-EGFR, the distribution of the bleached fraction along the $y$-direction was computed by averaging along the $x$-direction:

$$b(y,t_i) = \frac{1}{N}\sum_{x=-2\mu\text{m}}^{x=2\mu\text{m}} b_i(x,y), \tag{B.2}$$

where $N$ is the number of contributing pixels (in this case $N$=74). If the molecular motion is consistent with simple diffusion the fraction of bleached molecules, $b(y,t)$ should obey Fick's second law of diffusion:

$$\frac{\partial b(y,t)}{\partial t} = D\frac{\partial^2 b(y,t)}{\partial y^2} \tag{B.3}$$

This equation is solved by a time-dependent Gaussian curve:

$$b(y,t) = a(t)\exp(-y^2/w(t)^2) + \text{offset} \quad \text{with} \quad w(t)^2 = 4Dt + w_0^2 \tag{B.4}$$

Thus, given that the distribution of bleached molecules is Gaussian, the temporal broadening of the width $w(t)$ is a direct measure of the diffusion coefficient[1]. The example in Fig. B.1G shows that the distribution of bleached molecules is already Gaussian in the first frame after bleaching. Fitting $b(y, t_i)$ to Gaussian curves yields $w^2(t)$ (Fig. B.1H). In the example, $w^2(t)$ is well fit by a line, indicating simple diffusion. To check that simple diffusion is observed, the residuals of line fits to $w(t)^2$ were computed for 24 independent experiments (Fig. B.1I). The residuals do not indicate a significant deviation from a linear increase of $w(t)^2$ with time. Thus, motion of GFP-EGFR in the plasma membrane of a Cos7 cell is well described by simple diffusion on timescales longer than ca. 0.1 s and on length scales longer than ca. 0.3 $\mu$m. This permits the determination of a microscopic diffusion coefficient $D_{micro}$ from the slope of $w(t)^2$. In Cos7 cells at ≈22°C:

$$D_{micro}^{\mathrm{GFP-EGFR}} = (0.12 \pm 0.02)\ \mu\mathrm{m}^2/\mathrm{s}, \tag{B.5}$$

where the mean ± standard-deviation was calculated from the 24 independent measurements.

### Discussion

The first mobility measurements of EGFR were reported by Schlessinger et al. (1978). They added fluorescent EGF to 3T3 mouse fibroblasts and subsequently measured FRAP on the fluorescent EGF-EGFR complexes. In addition, several other groups have also measured EGFR mobility via fluorescent EGF:

---

[1] In principle, also the amplitude $a(t)$ could be used to measure the diffusion coefficient. However, because the bleached stripe is not infinitely long, there is a net flux of bleached molecules along the $x$-direction, i.e. out of the image. This makes the computation of $a(t)$ more difficult and it was therefore just used as a fit-parameter, however not evaluated.

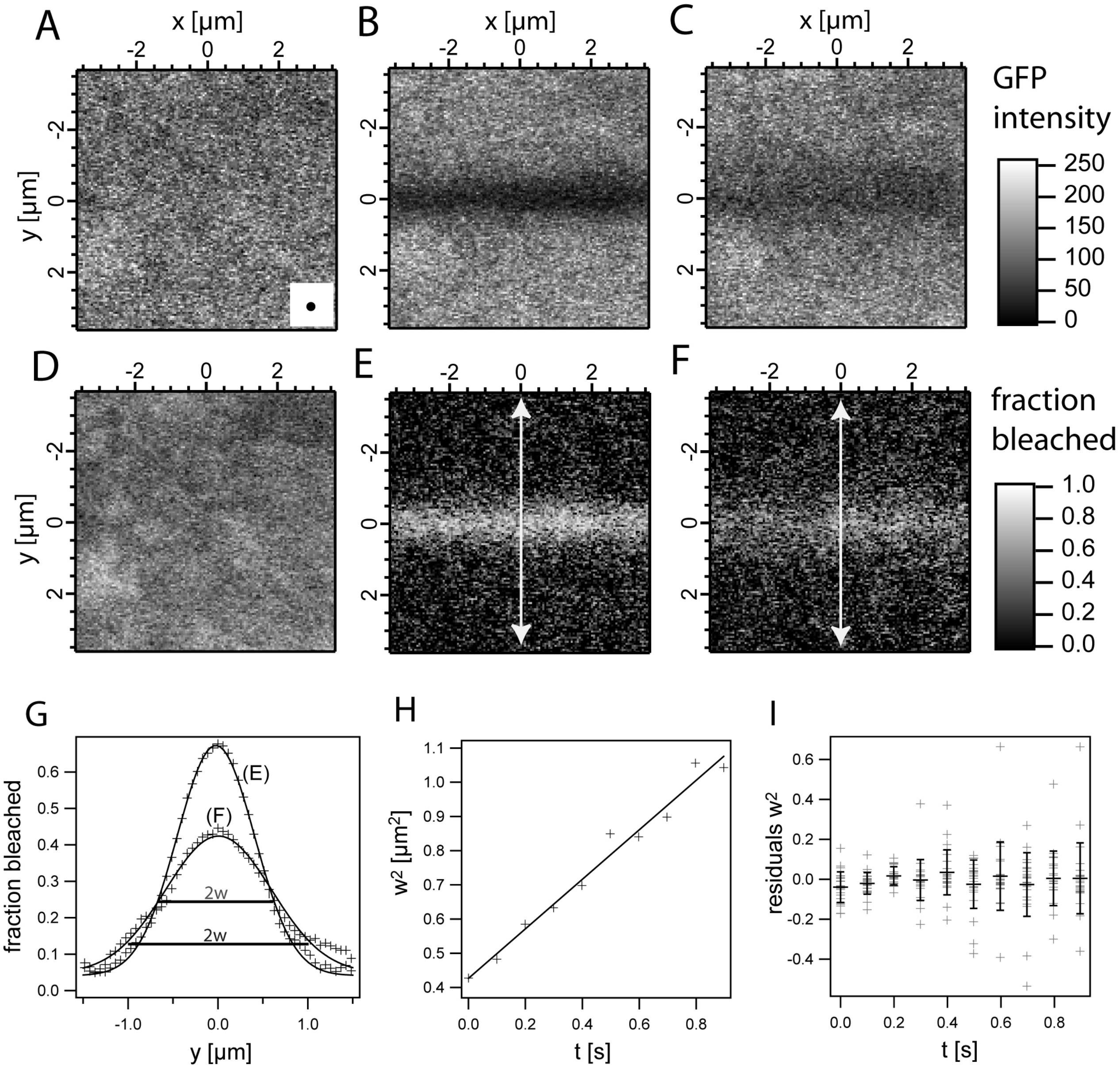

**Figure B.1:** Mobility of EGFR on the micrometer scale as measured by confocal FRAP. A)-D) Confocal fluorescence intensity images of GFP-EGFR in the plasma membrane of a COS7 cell. A) Before bleaching. The black circular area in the inset in the lower right corner depicts a region that would be probed in a 2D-TNIM experiment, i.e. $\approx$0.2 $\mu$m in diameter. B) First image after bleaching. C) Tenth image (983 ms) after bleaching. The acquisition of each frame took 98.3 ms. D) The average of five images that were acquired before bleaching. E)-F) Calculated fraction of bleached molecules in B and C according to Equation (B.1), taking the image in D for normalisation. The arrows indicate the direction along which the profiles in G were calculated. G) Crosses: average fraction of bleached molecules along the $y$-axis averaged over $1\mu$m$< x <1\mu$m in E and F. Lines: fits of Gaussian curves according to Equation (B.4). H) Crosses: squared width of the spatial distribution of bleached molecules as a function of time. Line: linear fit to deduce the diffusion coefficient. I) Grey crosses: residuals of the line-fits of 24 independent experiments. Black crosses: average and standard deviation of these residuals.

|  |  |  |
|---|---|---|
| Schlessinger et al. (1978) | , $D$=0.04 $\mu$m$^2$/s | , 3T3 cells |
| Zidovetzki et al. (1981) | , $D$=0.06 $\mu$m$^2$/s | , A431 cells |
| Hillman and Schlessinger (1982) | , $D$=0.08 $\mu$m$^2$/s | , A431 cells |
| Rees et al. (1984) | , $D$=0.02 $\mu$m$^2$/s | , A431 cells |
| Livneh et al. (1986) | , $D$=0.015 $\mu$m$^2$/s | , Cos cells |
| Benveniste et al. (1988) | , $D$=0.06–0.2 $\mu$m$^2$/s | , NIH-3T3 cells |

All diffusion coefficients obtained were slower than the $D = 0.12 \pm 0.02$ $\mu$m$^2$/s measured here for GFP-EGFR in Cos7 cells. The main difference between this work and the studies listed above is that here the EGFR was not stimulated by EGF[2]. EGF leads to membrane ruffling and EGFR internalisation within a few minutes (e.g. Yamazaki et al., 2002). An example of membrane ruffling after EGF stimulation in A431 cells is seen in Fig. C.1A. Membrane ruffling is a likely reason for the observed slower diffusion coefficients, since due to ruffling, the plasma membrane was probably no longer flat within the imaged object plane. Thus the motion observed with FRAP was most likely the projection of complex 3D motion on a 2D plane, leading to an underestimation of the apparent 2D diffusion coefficient.

Remarkably, the diffusion coefficient of EGFR that was obtained here (on length scales $\geq$0.3 $\mu$m) is more than 20-fold lower than on length scales $\leq$0.01 $\mu$m as measured in section 4.4. As both measurements were performed at a similar temperature ($\approx$22°C), using the same protein construct (GFP-EGFR) and the same line (Cos7 cells), it is concluded that diffusion of EGFR is hindered by constraints on the submicrometer scale such as observed in section 4.3.

---

[2] While this work was finished there was no study published that measured the mobility of unstimulated EGFR. Thus a direct comparison was not possible.

# C. Surface density of EGFR

For quantitative understanding of EGFR signal initiation, plasma membrane surface density of EGFR is an important parameter. For instance, it determines the frequency of diffusive encounters of monomeric EGFR. This encounter frequency determines the timescale of ligand induced dimerisation as well as ligand independent trans-phosphorylation events. Further, EGFR plasma membrane density determines the average distance between individual receptors and therefore determines biologically relevant length-scales in the plasma membrane.

The plasma membrane density of endogenous EGFR was measured in Cos7 cells, which is the cell line of choice for experiments on EGFR mobility (chapter 4 and chapter B). There is no established method to quantitatively measure densities of endogenous plasma membrane molecules. Here, EGFR was stained by fluorescent EGF to quantify relative densities in cells of different cell lines. To calculate the absolute number of molecules per area, two independent approaches for calibrating EGF-Cy3 fluorescence were employed. The absolute plasma membrane density of EGFR-GFP in MCF7 cells was determined by Fluorescence Correlation Spectroscopy (FCS). Furthermore, the EGF-Cy3 fluorescence on A431 cells, for which the approximate total number of EGFR molecules per cell is known, was used as a calibration standard. It shall be noted that it was not intended to perform high precision measurements but rather to obtain the order of magnitude of EGFR plasma membrane density.

### Experiments and results

Cells were incubated with about 100 ng/ml Cy3-EGF and left for 5 min at room temperature to permit binding to cell surface EGFR. Subsequently, unbound Cy3-EGF was removed and cells were fixed with para-formaldehyde to prevent further endocytosis of activated Cy3-EGF EGFR complexes. Such internalisation would diminish the Cy3-EGF intensity at the plasma membrane and consequently lead to an underestimation of EGFR plasma membrane density. Because both Cy3-EGF concentration in the medium and incubation time were identical in all experiments, the probability that individual EGFR bound a Cy3-EGF should be identical as well. Consequently, the average EGFR plasma membrane density should be proportional to the average intensity of Cy3-EGF at the plasma membrane as determined by confocal microscopy (Confocor, LSM-510, Zeiss). The distribution of Cy3-EGF intensities in Fig. C.1 shows that endogenous EGFR densities vary between individual cells and even more between cell lines (up to 100 fold). To obtain the absolute surface density of EGFR in Cos7 cells, A431 cells were used as a calibration standard. A431 cells have particularly high endogenous EGFR expression levels, which are therefore relatively easy to detect in various assays. According to Wiley (1988) the average total number of receptors within one A431 cell is roughly $2{\cdot}10^6$ as measured by an assay using radio-active EGF. According to electron microscopy studies by Haigler et al. (1979), the surface area of a A431 cells is ca. 2800 $\mu$m$^2$. Taken together this yields a receptor density of $[R]_{\mathrm{A431}} \approx 7 \cdot 10^2\ \mu\mathrm{m}^{-2}$. Comparing the average Cy3-EGF intensity on A431 cells to $[R]_{A431}$ yields that 1 a.u. Cy3 intensity corresponds to ca. 70 receptors/$\mu$m$^2$ (see Fig. C.1B). To check this value, the Cy3-EGF intensity was calibrated by another method. FCS experiments were performed on MCF7 cells expressing EGFR-GFP (not shown[1]). The lateral radius ($1/e^2$) of the excitation volume was about $r_0$=0.18 $\mu$m at 488 nm excitation. The number of the EGFR-GFP molecules that were at one time within the excitation volume was on average ca. $3{\cdot}10^1$ molecules. This yields a EGFR-GFP surface density of $[R]_{\mathrm{FCS}} \approx 3 \cdot 10^1/(\pi r_0^2) \approx 3 \cdot 10^2\ \mu\mathrm{m}^{-2}$. Comparing the average receptor density of EGFR-GFP in MCF7 cells ($[R]_{\mathrm{FCS}}$) to the average Cy3-EGF intensities yields that 1 a.u. Cy3-EGF intensity corresponds to ca. 85 receptors/$\mu$m$^2$ (see Fig. C.1B) . Thus, the "FCS calibration" corroborates the "A431 calibration", which indicated that 1 a.u. Cy3-EGF intensity corresponds to ca. 70 receptors/$\mu$m$^2$. Considering the completely different approaches to determine the calibration factor, the coincidence it remarkable. For the conclusions it was assumed that 1 a.u. Cy3-EGF intensity corresponds to ca. 80 receptors/$\mu$m$^2$.

### Conclusions

The surface density of endogenous EGFR in Cos7 cells is on the order of $1{\cdot}10^2/\mu\mathrm{m}^2$. EGFR density in wild type MCF7 cells is at least 10-fold lower than in Cos7 cells. This is consistent with findings of other groups reporting little or no detectable EGFR in this cell line (Larsen et al., 1999; DeFazio et al., 2000). The average density of EGFR in the plasma membrane of A431 cells is ca. $8{\cdot}10^2/\mu\mathrm{m}^2$.

---

[1] For details on FCS technology see e.g. Bacia and Schwille, 2003.

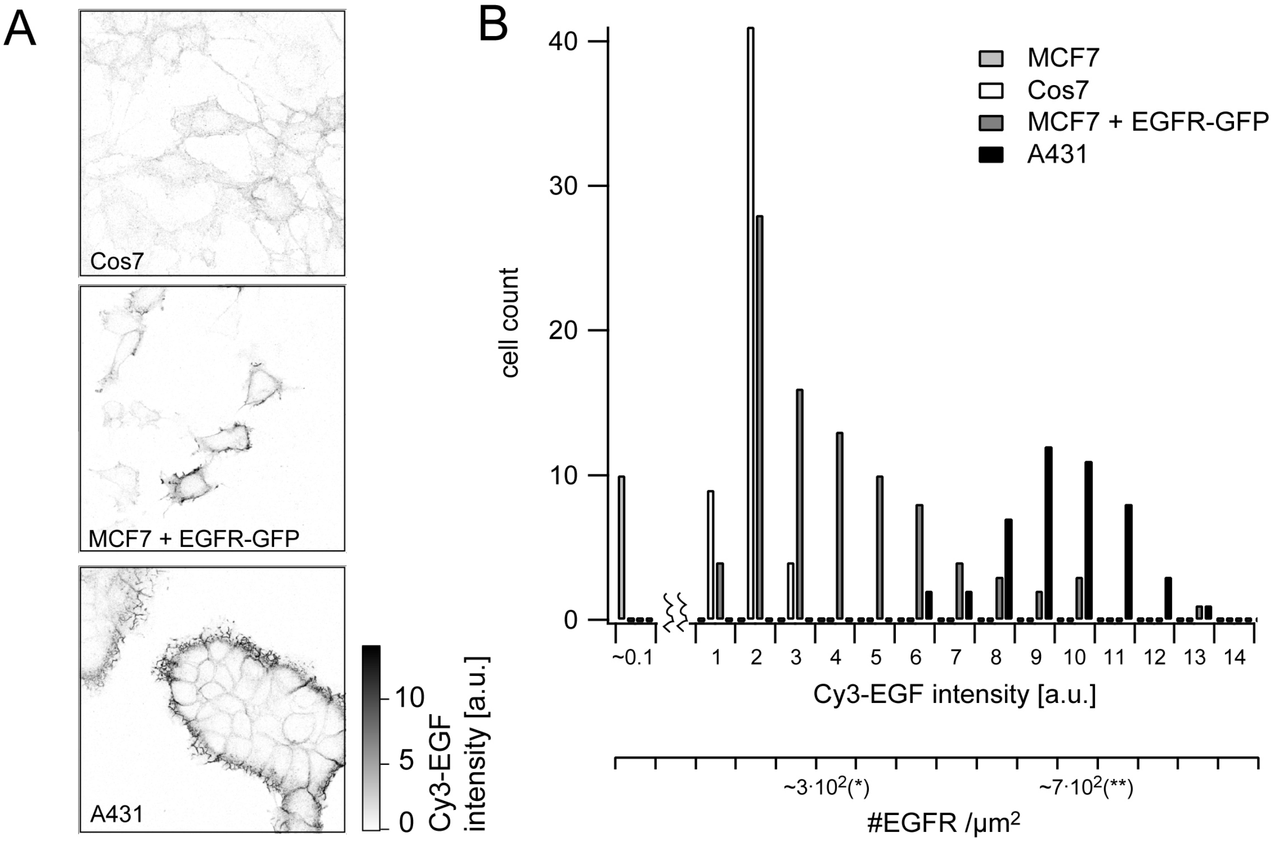

**Figure C.1:** EGFR plasma membrane density. A) Confocal fluorescence images of cells incubated for 5 min with Cy3-EGF. A431 cells grow in colonies thereby hampering Cy3-EGF binding at cell-cell contacts. B) Distribution of plasma membrane Cy3-EGF intensities in individual cells within different cell lines. (*) The Cy3-EGF intensity is compared to the average surface density of EGFR-GFP in MCF7 cells, determined by FCS (MCF7 cells were transfected with EGFR-GFP encoding cDNA). (**) The Cy3-EGF intensity is compared to the average surface density of EGFR in A431 cells (see text).

# D. Molecular biology methods

## Reagents

**biotinylated GFP-antibody:** biotin conjugated monoclonal anti-GFP antibody (600-306-215, Rockland, Gilbertsville, USA); kept as 25x glycerol stock at -20°C; for usage diluted to 100 nM.

**streptavidin-Alexa633:** streptavidin conjugated to Alexa Fluor 633 (633/647) (S21375, Molecular Probes, Leiden, The Netherlands); kept as 100x glycerol-stock at -20°C; for usage diluted to 100 nM.

**250 nm streptavidin spheres:** yellow/green fluorescent (470/505) streptavidin coated polystyrene microspheres with a mean diameter of 250 nm (L-6905, SIGMA, Saint Louis, Missouri, USA)

**250 nm red fluorescent streptavidin spheres:** red fluorescent (575/610) streptavidin coated polystyrene microspheres with a mean diameter of 250 nm (L-6530, SIGMA, Saint Louis, Missouri, USA)

**IM/BSA:** low bicarbonate Dulbecco's modified Eagle's medium (DMEM) without phenol red supplemented with 25 mM HEPES buffer and 0.2% bovine serum albumin (BSA) to block unspecific interactions.

## Protein constructs

**GFP-EGFR:** Green fluorescent protein as the ectodomain connected to epidermal growth factor receptor. The construct was produced by Martin Offterdinger, EMBL Heidelberg.

**GFP-GL-GPI:** Green fluorescent protein as the ectodomain connected to a GPI-anchor. The construct was a donated by Patrick Keller, MPI-CBG Dresden. For details see Pralle et al. (2000).

## Cell Culture and transfection

Cells were routinely maintained in Dulbecco's modified Eagle's medium (DMEM) supplemented with 10% foetal calf serum. Two days before an experiment cells were transferred to glass coverslips and left for one day. Subsequently, transient expression of proteins was induced by transfecting cells with plasmid DNA using the Fugene reagent (Roche, Basel, Switzerland). Cells were allowed to express the protein for one day. For microscopy, DMEM was replaced by the "imaging medium" IM/BSA (s.a.).

## Incubation of cells with biotinylated GFP antibody

To prepare specific binding of streptavidin beads (or streptavidin-Alexa633) to cells expressing a GFP coupled membrane molecule, cells were incubated for 10 min at 20° C with biotinylated GFP antibody that has been dissolved at 100 nM in IM/BSA. To remove unbound antibody, cells were washed extensively with IM/BSA.

## Preparation of agar polymer for 3D TNIM

Agar polymer was prepared at a concentration of 0.25 wt/vol by dissolving agar powder (Bacto-Agar, Difco) in bidistilled water and heating it at 90-100 °C for half an hour. The gel was then stored in a refrigerator at 4 °C for later use. Prior to an experiment, the agar gel was boiled in a microwave oven for 30 s. This ensured that the agar was completely in the fluid phase. Latex beads (Fluospheres, L-5242, Molecular Probes) with a nominal diameter of 216 nm were added to the fluid at an approximate concentration of about one bead per 20x20x20 $\mu m^3$. This low concentration was used to avoid optical trapping of multiple beads. The fluid was immediately filled into the sample chamber. The agar gel solidifies within minutes at room temperature.

## Immobilisation of microspheres on glass surface

Microsphere were dissolved in PBS and put onto an uncoated coverslip for adsorption onto the glass surface. After 10 minutes the coverslip was washed with water and dried for 30 minutes at 50 °C to increase the binding of the spheres. After mounting the coverslip in the sample chamber, it was filled with PBS for the experiment.

# Bibliography

G. Adam and M. Delbrück. *Reduction of dimensionality in biological diffusion processes.* W.H. Freeeman, San Francisco, 1968.

P. S. Agutter. Intracellular structure and nucleocytoplasmic transport. *Int. Rev. Cytol.*, 162B: 183–224, 1995.

B. Alberts, A. Johnson, J. Lewis, M. Raff, K. Roberts, and P. Walter. *Molecular biology of the cell. 4th edn.* Garland Science, New York, 2002.

P. F. Almeida, W. L. Vaz, and T. E. Thompson. Lateral diffusion and percolation in two-phase, two-component lipid bilayers. topology of the solid-phase domains in-plane and across the lipid bilayer. *Biochemistry*, 31:7198–7210, 1992.

P. F. F. Almeida and W. L. C. Vaz. *Lateral diffusion in membranes*, volume 1. Elsevier, 1995.

R. Anderson and K. Jacobson. A role for lipid shells in targeting proteins to caveolae, rafts and other lipid domains. *Science*, 296:1821–1825, 2002.

A. Ashkin, J. M. Dziedzic, J. E. Bjorkholm, and S. Chu. Observation of a single-beam gradient-force optical trap for dielectric particles. *Opt. Lett.*, 11:288–290, 1986.

D. Axelrod, D. E. Koppel, J. Schlessinger, E. Elson, and W. W. Webb. Mobility measurement by analysis of fluorescence photobleaching recovery kinetics. *Biophys. J.*, 16(9):1055–1069, 1976.

K. Bacia and P. Schwille. A dynamic view of cellular processes by in vivo fluorescence auto- and cross-correlation spectroscopy. *Methods*, 29:74–85, 2003.

A. Bakardjieva, H. J. Galla, and E. J. Helmreich. Modulation of the beta-receptor adenylate cyclase interactions in cultured Chang liver cells by phospholipid enrichment. *Biochemistry*, 18(14):3016–3023, 1979.

L. Barak and W. Webb. Diffusion of low density lipoprotein-receptor complex on human fibroblasts. *J. Cell Biol.*, 95:846–852, 1982.

L. S. Barak and W. W. Webb. Fluorescent low density lipoprotein for observation of dynamics of individual receptor complexes on cultured human fibroblasts. *J. Cell Biol.*, 90(3):595–604, 1981.

R. Barziv, A. Meller, T. Tlusty, E. Moses, J. Stavans, and S. Safran. Localized dynamic light scattering: Probing single particle dynamics at the nanoscale. *Phys. Rev. Lett.*, 78:154–157, 1997.

M. Benveniste, E. Livneh, J. Schlessinger, and Z. Kam. Overexpression of epidermal growth factor receptor in NIH-3T3-transfected cells slows its lateral diffusion and rate of endocytosis. *J. Cell Biol.*, 106(6):1903–1909, 1988.

H. Berg and E. Purcell. Physics of chemoreception. *Biophys. J.*, 20:193–219, 1977.

P. Bertics and G. Gill. Self-phosphorylation enhances the protein-tyrosine kinase activity of the epidermal growth factor receptor. *J. Biol. Chem.*, 260:14642–14647, 1985.

M. Bevan and D. Prieve. Hindered diffusion of colloidal particles very near to a wall: revisited. *J. Chem. Phys.*, 113:1228–1236, 2000.

G. Binnig, C. F. Quate, and C. Gerber. Atomic force microscope. *Phys. Rev. Lett.*, 56:930–933, 1986.

G. Binnig, H. Rohrer, C. Gerber, and E. Weibel. Surface studies by scanning tunneling microscopy. *Phys. Rev. Lett.*, 49:57–61, 1982.

J. Boileau and G. W. Slater. An exactly solvable Ogston model of gel electrophoresis. VI. Towards a theory for macromolecules. *Electrophoresis*, 22:673–683, 2001.

A. J. Borgdorff and D. Choquet. Regulation of AMPA receptor lateral movements. *Nature*, 417(6889):649–653, 2002.

G. E. P. Box and G. M. Jenkins. *Time Series Analysis: Forecasting and Control*. Holden Day, 1970.

H. Brenner. The slow motion of a sphere through a viscous fluid towards a plane surface. *J. Chem. Phys.*, 16:242–251, 1961.

F. A. Brightman and D. A. Fell. Differential feedback regulation of the MAPK cascade underlies the quantitative differences in EGF and NGF signalling in PC12 cells. *FEBS Lett.*, 482(3):169–174, 2000.

D. Broday. Motion of nanobeads proximate to plasma membranes during single particle tracking. *Bull. Math. Biol.*, 64:531–563, 2002.

F. L. H. Brown. Regulation of protein mobility via thermal membrane undulations. *Biophys. J.*, 84:842–853, 2003.

F. Castiglione, M. Bernaschi, S. Succi, R. Heinrich, and M. W. Kirschner. Intracellular signal propagation in a two-dimensional autocatalytic reaction model. *Phys. Rev. E Stat. Nonlin. Soft Matter Phys.*, 66:031905, 2002.

P. Celliers and J. Conia. Measurement of localized heating in the focus of an optical trap. *Appl. Optics*, 39:3396–3407, 2000.

G. Cevc. Lipid vesicles and other colloids as drug carriers on the skin. *Adv. Drug Deliv. Rev.*, 56:675–711, 2004.

S. Chandrasekhar. Stochastic problems in physics and astronomy. *Rev. of mod. Physics*, 15: 1–89, 1943.

R. J. Cherry, P. R. Smith, I. E. Morrison, and N. Fernandez. Mobility of cell surface receptors: a re-evaluation. *FEBS Lett.*, 430:88–91, 1998.

S. Cowley, H. Paterson, P. Kemp, and C. J. Marshall. Activation of MAP kinase kinase is necessary and sufficient for PC12 differentiation and for transformation of NIH 3T3 cells. *Cell*, 77(6):841–852, 1994.

M. Dahan, S. Levi, C. Luccardini, P. Rostaing, B. Riveau, and A. Triller. Diffusion dynamics of glycine receptors revealed by single-quantum dot tracking. *Science*, 302(5644):442–445, 2003.

F. Daumas, N. Destainville, C. Millot, A. Lopez, D. Dean, and L. Salome. Confined diffusion without fences of a g-protein-coupled receptor as revealed by single particle tracking. *Biophys. J.*, 84:356–366, 2003.

M. de Brabander, G. Geuens, R. Nuydens, M. Moeremans, and J. D. Mey. Probing microtubule-dependent intracellular motility with nanometre particle video ultramicroscopy (nanovid ultramicroscopy). *Cytobios*, 43:273–283, 1985.

M. de Brabander, R. Nuydens, A. Ishihara, B. Holifield, K. Jacobson, and H. Geerts. Lateral diffusion and retrograde movements of individual cell surface components on single motile cells observed with Nanovid microscopy. *J. Cell Biol.*, 112(1):111–124, 1991.

J. Dean. *Lange's Handbook of Chemistry.* McGraw-Hill Book Company, New York, 1985.

A. DeFazio, Y.-E. Chiew, R. Sini, P. Janes, and R. Sutherland. Expression of c-erbb receptors, heregulin and oestrogen receptor in human breast cell lines. *Int. J. Cancer*, 87:487–498, 2000.

M. Edidin. Patches, posts and fences: proteins and plasma membrane domains. *Trends in Cell Biol.*, 2:376–380, 1992.

M. Edidin. Membrane cholesterol, protein phosphorylation, and lipid rafts. *Sci. STKE*, 2001 (67):PE1, 2001a.

M. Edidin. Shrinking patches and slippery rafts: scales of domains in the plasma membrane. *Trends Cell Biol.*, 11:492–496, 2001b.

M. Edidin. Lipids on the frontier: a century of cell-membrane bilayers. *Nat. Rev. Mol. Cell Biol.*, 4(5):414–418, 2003.

M. Edidin, S. C. Kuo, and M. P. Sheetz. Lateral movements of membrane glycoproteins restricted by dynamic cytoplasmic barriers. *Science*, 254:1379–1382, 1991.

M. Edidin, M. C. Zuniga, and M. P. Sheetz. Truncation mutants define and locate cytoplasmic barriers to lateral mobility of membrane glycoproteins. *Proc. Natl. Acad. Sci.*, 91(8):3378–3382, 1994.

A. Einstein. On the motion of small particles suspended in liquids at rest required by the molecular-kinetic theory of heat. *Annalen der Physik*, 17:549–560, 1905.

L. Ellis, E. Clauser, D. O. Morgan, M. Edery, R. A. Roth, and W. J. Rutter. Replacement of insulin receptor tyrosine residues 1162 and 1163 compromises insulin-stimulated kinase activity and uptake of 2-deoxyglucose. *Cell*, 45(5):721–732, 1986.

D. Ermak and J. McCammon. Brownian dynamics with hydrodynamic interactions. *J. Chem. Phys.*, 69:1352–1360, 1978.

S. Eskandari, E. Wright, M. Kreman, D. Starace, and G. Zampighi. Structural analysis of cloned plasma membrane proteins by freezefracture electron microscopy. *Proc. Natl. Acad. Sci.*, 95:11235–11240, 1998.

W. J. Fantl, J. A. Escobedo, and L. T. Williams. Mutations of the platelet-derived growth factor receptor that cause a loss of ligand-induced conformational change, subtle changes in kinase activity, and impaired ability to stimulate DNA synthesis. *Mol. Cell Biol.*, 9(10): 4473–4478, 1989.

J. Ferrell and W. Xiong. Bistability in cell signaling: How to make continuous processes discontinuous, and reversible processes irreversible. *Chaos*, 11(1):227–236, 2001.

P. Fife and J. B. McLeod. The approach of solutions of nonlinear diffusion equation to travelling front solutions. *Arch. Rational Mech. Anal.*, 65:335–361, 1977.

E. H. Fischer, H. Charbonneau, and N. K. Tonks. Protein tyrosine phosphatases: a diverse family of intracellular and transmembrane enzymes. *Science*, 253(5018):401–406, 1991.

R. Fisher. The wave of advance of advantageous genes. *Ann. Eugenics*, 7:353–369, 1937.

E.-L. Florin. *Nanomechanik, Adhäsion und Erkennung*. PhD thesis, Fakultät für Physik der technischen Universität München, 1994.

E. L. Florin, V. T. Moy, and H. E. Gaub. Adhesion forces between individual ligand-receptor pairs. *Science*, 264:415–417, 1994.

E.-L. Florin, A. Pralle, J. Hörber, and E. Stelzer. Photonic force microscope based on optical tweezers and two-photon excitation for biological applications. *J. Struct. Biol.*, 119:202–211, 1997.

E.-L. Florin, A. Pralle, E. Stelzer, and J. Hörber. Photonic force microscope calibration by thermal noise analysis. *Appl. Phys. A*, 66:75–78, 1998.

T. Fujiwara, K. Ritchie, H. Murakoshi, K. Jacobson, and A. Kusumi. Phospholipids undergo hop diffusion in compartmentalized cell membrane. *J. Cell Biol.*, 157(6):1071–1081, 2002.

F. Galbiati, B. Razani, and M. Lisanti. Emerging themes in lipid rafts and caveolae. *Cell*, 106:403–411, 2001.

T. P. J. Garrett, N. M. McKern, M. Lou, T. C. Elleman, T. E. Adams, G. O. Lovrecz, H.-J. Zhu, F. Walker, M. J. Frenkel, P. A. Hoyne, R. N. Jorissen, E. C. Nice, A. W. Burgess, and C. W. Ward. Crystal structure of a truncated epidermal growth factor receptor extracellular domain bound to transforming growth factor alpha. *Cell*, 110(6):763–773, 2002.

L. Ghislain and W. Webb. Scanning force microscope using an optical trap. *Opt. Lett.*, 18: 1678–1683, 1993.

F. Gittes and C. Schmidt. Signals and noise in micromechanical measurements. *Methods Cell Biol.*, 55:129–156, 1997.

F. Gittes and C. Schmidt. Interference model for back focal plane displacement detection in optical tweezers. *Opt. Lett.*, 23:7–9, 1998.

A. Goldman, R. Cox, and H. Brenner. Slow viscous motion of a sphere parallel to a plane wall - i motion through a quiescent fluid. *Chem. Eng. Sci.*, 22:637, 1967.

B. Goldstein, C. Wofsy, and G. Bell. Interactions of low density lipoprotein receptors with coated pits on human fibroblasts: estimate of the forward rate constant and comparison with the diffusion limit. *Proc. Natl. Acad. Sci.*, 78(9):5695–5698, 1981.

W. C. Gorospe and P. M. Conn. Membrane fluidity regulates development of gonadotrope desensitization to GnRH. *Mol. Cell Endocrinol.*, 53(1-2):131–140, 1987.

D. Grier. A revolution in optical manipulation. *Nature*, 424:810–816, 2003.

C. L. Grimellec, E. Lesniewska, M. Giocondi, E. Finot, V. Vie, and J. Goudonnet. Imaging of the surface of living cells by low-force contact-mode atomic force microscopy. *Biophys. J.*, 75:695–703, 1998.

L. C. Groenen, F. Walker, A. W. Burgess, and H. R. Treutlein. A model for the activation of the epidermal growth factor receptor kinase involvement of an asymmetric dimer? *Biochemistry*, 36(13):3826–3836, 1997.

W. J. Gullick. Prevalence of aberrant expression of the epidermal growth factor receptor in human cancers. *Br. Med. Bull.*, 47(1):87–98, 1991.

H. T. Haigler, J. A. McKanna, and S. Cohen. Direct visualization of the binding and internalization of a ferritin conjugate of epidermal growth factor in human carcinoma cells A-431. *J. Cell Biol.*, 81:382–395, 1979.

E. Hanski, G. Rimon, and A. Levitzki. Adenylate cyclase activation by the beta-adrenergic receptors as a diffusion-controlled process. *Biochemistry*, 18(5):846–853, 1979.

J. Happel and H. Brenner. *Low Reynolds Number Hydrodynamics*. Prentice Hall, 1965.

D. Heermann. Computational Physics. *Lecture at the Faculty of Physics at Heidelberg University*, 2000.

R. Heinrich, B. G. Neel, and T. A. Rapoport. Mathematical models of protein kinase signal transduction. *Mol Cell*, 9(5):957–970, 2002.

B. S. Hendriks, L. K. Opresko, H. S. Wiley, and D. Lauffenburger. Quantitative analysis of HER2-mediated effects on HER2 and epidermal growth factor receptor endocytosis: distribution of homo- and heterodimers depends on relative HER2 levels. *J. Biol. Chem.*, 278 (26):23343–23351, 2003.

G. M. Hillman and J. Schlessinger. Lateral diffusion of epidermal growth factor complexed to its surface receptors does not account for the thermal sensitivity of patch formation and endocytosis. *Biochemistry*, 21(7):1667–1672, 1982.

W. Hong and A. Ullrich. The role of EGFR in solid tumors and implications for therapy. *Oncol. Biother.*, 1:1–29, 2000.

C. Y. Hsu, D. R. Hurwitz, M. Mervic, and A. Zilberstein. Autophosphorylation of the intracellular domain of the epidermal growth factor receptor results in different effects on its tyrosine kinase activity with various peptide substrates. Phosphorylation of peptides representing Tyr(P) sites of phospholipase C-gamma. *J. Biol. Chem.*, 266(1):603–608, 1991.

S. R. Hubbard, M. Mohammadi, and J. Schlessinger. Autoregulatory mechanisms in protein-tyrosine kinases. *J. Biol. Chem.*, 273(20):11987–11990, 1998.

S. R. Hubbard and J. H. Till. Protein tyrosine kinase structure and function. *Annu Rev Biochem*, 69:373–398, 2000.

E. Hur, Y. Park, B. Lee, I. Jang, H. Kim, T. Kim, P. Suh, S. Ryu, and K. Kim. Sensitization of epidermal growth factor-induced signaling by bradykinin is mediated by c-src. implications for a role of lipid microdomains. *J. Biol. Chem.*, 279:5852–5860, 2004.

W. Häberle, J. H. K. Hörber, F. Ohnesorge, D. P. Smith, and G. Binnig. In situ investigations of single living cells infected by viruses. *Ultramicroscopy*, 42:1161–1167, 1992.

J. K. H. Hörber and M. J. Miles. Scanning probe evolution in biology. *Science*, 302:1002–1005, 2003.

J. N. Israelachvilli. *Intermolecular and Surface Forces.* Academy Press, New York, 1991.

K. Jacobson and C. Dietrich. Looking at lipid rafts? *Trends Cell Biol.*, 9:87–91, 1999.

D. A. Jans. The mobile receptor hypothesis revisited: a mechanistic role for hormone receptor lateral mobility in signal transduction. *Biochim. Biophys. Acta*, 1113(3-4):271–276, 1992.

S. Jeney, E. H. K. Stelzer, H. Grubmuller, and E.-L. Florin. Mechanical properties of single motor molecules studied by three-dimensional thermal force probing in optical tweezers. *Chemphyschem*, 5(8):1150–1158, 2004.

A. Jeremic, M. Kelly, S.-J. Cho, M. H. Stromer, and B. P. Jena. Reconstituted fusion pore. *Biophys. J.*, 85(3):2035–2043, 2003.

F. K, G. E, and Z. R. Noise-induced bistability in a Monte Carlo surface-reaction model. *Phys. Rev. Lett.*, 63(14):1527–1530, 1989.

J. Keizer. Theory of rapid bimolecular reactions in solution and membranes. *Accounts Chem. Res.*, 18:235–241, 1985.

J. Keizer. Diffusion effects on rapid bimolecular chemical-reactions. *Chemical Reviews*, 87: 167–180, 1987.

S. J. Kempiak, S.-C. Yip, J. M. Backer, and J. E. Segall. Local signaling by the EGF receptor. *J. Cell Biol.*, 162(5):781–787, 2003.

R. L. Kendall, R. Z. Rutledge, X. Mao, A. J. Tebben, R. W. Hungate, and K. A. Thomas. Vascular endothelial growth factor receptor KDR tyrosine kinase activity is increased by autophosphorylation of two activation loop tyrosine residues. *J. Biol. Chem.*, 274(10):6453–6460, 1999.

A. K. Kenworthy, B. J. Nichols, C. L. Remmert, G. M. Hendrix, M. Kumar, J. Zimmerberg, and J. Lippincott-Schwartz. Dynamics of putative raft-associated proteins at the cell surface. *J. Cell Biol.*, 165(5):735–746, 2004.

B. N. Kholodenko. Four-dimensional organization of protein kinase signaling cascades: the roles of diffusion, endocytosis and molecular motors. *J Exp Biol*, 206(Pt 12):2073–2082, 2003.

B. N. Kholodenko, O. V. Demin, G. Moehren, and J. B. Hoek. Quantification of short term signaling by the epidermal growth factor receptor. *J. Biol. Chem.*, 274(42):30169–30181, 1999.

A. Kolmogoroff, I. Petrosky, and N. Piscounoff. Etudes de l'equation aved croissance de la quantit´e de mati‘ere et son application a un probleme biologique. *Moscow Univ. Bull. Math.*, 1:1–25, 1937.

K. König, H. Liang, M. Berns, and B. Tromberg. Cell damage in near infrared multimode optical traps due to multi-photon absorption. *Optics Letters*, 21:1090–1092, 1996.

R. Kubo. The fluctuation-dissipation theorem. *Rep. Prog. Phys.*, 29:255–284, 1966.

S. Kulin, R. Kishore, J. B. Hubbard, and K. Helmerson. Real-time measurement of spontaneous antigen-antibody dissociation. *Biophys. J.*, 83:1965–1973, 2002.

A. Kusumi and Y. Sako. Cell surface organization by the membrane skeleton. *Curr. Opin. Cell Biol.*, 8:566–574, 1996.

A. Kusumi, Y. Sako, and M. Yamamoto. Confined lateral diffusion of membrane receptors as studied by single particle tracking (nanovid microscopy). effects of calcium-induced differentiation in cultured epithelial cells. *Biophys. J.*, 65:2021–2040, 1993.

J. Kwik, S. Boyle, D. Fooksman, L. Margolis, M. Sheetz, and M. Edidin. Membrane cholesterol, lateral mobility, and the phophatidylinositol 4,5-biphosphate-dependent organization of cell actin. *PNAS*, 100:13964–13969, 2003.

S. Larsen, M. Egebald, M. Jaattela, and A. Lykkesfeldt. Acquired antiestrogen resistance in mcf-7 human breast cancer sublines is not accomplished by altered expression of receptors in the erbb-family. *Breast Cancer Res. Treat.*, 58:41–56, 1999.

D. A. Lauffenburger and J. J. Linderman. *Receptors: Models for Binding, Trafficking, and Signalling.* Oxford University Press, New York, 1993.

G. Lee, F. Zhang, A. Ishihara, C. McNeil, and K. Jacobson. Unconfined lateral diffusion and an estimate of pericellular matrix viscosity revealed by measuring the mobility of gold-tagged lipids. *J. Cell Biol.*, 120:25–35, 1993.

T. Libermann. Amplification, enhanced expression and possible rearrangement of egf receptor gene in primary human brain tumours of glial origin. *Nature*, 313:144–147, 1985.

B. Lin, J. Yu, and S. A. Rice. Direct measurements of constrained brownian motion of an isolated sphere between two walls. *Phys. Rev. E*, 62:3909–3919, 2000.

L. Lin and F. Brown. Dynamics of pinned membranes with application to protein diffusion on the surface of red blood cells. *Biophys. J.*, 86(2):764–780, 2004.

K. Lindenberg, P. Argyrakis, and R. Kopleman. Diffusion-limited binary reactions - the hierarchy of nonclassical regimes for correlated initial conditions. *J. Phys. Chem.*, 98:3389–3397, 1994.

J. Lippincott-Schwartz, N. Altan-Bonnet, and G. H. Patterson. Photobleaching and photoactivation: following protein dynamics in living cells. *Nat. Cell Biol.*, Suppl:7–14, 2003.

E. Livneh, M. Benveniste, R. Prywes, S. Felder, Z. Kam, and J. Schlessinger. Large deletions in the cytoplasmic kinase domain of the epidermal growth factor receptor do not affect its laternal mobility. *J. Cell Biol.*, 103(2):327–331, 1986.

P. H. M. Lommerse, G. A. Blab, L. Cognet, G. S. Harms, B. E. Snaar-Jagalska, H. P. Spaink, and T. Schmidt. Single-molecule imaging of the H-ras membrane-anchor reveals domains in the cytoplasmic leaflet of the cell membrane. *Biophys. J.*, 86:609–616, 2004.

P. Longati, A. Bardelli, C. Ponzetto, L. Naldini, and P. M. Comoglio. Tyrosines1234-1235 are critical for activation of the tyrosine kinase encoded by the MET proto-oncogene (HGF receptor). *Oncogene*, 9(1):49–57, 1994.

B. L. MacInnis and R. B. Campenot. Retrograde support of neuronal survival without retrograde transport of nerve growth factor. *Science*, 295(5559):1536–1539, 2002.

K. Mahadev, A. Zilbering, L. Zhu, and B. J. Goldstein. Insulin-stimulated hydrogen peroxide reversibly inhibits protein-tyrosine phosphatase 1b in vivo and enhances the early insulin action cascade. *J. Biol. Chem.*, 276:21938–21942, 2001.

L. Malmquist and H. Hertz. Unconfined lateral diffusion and an estimate of pericellular matrix viscosity revealed by measuring the mobility of gold-tagged lipids. *Opt. Commun.*, 94:19–24, 1992.

C. J. Marshall. Specificity of receptor tyrosine kinase signaling: transient versus sustained extracellular signal-regulated kinase activation. *Cell*, 80(2):179–185, 1995.

F. Maxfield. Plasma membrane microdomains. *Curr. Opin. Cell Biol.*, 14(2):483–487, 2002.

G. Mitra. Mutational analysis of conserved residues in the tyrosine kinase domain of the human trk oncogene. *Oncogene*, 6(12):2237–2241, 1991.

G. Moehren, N. Markevich, O. Demin, A. Kiyatkin, I. Goryanin, J. B. Hoek, and B. N. Kholodenko. Temperature dependence of the epidermal growth factor receptor signaling network can be accounted for by a kinetic model. *Biochemistry*, 41(1):306–320, 2002.

M. Mohammadi, I. Dikic, A. Sorokin, W. H. Burgess, M. Jaye, and J. Schlessinger. Identification of six novel autophosphorylation sites on fibroblast growth factor receptor 1 and elucidation of their importance in receptor activation and signal transduction. *Mol. Cell Biol.*, 16(3):977–989, 1996.

I. Mrani, G. Fras, and J. Benet. Microstructure et proprietes hygro-mecaniques du gel d'agar. *J. Phys. III*, 5:985–988, 1995.

K. Murase, T. Fujiwara, Y. Umemura, K. Suzuki, R. Iino, H. Yamashita, M. Saito, H. Murakoshi, K. Ritchie, and A. Kusumi. Ultrafine membrane compartments for molecular diffusion as revealed by single molecule techniques. *Biophys. J.*, 5:4075–4093, 2004.

J. Murray. *Mathematical Biology I.* Springer-Verlag, Berlin, 2002.

C. Nakada, K. Ritchie, Y. Oba, M. Nakamura, Y. Hotta, R. Iino, R. S. Kasai, K. Yamaguchi, T. Fujiwara, and A. Kusumi. Accumulation of anchored proteins forms membrane diffusion barriers during neuronal polarization. *Nat. Cell Biol.*, 5(7):626–632, 2003.

J. Neter, W. Wasserman, and G. Whitmore. *Applied Statistics, 3rd edition.* Allyn and Bacon, Inc., 1991.

K. Neuman, E. Chadd, G. Liou, K. Bergman, and S. Block. Characterization of photodamage to escherichia coli in optical traps. *Biophys. J.*, 77:2856–2863, 1999.

D. A. Neumayer. Photonic force microscopy with dynamic optical trap. Master's thesis, Fakultät für Physik und Astronomie der Ruprecht-Karls-Universität Heidelberg, 2003.

L. Oddershede, J. Dreyer, S. Grego, S. Brown, and K. Berg-Sorensen. The motion of a single molecule, the lambda-receptor, in the bacterial outer membrane. *Biophys. J.*, 83:3152–3161, 2002.

M. Offterdinger, V. Georget, A. Girod, and P. I. H. Bastiaens. Imaging phosphorylation dynamics of the epidermal growth factor receptor. *J. Biol. Chem.*, 279:36972–36981, 2004.

M. Ormo, A. B. Cubitt, K. Kallio, L. A. Gross, R. Y. Tsien, and S. J. Remington. Crystal structure of the Aequorea victoria green fluorescent protein. *Science*, 273(5280):1392–1395, 1996.

R. Ostrom and P. Insel. The evolving role of lipid rafts and caveolae in g protein-coupled receptor signaling: implications for molecular pharmacology. *Br. J. Pharmacol.*, 2004. [Epub ahead of print].

C. S. Park, I. C. Schneider, and J. M. Haugh. Kinetic analysis of platelet-derived growth factor receptor/phosphoinositide 3-kinase/Akt signaling in fibroblasts. *J. Biol. Chem.*, 278 (39):37064–37072, 2003.

A. Parsegian. The cows or the fence? *Molecular Membrane Biology*, 12:5–7, 1995.

T. Pawson. Regulation and targets of receptor tyrosine kinases. *Eur. J. Cancer*, 38 Suppl 5: S3–10, 2002.

R. Peters and R. Cherry. Lateral and rotational diffusion of bacteriorhodopsin in lipid bilayers: experimental test of the saffman-delbrück equations. *Proc. Natl. Acad. Sci.*, 79:4317–4321, 1982.

R. J. Phillips. A hydrodynamic model for hindered diffusion of proteins and micelles in hydrogels. *Biophys. J.*, 79:3350–3353, 2000.

A. Pluen, P. A. Netti, R. K. Jain, and D. A. Berk. Diffusion of macromolecules in agarose gels: comparison of linear and globular configurations. *Biophys. J.*, 77(1):542–552, 1999.

D. Pohl, W. Denk, and M. Lanz. Optical stethoscopy: image recording with a resolution of lambda/20. *Appl. Phys. Lett.*, 44:651–654, 1984.

E. Potma, W. P. de Boeij, P. J. van Haastert, and D. A. Wiersma. Real-time visualization of intracellular hydrodynamics in single living cells. *Proc. Natl. Acad. Sci.*, 98(4):1577–1582, 2001a.

E. O. Potma, W. P. de Boeij, L. Bosgraaf, J. Roelofs, P. J. van Haastert, and D. A. Wiersma. Reduced protein diffusion rate by cytoskeleton in vegetative and polarized dictyostelium cells. *Biophys. J.*, 81(4):2010–2019, 2001b.

J. Powles, M. Mallett, G. Rickayzen, and W. Evans. Exact analytic solutions for diffusion impeded by an infinite array of partially permeable barriers. *Proc. R. Soc. Lond. A.*, 436: 391–403, 1992.

A. Pralle. *Physical properties of the plasma membrane studied by local probe techniques.* PhD thesis, Fakultät für Physik der technischen Universität München, 1999.

A. Pralle, E.-L. Florin, E. Stelzer, and J. Hörber. Local viscosity probed by photonic force microscopy. *Appl. Phys. A*, 66:71–73, 1998.

A. Pralle, P. Keller, E.-L. Florin, K. Simons, and J. Hörber. Sphingolipid-cholesterol rafts diffuse as small entities in the plasma membrane of mammalian cells. *J. Cell Biol.*, 148: 997–1008, 2000.

A. Pralle, M. Prummer, E.-L. Florin, E. Stelzer, and J. Hörber. Three-dimensional position tracking for optical tweezers by forward scattered light. *Microscopy Research and Techniques*, 44:378–386, 1999.

D. Prieve and B. Alexander. Hydrodynamic measurement of double-layer repulsion between colloidal particle and flat plate. *Science*, 231:1269–1270, 1986.

H. Qian, M. Sheetz, and E. Elson. Single particle tracking. analysis of diffusion and flow in two-dimensional systems. *Biophys. J.*, 60:910–921, 1991.

A. Radhakrishnan, T. G. Anderson, and H. M. McConnell. Condensed complexes, rafts, and the chemical activity of cholesterol in membranes. *Proc. Natl. Acad. Sci.*, 97(23):12422–12427, 2000.

M. Radmacher, R. W. Tillmann, M. Fritz, and H. E. Gaub. From molecules to cells: imaging soft samples with the atomic force microscope. *Science*, 257:1900–1905, 1992.

A. R. Rees, M. Gregoriou, P. Johnson, and P. B. Garland. High affinity epidermal growth factor receptors on the surface of A431 cells have restricted lateral diffusion. *EMBO J.*, 3 (8):1843–1847, 1984.

F. Reif. *Statistische Physik und Theorie der Wärme.* Walter de Gruyter und Co., 1985.

A. Reynolds, C. Tischer, P. Verveer, O. Rocks, and P. Bastiaens. Egfr activation coupled to inhibition of tyrosine phosphatases causes lateral signal propagation. *Nat. Cell Biol.*, 5: 447–453, 2003.

H. Risken. *The Fokker-Planck Equation.* Springer-Verlag, 1989.

K. Ritchie, R. Iino, T. Fujiwara, K. Murase, and A. Kusumi. The fence and picket structure of the plasma membrane of live cells as revealed by single molecule techniques. *Mol. Membr. Biol.*, 20:13–18, 2003.

A. Rohrbach, H. Kress, and E. Stelzer. Three-dimensional tracking of small spheres in focused laser beams: influence of the detection angular aperture. *Opt. Lett.*, 28:411–413, 2003.

A. Rohrbach and E. Stelzer. Three-dimensional position detection of optically trapped dielectric particles. *Journal of Applied Physics*, 91:5474–5488, 2002a.

A. Rohrbach and E. Stelzer. Trapping forces, force constants and potential depths for dielectric spheres in the presence of spherical aberrations. *Appl. Opt.*, 41:2494–2507, 2002b.

A. Rohrbach, C. Tischer, D. Neumayer, E.-L. Florin, and E. Stelzer. Trapping and tracking a local probe with a photonic force microscope. *Rev. Sci. Inst.*, 75:2197–2210, 2004.

S. J. Ruff, K. Chen, and S. Cohen. Peroxovanadate induces tyrosine phosphorylation of multiple signaling proteins in mouse liver and kidney. *J. Biol. Chem.*, 272(2):1263–1267, 1997.

B. Y. S. Epidermal growth factor (egf)-induced generation of hydrogen peroxide. role in egf receptormediated tyrosine phosphorylation. *J. Biol. Chem.*, 272:217–221, 1997.

P. Saffman and M. Delbrück. Brownian motion in biological membranes. *Proc. Natl. Acad. Sci.*, 72:3111–3113, 1975.

Y. Sako and A. Kusumi. Compartmentalized structure of the plasma membrane for receptor movements as revealed by a nanometer-level motion analysis. *J. Cell Biol.*, 125(6):1251–1264, 1994.

Y. Sako and A. Kusumi. Barriers for lateral diffusion of transferrin receptor in the plasma membrane as characterized by receptor dragging by laser tweezers: fence versus tether. *J. Cell Biol.*, 129(6):1559–1574, 1995.

Y. Sako, A. Nagafuchi, S. Tsukita, M. Takeichi, and A. Kusumi. Cytoplasmic regulation of the movement of E-cadherin on the free cell surface as studied by optical tweezers and single particle tracking: corralling and tethering by the membrane skeleton. *J. Cell Biol.*, 140(5): 1227–1240, 1998.

D. S. Salomon, R. Brandt, F. Ciardiello, and N. Normanno. Epidermal growth factor-related peptides and their receptors in human malignancies. *Crit. Rev. Oncol. Hematol.*, 19(3): 183–232, 1995.

M. Sarmiento, Y. Zhao, S. J. Gordon, and Z. Y. Zhang. Molecular basis for substrate specificity of protein-tyrosine phosphatase 1B. *J. Biol. Chem.*, 273(41):26368–26374, 1998.

A. Sawano, S. Takayama, M. Matsuda, and A. Miyawaki. Lateral propagation of EGF signaling after local stimulation is dependent on receptor density. *Dev. Cell*, 3(2):245–257, 2002.

M. Saxton. Lateral diffusion in an archipelago: single-particle diffusion. *Biophys. J.*, 64: 1766–1780, 1993.

M. Saxton and K. Jacobson. Single-particle tracking: applications to membrane dynamics. *Annu. Rev. Biophys. Biomol. Struct.*, 26:373–399, 1997.

M. J. Saxton. Single-particle tracking: effects of corrals. *Biophys. J.*, 69(2):389–398, 1995.

J. Schlessinger. Cell signaling by receptor tyrosine kinases. *Cell*, 103(2):211–225, 2000.

J. Schlessinger, Y. Shechter, P. Cuatrecasas, M. C. Willingham, and I. Pastan. Quantitative determination of the lateral diffusion coefficients of the hormone-receptor complexes of insulin and epidermal growth factor on the plasma membrane of cultured fibroblasts. *Proc. Natl. Acad. Sci.*, 75(11):5353–5357, 1978.

T. Scholz, S. Altmann, M. Antognozzi, C. Tischer, H. Hörber, and B. Brenner. Mechanical properties of single myosin molecules probed with the Photonic Force Microscope. *Biophys. J.*, 2004. [Epub ahead of print].

G. Schütz, M. Sonnleitner, P. Hinterdorfer, and H. Schindler. Single molecule microscopy of biomembranes. *Mol. Membr. Biol.*, 17:17–29, 2000.

A. R. Sedaghat, A. Sherman, and M. J. Quon. A mathematical model of metabolic insulin signaling pathways. *Am. J. Physiol. Endocrinol. Metab.*, 283(5):1084–1101, 2002.

I. Segel. *Enzyme Kinetics*. John Wiley and Sons, Inc., New York, 1993.

O. Seksek, J. Biwersi, and A. S. Verkman. Translational diffusion of macromolecule-sized solutes in cytoplasm and nucleus. *J. Cell Biol.*, 138(1):131–142, 1997.

D. L. Senger and R. B. Campenot. Rapid retrograde tyrosine phosphorylation of trkA and other proteins in rat sympathetic neurons in compartmented cultures. *J. Cell Biol.*, 138(2): 411–421, 1997.

L. Shea, G. Omann, and J. Linderman. Calculation of diffusion-limited kinetics for the reactions in collision coupling and receptor cross-linking. *Biophysical Journal*, 73:2949–2959, 1997.

K. Simons and E. Ikonen. Functional rafts in cell membranes. *Nature*, 387(6633):569–572, 1997.

K. Simons and D. Toomre. Lipid rafts and signal transduction. *Nat. Rev. Mol. Cell Biol.*, 1: 31–41, 2000.

R. Simson, E. Sheets, and K. Jacobson. Detection of temporary lateral confinement of membrane proteins using single particle tracking analysis. *Biophys. J.*, 69:989–993, 1995.

S. Singer and G. Nicolson. The fluid mosaic model of cell membranes. *Science*, 175:720–731, 1972.

G. W. Slater and H. L. Guo. Ogston gel electrophoretic sieving: how is the fractional volume available to a particle related to its mobility and diffusion coefficient(s)? *Electrophoresis*, 16:11–15, 1995.

L. Smith, B. Smith, and H. McConnell. Lateral diffusion of M-13 coat protein in model membranes. *Biochemistry*, 18:2256–2259, 1979.

M. M. Sperotto and O. G. Mouritsen. Monte carlo simulation studies of lipid order parameter profiles near integral membrane proteins. *Biophys. J.*, 59:261–270, 1991.

M. Sundaresan, Z. X. Yu, V. J. Ferrans, K. Irani, and T. Finkel. Requirement for generation of h2o2 for platelet-derived growth factor signal transduction. *Science*, 270:296–299, 1995.

K. Suzuki, R. Sterba, and M. Sheetz. Outer membrane monolayer domains from two-dimensional surface scanning resistance measurements. *Biophys. J.*, 79:448–459, 2000.

Q. Tang and M. Edidin. Lowering the barriers to random walks on the cell surface. *Biophys. J.*, 84(1):400–407, 2003.

C. Tardin, L. Cognet, C. Bats, B. Lounis, and D. Choquet. Direct imaging of lateral movements of AMPA receptors inside synapses. *EMBO J.*, 22(18):4656–4665, 2003.

C. Tischer, S. Altmann, S. Fisinger, J. Hörber, E. Stelzer, and E.-L. Florin. Three-dimensional thermal noise imaging. *Appl. Phys. Lett.*, 79:3878–3880, 2001.

C. Tischer, A. Pralle, and E.-L. Florin. Determination and correction of position detection nonlinearity in single particle tracking and three-dimensional scanning probe microscopy. *Microscopy and Microanalysis*, 10:425–434, 2004.

A. Tolkovsky and A. Levitzki. Mode of coupling between the beta-adrenergic receptor and adenylate cyclase in turkey erythrocytes. *Biochemistry*, 17:3795–3810, 1978.

S. Traverse, K. Seedorf, H. Paterson, C. J. Marshall, P. Cohen, and A. Ullrich. EGF triggers neuronal differentiation of PC12 cells that overexpress the EGF receptor. *Curr. Biol.*, 4(8): 694–701, 1994.

G. Uhlenbeck and L. Ornstein. On the theory of brownian motion. *Physical Review*, 36: 823–841, 1930.

A. Ullrich, L. Coussens, J. Hayflick, T. Dull, A. Gray, A. Tam, J. Lee, Y. Yarden, T. Libermann, and J. Schlessinger. Human epidermal growth factor receptor cdna sequence and aberrant expression of the amplified gene in a431 epidermoid carcinoma cells. *Nature*, 309: 418–425, 1984.

M. Ushio-Fukai, L. Hilenski, N. Santanam, P. Becker, Y. Ma, K. Griendling, and R. Alexander. Cholesterol depletion inhibits epidermal growth factor receptor transactivation by angiotensin ii in vascular smooth muscle cells: role of cholesterol-rich microdomains and focal adhesions in angiotensin ii signaling. *J. Biol. Chem.*, 276:48269–48275, 2001.

G. Vereb, J. Szollosi, J. Matko, P. Nagy, T. Farkas, L. Vigh, L. Matyus, T. Waldmann, and S. Damjanovich. Dynamic, yet structured: The cell membrane three decades after the singer-nicolson model. *Proc. Natl. Acad. Sci.*, 100:8053–8058, 2003.

P. J. Verveer, F. S. Wouters, A. R. Reynolds, and P. I. Bastiaens. Quantitative imaging of lateral ErbB1 receptor signal propagation in the plasma membrane. *Science*, 290(5496): 1567–1570, 2000.

K. Visscher and G. J. Brakenhoff. Single beam optical trapping integrated in a confocal microscope for biological applications. *Cytometry*, 12(6):486–491, 1991.

M. C. Wang and G. Uhlenbeck. On the theory of brownian motion ii. *Rev. of mod. Physics*, 17:323–342, 1945.

P. B. Weisz. Diffusion and chemical transformation. *Science*, 179(72):433–440, 1973.

E. J. Westover, D. F. Covey, H. L. Brockman, R. E. Brown, and L. J. Pike. Cholesterol depletion results in site-specific increases in epidermal growth factor receptor phosphorylation due to membrane level effects. Studies with cholesterol enantiomers. *J. Biol. Chem.*, 278 (51):51125–51133, 2003.

A. M. Wiland, J. M. Denu, R. J. Mourey, and J. E. Dixon. Purification and kinetic characterization of the mitogen-activated protein kinase phosphatase rVH6. *J. Biol. Chem.*, 271 (52):33486–33492, 1996.

H. Wiley. Anomalous binding of epidermal growth factor to a431 cells is due to the effect of high receptor densities and a saturable endocytic system. *J. Cell Biol.*, 107:801–810, 1988.

L. Wu, A. Buist, J. den Hertog, and Z. Y. Zhang. Comparative kinetic analysis and substrate specificity of the tandem catalytic domains of the receptor-like protein-tyrosine phosphatase alpha. *J. Biol. Chem.*, 272(11):6994–7002, 1997.

T. Yamazaki, K. Zaal, D. Hailey, J. Presley, J. Lippincott-Schwartz, and L. E. Samelson. Role of Grb2 in EGF-stimulated EGFR internalization. *J. Cell Sci.*, 115:1791–1802, 2002.

Y. Yarden and M. X. Sliwkowski. Untangling the ErbB signalling network. *Nat. Rev. Mol. Cell Biol.*, 2(2):127–137, 2001.

E. Yechiel and M. Edidin. Micrometer-scale domains in fibroblast plasma membranes. *J. Cell Biol.*, 105(2):755–760, 1987.

Y. Zhao and Z. Y. Zhang. The mechanism of dephosphorylation of extracellular signal-regulated kinase 2 by mitogen-activated protein kinase phosphatase 3. *J. Biol. Chem.*, 276(34):32382–32391, 2001.

R. Zidovetzki, Y. Yarden, J. Schlessinger, and T. M. Jovin. Rotational diffusion of epidermal growth factor complexed to cell surface receptors reflects rapid microaggregation and endocytosis of occupied receptors. *Proc. Natl. Acad. Sci.*, 78(11):6981–6985, 1981.

E. Zwick, J. Bange, and A. Ullrich. Receptor tyrosine kinases as targets for anticancer drugs. *Trends Mol. Med.*, 8(1):17–23, 2002.

A. Östman and F. D. Böhmer. Regulation of receptor tyrosine kinase signaling by protein tyrosine phosphatases. *Trends Cell Biol.*, 11(6):258–266, 2001.

# Lebenslauf

## Persönliche Daten

Name: Christian Tischer
Geburtstag: 13. Dezember 1973
Geburtsort: Stuttgart
Adresse: Handschuhsheimer-Landstr. 86
69121 Heidelberg
Tel.: 06221-387406
E-mail: tischer@embl.de

## Ausbildung

| | |
|---|---|
| 10/2000 | Beginn der Promotionsarbeit |
| 09/2000 | Diplom in Physik, Ruprecht-Karls Universität, Heidelberg |
| 05/1993 | Abitur, Karls-Gymnasium, Stuttgart |

## Lehrerfahrung

| | |
|---|---|
| 10/1998-03/1999 | Tutor für Analysis II<br>Ruprecht-Karls Universität, Heidelberg |
| 05-09/1998 | Tutor für Lineare Algebra II<br>Ruprecht-Karls Universität, Heidelberg |

## Auszeichnungen

| | |
|---|---|
| 08/2003 | Students' Presentation Award<br>"Molecular Mechanisms in Signal Transduction"<br>EMBO/FEBS Advanced Lecture Course, Spetses, Griechenland |
| 04/2001 | Nikon Poster Award<br>Conference "Focus On Microscopy", Amsterdam, Niederlande |
| seit 10/2000 | Stipendiat des EMBL International PhD Programme<br>European Molecular Biology Laboratory, Heidelberg |

# Publikationsliste

Scholz, T., Altmann, S.M., Tischer, C., Hörber, J.K.H, and B. Brenner
Mechanical properties of single myosin molecules probed with the Photonic Force Microscope.
*Biophys. J.* (accepted)

Rohrbach, A., Tischer, C., Neumayer, D., Florin, E.-L., and E.H.K. Stelzer (2004) Trapping and tracking a local probe with a Photonic Force Microscope.
*Rev. Sci. Inst.* **75**, 2197–2210

Tischer, C., Pralle, A., and E.-L. Florin (2004) Determination and correction of position detection non-linearity in single particle tracking and three-dimensional scanning probe microscopy.
*Microscopy and Microanalysis* **10**, 425–434

Tischer, C. and P.I.H. Bastiaens (2003) Opinion: Lateral phosphorylation propagation: an aspect of feedback signalling? *Nat. Rev. Mol. Cell Biol.* **4**, 1–5

Reynolds, A., Tischer, C., Verveer, P.J., Rocks, O., and P.I.H. Bastiaens (2003)
Epidermal growth factor receptor activation coupled to inhibition of protein tyrosine phosphatases causes lateral signal propagation.
*Nat. Cell Biol.* **5**, 447–453 (A.R. and C.T. contributed equally)

Tischer, C. (2002) Three-dimensional scanning probe microscopy using Brownian Motion. *G.I.T. Imaging and Microscopy* **3**, 6–8

Tischer, C., Altmann, S., Fisinger, S., Hoerber, J.K., Stelzer, E.H.K., and E.-L. Florin (2001) Three-dimensional thermal noise imaging. *Appl. Phys. Lett.* **79**, 3878–3880

# Danksagung

An erster Stelle möchte ich Herrn Prof. R. Heinrich dafür danken, dass er bereit war, diese Arbeit zu betreuen. Durch sein Interesse an dieser Arbeit wurde meine Promotion ermöglicht.

Einen herzlichen Dank möchte ich Herrn Prof. P. Bastiaens aussprechen, der mich unterstützt hat und es immer wieder verstand, in den schwierigen Phasen dieser Arbeit aufbauende Worte zu finden.

Herrn Prof. E.-L. Florin möchte ich für die fruchtbare wissenschaftliche Zusammenarbeit und viele Diskussionen danken, die er zuletzt sogar aus Texas mit mir führte.

Vielen Dank an Dr. Arnd Pralle, auf dessen Vorarbeit viele Experimente dieser Arbeit beruhen und an Dr. Alexander Rohrbach für dessen hilfreiche Mitarbeit bei der Entwicklung des Mikroskops. Desweiteren möchte ich Dipl. Phys. Dirk Neumayer danken, der im Rahmen seiner Diplomarbeit die Software zur Mikroskopansteuerung entwickelte.

Einen großen Dank auch an die Mitarbeiter des Mechanical Workshop am EMBL: Leo Burger, Helmuth Schaar und Henry Werner, Dominik Haffner und Tarkan Karakol. Eure präzise und schnelle Arbeit und eure wertvollen Tips erlaubten es einem bis dahin eher theoretischen Physiker ein robust funktionierendes ”Nanoskop” zu bauen.

Einen ganz herzlichen Dank möchte ich allen Mitgliedern der Arbeitsgruppe Bastiaens aussprechen. Im speziellen möchte ich Dr. Martin Offterdinger und Anna Peyker für Ihre Hilfe bei der Molekularbiologie und Dr. Michael Keese und Dr. Andreas Girod für die unterhaltsamen Gespräche während des gemeinsamen Mikroinjektierens danken.

Einen großen Dank an alle, die Teile dieser Arbeit korrekturgelesen haben: Dr. Tony Squire, Dr. Jim Swoger, Dr. Peter Verveer, Janina Karres, Branimir Lukic, Dr. Sylvia Jeney, Dr. Alexander Rohrbach, Holger Kress, Dr. Piet Lommerse und Jens-Daniel Peter.

Abschließend möchte ich meinen Eltern danken. Ihre Unterstützung machte mein Studium und die anschließende Promotion erst möglich.

# Erklärung

Ich versichere hiermit, die vorliegende Arbeit selbständig und ausschließlich unter Verwendung der angegebenen Mittel und ohne unerlaubte Hilfen angefertigt zu haben.

Heidelberg, den

Christian Tischer